ELECTRON BEAM INDUCED DEPOSITION (EBID) OF CARBON INTERFACE BETWEEN CARBON NANOTUBE INTERCONNECT AND METAL ELECTRODE

A Thesis

Presented to

The Academic Faculty

by

Konrad Rykaczewski

In Partial Fulfillment

of the Requirements for the Degree

Doctor of Philosophy in the

School of Mechanical Engineering

Georgia Institute of Technology

October, 2009

ELECTRON BEAM INDUCED DEPOSITION (EBID) OF CARBON INTERFACE BETWEEN CARBON NANOTUBE INTERCONNECT AND METAL ELECTRODE

Approved by:

Dr. Andrei G. Fedorov, Advisor
School of Mechanical Engineering
Georgia Institute of Technology

Dr. Suresh Sitaraman
School of Mechanical Engineering
Georgia Institute of Technology

Dr. Azad Naeemi
School of Electrical and Computer Engineering
Georgia Institute of Technology

Dr. Yogendra Joshi
School of Mechanical Engineering
Georgia Institute of Technology

Dr. Vladimir V. Tsukruk
School of Material Science and Engineering &
School of Polymer, Textile, and Fiber Engineering
Georgia Institute of Technology

Date Approved: 10/16/2009

The next question is: How do we *write* small? We have no standard technique to do this now. But let me argue that it is not as difficult as it first appears to be. We can reverse the lenses of the electron microscope in order to demagnify as well as magnify. A source of ions, sent through the microscope lenses in reverse, could be focused to a very small spot. We could write with that spot like we write in a TV cathode ray oscilloscope, by going across in lines, and having an adjustment which determines the amount of material which is going to be deposited as we scan in lines.

-excerpt from Richard Feynman's talk *There's Plenty of Room at the Bottom,* 1959

ACKNOWLEDGEMENTS

First I would like to thank my parents, Anna and Krzysztof, for their support and guidance in all my pursuits throughout the past twenty five years. Second I would like to thank my advisor, Professor Fedorov, for being an inspiration, mentor, and friend during the past five years.

Financial support for this project has provided by National Science Foundation (NSF Grant DMI 0403671) and Semiconductor Research Corporation (GRC Grant 2008OJ1864.1281).

TABLE OF CONTENTS

LIST OF FIGURES

SUMMARY

Electron Beam Induced Deposition (EBID) is an emerging additive nanomanufacturing tool which enables growth of complex 3-D parts from a variety of materials with nanoscale resolution. Fundamentals of EBID and its application to making a robust, low-contact-resistance electromechanical junction between a Multiwall Carbon Nanotube (MWNT) and a metal electrode are investigated in this thesis research. MWNTs are promising candidates for next generation electrical and electronic devices, and one of the main challenges in MWNT utilization is a high intrinsic contact resistance of the MWNT-metal electrode junction interface. EBID of an amorphous carbon interface has previously been demonstrated to simultaneously lower the electrical contact resistance and to improve mechanical characteristics of the MWNT-electrode junction. In this work, factors contributing to the EBID formation of the carbon joint between a MWNT and an electrode are systematically explored via complimentary experimental and theoretical investigations. A comprehensive dynamic model of EBID using residual hydrocarbons as a precursor molecule is developed by coupling the precursor mass transport, electron transport and scattering, and surface deposition reaction. The model is validated by comparison with experiments and is used to identify different EBID growth regimes and the growth rates and shapes of EBID deposits for each regime. In addition, the impact of MWNT properties, the electron beam impingement location and energy on the EBID-made carbon joint between the MWNT and the metal electrode is critically evaluated. Lastly, the dominant factors contributing to the overall electrical resistance of the MWNT-based electrical interconnect and relative importance of the mechanical contact area of the EBID-made carbon joint to MWNT vs. that to the metal electrode are determined using carefully designed experiments.

CHAPTER 1

INTRODUCTION

As the feature sizes in electronic devices decrease to nano-scale, metal resistivity increases due to surface and grain boundary scattering and wire type structures become more vulnerable to electromigration effects [1]. Carbon nanotubes' (CNT) ballistic transport characteristics, high carrier mobility in the diffusive region, capability of handling large current densities without mechanical degradation, and exceptional mechanical properties make them an attractive material for nano-electronic components [2-4]. Multiwall carbon nanotubes (MWNT) are often preferred to single-wall carbon nanotubes (SWNT) due to their multi-channel conduction [5] and simpler manufacturing process [6]. Furthermore, Li et al. [6] showed that intermediate and global interconnects based on MWNT outperform both copper and random chirality SWNT-bundle based interconnects. In general, individual MWNT are implemented into devices in two geometrical arrangements: resting directly on a flat substrate and as a free standing extension of conventional Scanning Probe Microscopy (SPM) tips. When resting on a substrate, the MWNT is usually aligned in between and serves as an electrical interconnect of two thin metal electrodes [7]. When attached to a SPM tip, the MWNT is used to map the topography of the sample [8] and in specialized applications such as Conductive Force Microscopy (CFM) to map conductivity of the sample (see Figure 2.1).

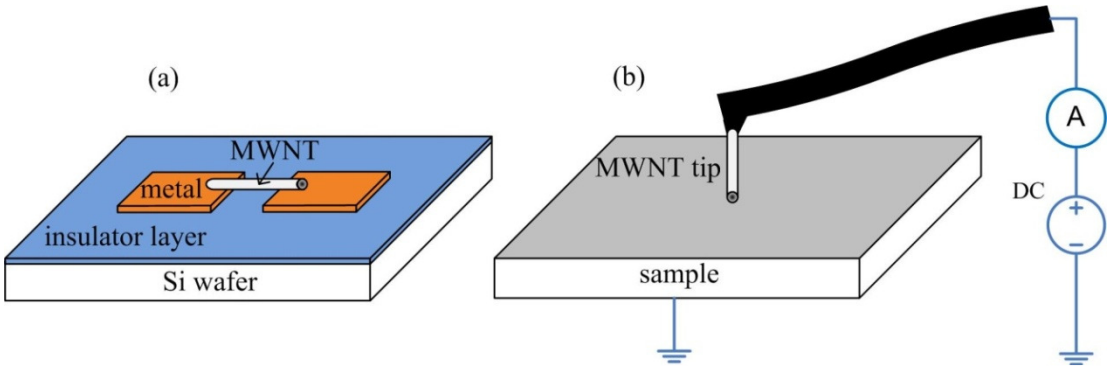

Figure 2.1. Schematic of two methods of integration of individual MWNT into devices (a) on flat substrate connecting two electrodes and (b) as a free standing conductive SPM tip.

Close et al. [7] recently demonstrated GHz-range operation of an integrated circuit with MWNT interconnects. However, the effective resistivity of the MWNT based interconnect was two orders of magnitude higher than that of copper. This example highlights one of the main challenges in implementation of MWNT as electrical components, namely the high (~10^6-10^8 Ω) contact resistance of the

CNT-metal conductor connection [2, 9]. In the case of MWNT components, establishment of electrical connection with inner shells of the tube poses an additional challenge [10]. While several groups were able to demonstrate very low contact resistance in vertically aligned [11, 12] or free standing MWNT [10, 13], the methods utilized, such as 'dipping' the end of the MWNT into a liquid metal [10] or growing MWNT from preformed catalyst nanoparticles, do not allow for control over the orientation of the tube and are difficult to implement in on-the-substrate configuration. In this type of device geometry, methods such as Electron Beam Lithography (EBL) of metal pads [14], joule heating [2], and gold nanoparticle ("nano-ink") suspensions deposition [15] have been applied for lowering of the contact resistance. As schematically shown in Figure 2.2, in application of these methods it is difficult to establish contact with the inner shells of tube because the conductor deposition occurs predominantly in the vertical direction. In addition these methods produce side-contacted rather than end-contacted CNT-metal geometries, which according to Tersoff [9] results in a weak electronic coupling at the Fermi surfaces and thus a higher intrinsic contact resistance.

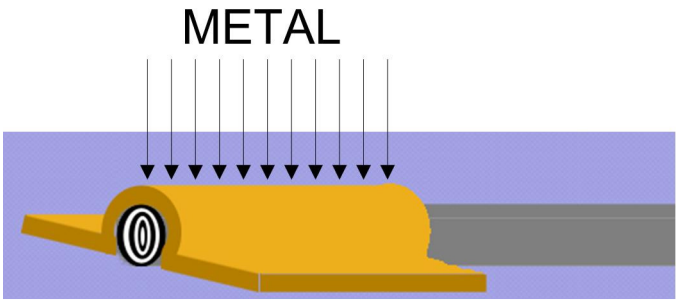

Figure 2.2. Schematic of metal MWNT contact fabrication.

Application of Electron Beam Induced Deposition (EBID) of carbon [16-18] or metal [19] CNT-electrode connection has potential to resolve the above-mentioned issues. In this process a tightly focused, high-energy electron beam impinges on a substrate and the high-energy primary electrons interact with the substrate to produce low energy secondary electrons (SE) and backscattered electrons (BSE). Figure 2.3a shows a general schematic of the process and physical phenomena involved in EBID. As demonstrated by Fedorov et al. [20], significant electron beam induced heating of the deposit and substrate occurs only under conditions rarely achievable in SEM, namely when the beam currents higher are than microampere.

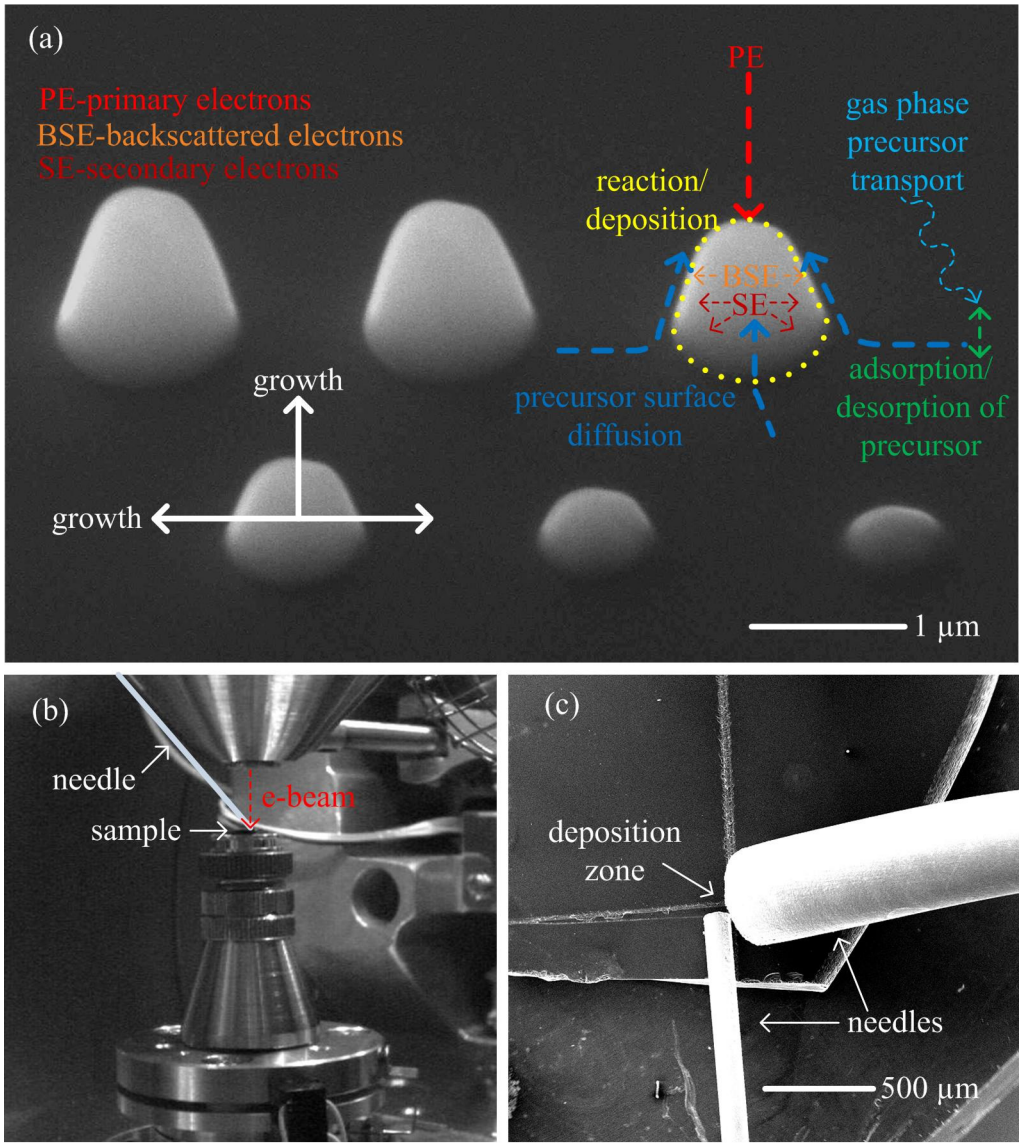

Figure 2.3. (a) Schematic of phenomena involved in EBID of typical carbon deposits grown for period of 1, 2, 3, 4, 5, and 6 minutes from methane precursor gas. (b) CCD camera view of the ESEM chamber showing location of the precursor needle, electron beam column, and a sample. (c) SEM image of dual gas injection deposition experiment.

The precursor delivery methods can be subdivided into two categories: gas-phase [20] and surface adsorbed phase [21] delivery. In the first method, precursor gas is introduced locally near the deposition area via a needle or globally by partial to complete flooding of the reaction chamber (see Figures 1.3b and c). In the second method, surface adsorbed residual hydrocarbons, sometimes supplemented by placing a

solid hydrocarbon supply such as a piece of paraffin, in the vicinity of the deposition area [21, 22] are used as a precursor. Because it can be used in conjunction with an unmodified Scanning Electron Microscope (SEM), the latter precursor delivery method has been widely utilized in CNT processing [8, 16-18, 23-37] and is the main focus of this work. Regardless of the precursor supply method, once adsorbed on the surface, the molecules redistribute by surface diffusion. Interactions of adsorbed molecules with backscattered primary and secondary electrons of the appropriate energy result in their dissociation forming a deposit. The vertical growth rates depend on the deposition procedure and the geometry of the deposit [38] and can vary from ~20 nm/min [38, 39] to ~3 μm/min [21, 40]. As shown in Figure 2.3a, the deposit grows both opposite to and perpendicular to the direction of the primary electron beam due to electron scattering within the deposit [38] and surface transport of the precursor [41].

The process also provides an opportunity for simultaneous improvement of the electrical [16] and mechanical characteristics of the connection [21]. The dual advantage of improving the contact resistance while forming a strong mechanical bond made EBID of amorphous carbon contacts a common technique in nanomanufacturing and metrology involving CNT [8, 17, 18, 23-25, 27-37, 42-50]. Bachtold et al.[16] were the first to demonstrate that an electron beam exposure of MWNT-metal electrode connection can lower the contact resistance by orders of magnitude. Soon after Yu et al.[26] applied Electron Beam Induced Deposition (EBID) of amorphous carbon for attaching a carbon nanotube to a tip of an Atomic Force Microscope (AFM). In addition to deposition of amorphous carbon from residual hydrocarbons some groups had deposited metals such as gold [42, 46-48] and tungsten [49] from organometalic gas precursors. The CNTs are usually soldered to AFM and nanomanipulator tips [8, 18, 23, 25-31, 33] or to thin metal electrodes deposited on an insulating substrate [16, 17, 35-37, 42, 43, 45-49]. The process has been applied in studying fundamental electrical [16-18, 31-33] and mechanical [25, 26, 31, 32, 36] properties of CNTs as well as in diverse applications, such as fabrication of interconnects [17, 32], mass sensors [45], CNT field emitters [27], nanoelectrodes for molecular devices [37], integration of CNTs into nanoelectromechanical [49] and nanorobotic systems [35]. Electron irradiation and the associated deposition of carbon have also been utilized in connecting and repairing CNTs [32, 37, 44]. The accelerating voltages and currents used varied from 5 kV and 7 pA [17] to 20 kV [16] and 100 pA [21].

The characterization of the EBID amorphous carbon connections has been limited to electrical [16, 17, 19, 23, 42, 47, 51, 52] and structural (TEM imaging [8, 44]).

While the application of EBID of amorphous carbon for improved CNT-electrode connection has been utilized before [16, 17, 19, 23, 42, 47, 51, 52], little attention has been dedicated to fundamental understanding of deposition process and influence of process parameters such as electron beam energy, current, geometry, and deposition time on the deposited interface geometry and electrical resistance. In this thesis, a fundamental study is undertaken with focus on understanding the deposition mechanisms and factors governing the formation and electrical properties of the EBID carbon MWNT-electrode connection.

Figure 2.4 schematically shows physical processes and technical issues related to EBID of carbon MWNT-electrode connection, mapping them out on the discussion presented in different chapters of this thesis. In Chapter 2, the physics governing the growth dynamics of EBID of residual hydrocarbons is explored. A comprehensive growth model of the process is formulated, implemented, and validated. Three distinct growth regimes, as well as their impact on the growth rate and shape of the deposits, are indentified using scaling analysis and confirmed through simulations.

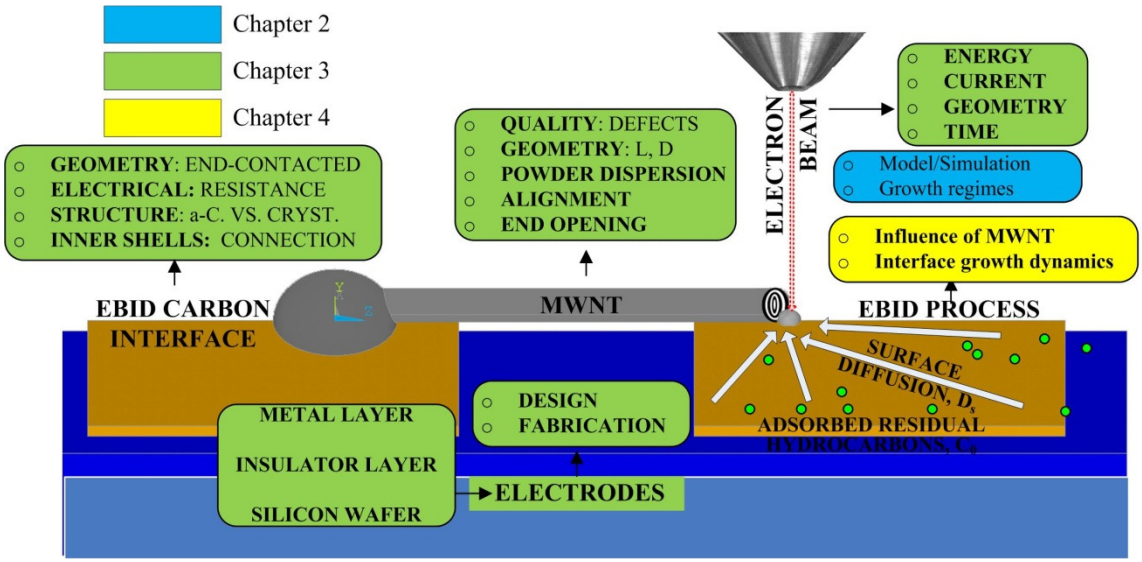

Figure 2.4. Schematic of the physical arrangement of the EBID-enabled MWNT interconnect, relevant technical issues, and parts of the thesis focusing on them.

In the last part of Chapter 2, complex growth dynamics of pillar within ring structures is simulated and compared against experimental results.

In Chapter 3 a systematic study of the interplay between the EBID process settings and their influence on the deposited interface geometry and electrical resistance is presented. A method for fabrication of MWNT interconnects is described and implemented. In-situ as well as post-deposition electrical characterization methods of the interconnects are discussed. The influence of the electron beam on the resulting electrical measurements is quantified. Two types of EBID carbon MWNT-electrode joint shapes are evaluated: cone-like and multiple square pads-like geometries. Deposition at the range of electron beam energies, currents, and diameters available in Quanta 200 ESEM is performed. Lastly, the effects of Joule heating on the resistance as well as structure of deposited carbon connections are studied. The experiments allow to define the factors contributing to the total resistance of the EBID MWNT interconnects, and dominating factors at each stage of the fabrication process.

In Chapter 4 the impact of MWNT on the EBID growth process is quantified. First, secondary electron emission from free standing MWNT is measured and compared against simulations. Next, cone-like deposits are grown on different locations of closed and open-ended MWNT and on the similar size amorphous carbon lines. The experimental results are explained through simulations of early stages of the cone-like deposit growth on top of MWNT with different secondary electron scattering properties. Next, the geometrical influence of the MWNT on the EBID process is quantified. Specifically, initial and later stages of EBID of carbon connection at the end of MWNT with different electron beam parameters are simulated. The results of simulations are related to electrical characterization results from Chapter 3. In Chapter 5, the results of the thesis work are critically summarized, and recommendations for the future work are made.

CHAPTER 2

GROWTH DYNAMICS OF ELECTRON BEAM INDUCED DEPOSITION OF RESIDUAL HYDROCARBONS

2.1 Introduction

Electron Beam Induced Deposition (EBID) of residual hydrocarbons is a common contamination issue in electron microscopy. In this process solid carbon deposit is formed due to interaction of backscattered electrons and secondary electrons with residual hydrocarbon species adsorbed on the surface of the substrate. However, with appropriate electron beam control this image degrading process can provide a basis for 3-D nanofabrication [40] and nanoscale metrology [21, 36]. Figure 2.1 shows a general schematic of the process and the physical phenomena involved in EBID [20]. The phenomenon was first recognized in late 1940's by Cosslett [53, 54], followed by postulation of possible physical mechanisms responsible for the contamination growth [55, 56]. A number of research groups have further explored the subject both experimentally and theoretically. Specifically, initial efforts focused on identifying and limiting the sources of hydrocarbon contamination [57, 58], which eventually led to the first attempt to theoretically describe the underlying physics of the problem [59]. Built on this initial progress, significant experimental and theoretical advances had been made in 70's and 80's by Reimer and Wachter [60], Fourie [58, 61, 62] and Hren [63], and more recently by Hirsh et al. [64] and Amman et al. [65]. A variety of structures have been deposited on different substrate materials, including carbon thin films [57, 64], dots [60, 63, 66], lines [65], and ring type structures [58, 60-62, 67], as well as complex three-dimensional structures [40, 68, 69]. The development of predictive capabilities was lagging the experimental advances.

Attempts to analyze EBID contamination deposits have been previously made by Reimer [60], Hren [63], Fourie [58, 61, 62], and Amman [65], by solving for both the steady-state and the transient spatial distributions of surface concentration of adsorbed hydrocarbons as qualitative indicators of the expected deposit shape. However, only recent developments in comprehensive EBID modeling [38, 70, 71] enabled the capability for detailed simulation of transient deposit growth. In this chapter a dynamic EBID model coupling mass transport, electron transport and scattering, and species decomposition predicting time evolution of the carbon deposit morphology is formulated, implemented, and validated by comparing with

experimental results. Different growth regimes are identified using scaling analysis and their impact on growth rate and shape of the deposit are explored using simulations. Lastly, complex growth dynamics of pillar within ring structures are simulated and compared against complementary experimental results.

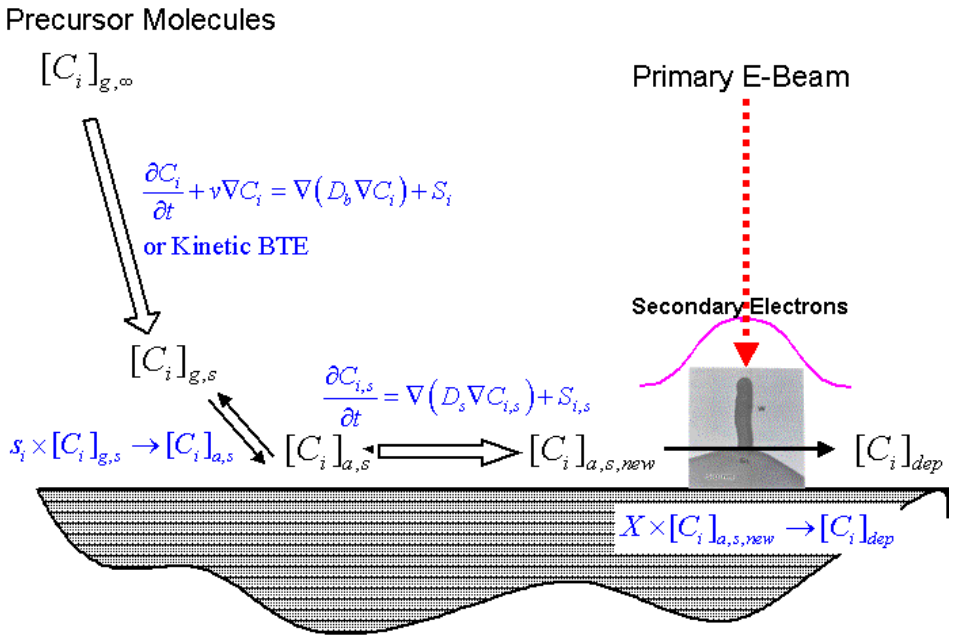

Figure 2.1. Schematic of Electron Beam deposition and key transport processes [20]. $[C_i]_{g,\infty}$ is the gas-phase concentration of "i"-th precursor species in the bulk, $[C_i]_{g,s}$ is the gas-phase concentration near the substrate, $[C_i]_{a,s}$ is the adsorbed-phase concentration of "i"-th precursor species, $[C_i]_{a,s,new}$ is the adsorbed-phase concentration of "i"-th precursor species in excited state upon surface diffusion to the deposition zone .

2.2 Model Formulation

2.2.1 Derivation of the Surface Transport Equation (STE)

Based on their experimental results, both Amman et al. [65] and Reimer and Wachter [60] have come to conclusion that surface diffusion is the primary species transport mode in EBID of residual hydrocarbons. The model proposed by Amman and Wachter [65] consisted of analytically solving surface diffusion equation with the initial condition of uniformly reduced surface concentration of the precursor within the reaction area. Such a formulation is inadequate because it does not take into account transient

spatial distribution of the precursor concentration and dynamic surface evolution effects during growth of a deposit. In this work, the principles of mass conservation are rigorously applied based on first principles to derive the governing equation for the adsorbed precursor transport. It is assumed that adsorption and desorption occur on much faster time scale and have reached quasi-equilibrium and do not affect the surface concentration. Initially, the deposition of nano-pillar which occurs when the microscope operates in the Spot mode is investigated. Figure 2.2 shows a diagram of the growing, radially symmetric fiber of an arbitrary shape. In this case the problem reduces to one dimension described by a single curve-linear coordinate (arc-length *s*) along the surface of the deposit. For simplicity the shape of the fiber is assumed to remain constant during the time step Δt which can be made small enough for this assumption to be valid. With this assumption surface concentration changes due to dilution (i.e., owing to instantaneous changes in the deposit shape) can be ignored. Also, surface properties of the deposit and substrate are assumed to be constant.

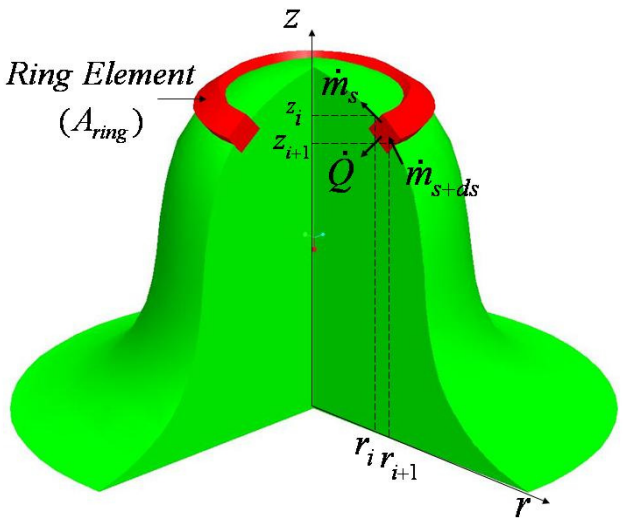

Figure 2.2. Schematic representation of a nanopillar with axial symmetry [41].

Difference in surface properties can be accounted for using a method outlined in Appendix A. Performing a mass balance on a ring control volume (Figure 2.2) results in:

$$2\pi\bar{r}\left(C\big|_{t+\Delta t} - C\big|_{t}\right)\Delta s = \left(\dot{m}_{net} - \dot{Q}\right)\Delta t \qquad 2.1$$

where $C(t,s)$ is the surface concentration at time *t* and arc length distance *s*, $\dot{m}_{net}$ is the net mass transfer

rate into the control volume, and $\dot{Q}$ is the mass sink due to deposition reaction. The net mass transfer rate $\dot{m}_{net}$ is equal to the difference between the rates of mass transfer due to surface diffusion at s and $s+\Delta s$:

$$\dot{m}_s = -2\pi r_s D \left.\frac{\partial C}{\partial s}\right|_s \qquad \dot{m}_{s+\Delta s} = -2\pi r_{s+\Delta s} D \left.\frac{\partial C}{\partial s}\right|_{s+\Delta s} \tag{2.2}$$

Where D is the surface diffusion coefficient of the adsorbed species. The mass sink (reaction) term represents the secondary electron induced dissociation of the adsorbed hydrocarbons. According to Silvis-Cividjian et al. [38] the dissociation reaction rate can be calculated as:

$$\dot{Q}''(s,t) = \int_0^E \sigma_d(E) C(s,t) j_{se}(E,s) dE = C(s,t) \int_0^{E\max} \sigma_d(E) j_{se}(E,s) dE = C\dot{Q}_1 \tag{2.3}$$

with $\sigma_d(E)$ being the dissociation reaction cross section in units of area per electron, $j_{se}(E,s)$ is the flux of secondary electrons with energy E arriving to the surface within a ring Δs at the location s in units of electron per area and time, and $\dot{Q}_1$ is the local "reactive" electron flux. Substituting these relations into the mass conservation Equation 2.1, and taking limits of Δs and Δt decreasing to zero and assuming a constant surface diffusion coefficient, the axi-symmetric STE with appropriate boundary (BC) and initial (IC) conditions is obtained.

$$\begin{aligned} &\frac{\partial C}{\partial t} = \frac{1}{r}\frac{\partial}{\partial s}\left(Dr\frac{\partial C}{\partial s}\right) - C\dot{Q}_1 = D\frac{\partial^2 C}{\partial s^2} + \frac{D}{r}\frac{\partial r}{\partial s}\frac{\partial C}{\partial s} - C\dot{Q}_1 \\ &\text{Boundary Conditions} \quad \left.\frac{\partial C}{\partial s}\right|_{s=0} = 0 \quad C\big|_{s\to\infty} = C_\infty \\ &\text{Initial Condition} \quad C(t=0,s) = C_0(s) \end{aligned} \tag{2.4}$$

In order to model arbitrary deposit shapes Equation 2.4 is generalized as follow:

$$\begin{aligned} &\frac{\partial C^{surf}}{\partial t} = D\nabla^2 C^{surf} - \dot{Q}^{surf}_{electrons} C^{surf}, \; C^{surf}:\mathrm{S}\to\mathbb{R}, \; \dot{Q}^{surf}_{electrons}:\mathrm{S}\to\mathbb{R} \\ &B.C. \; C^{surf}\big|_{x,y\to\pm\infty} = C_\infty \quad I.C. \; C^{surf}(t=0,x,y) = C_0 \end{aligned} \tag{2.5}$$

Where x and y are orthogonal coordinates along the 2D surface S of a 3D deposit.

2.2.2 Non-dimensionalization of Surface Transport Equation (STE)

Non-dimensionalizing a governing equation allows one to generalize the formulation for different sets of variables and offer insight into different behavior regimes. The non-dimensional form of the equation is

obtained by introducing the following dimensionless variables:

$$C^* = \frac{C}{C_\infty} \quad r^* = \frac{r}{d_b} \quad s^* = \frac{s}{d_b} \quad t^* = \frac{t}{t_{obs}} \quad \dot{Q}^* = \frac{\dot{Q}''_1}{\dot{Q}''_s} \tag{2.6}$$

The appropriate length scale d_b is the full width at 50% of the beam (diameter of the circle within which 50% of the primary electrons hits the substrate), and t_{obs} is the observation time scale on which growth of deposit occurs. The reactive electron flux scale $\dot{Q}_s$ is calculated as follow:

$$\dot{Q}_s = j_{PE}\delta_{SE}\sigma_{\max} \tag{2.7}$$

Where j_{PE} is the primary electron flux in units of electrons per unit time and area, δ_{SE} is the secondary electron yield per primary electron, and $\sigma_{\max}$ is the maximum dissociation cross section in units of area per electron. The diffusion time scale t_{diff} is equal to diffusion length scale (equal to d_b for the problem in hand) squared divided by the surface diffusion coefficient ($= d_b^2 / D$). The reactive electron flux time scale t_{sink} is equal to inverse of reactive electron flux scale term $\dot{Q}_s$ given by Equation 2.7 ($= 1/ j_{PE}\delta_{SE}\sigma_{\max}$). Substituting these scales into the governing Equation 2.4 yields:

$$\frac{\partial C^*}{\partial t^*} = \frac{t_{obs}}{t_{\text{diff}}}\left(\frac{1}{r^*}\frac{\partial}{\partial s^*} r^* \frac{\partial C^*}{\partial s^*}\right) - \frac{t_{obs}}{t_{\text{sink}}} C^* \dot{Q}^* \tag{2.8}$$

Dependent on selection of the observation time scale and the relative magnitude of the time scales for reactive electron flux time scale and diffusion, Equation 2.8 can be simplified using scaling analysis yielding the conditions for different deposition regimes. Details of the scaling analysis are given in Appendix B.

2.2.3 EBID mass deposition rate and morphology evolution

The total EBID mass deposition rate, $\dot{m}(t)$, can be calculated with the following relation:

$$\dot{m}(t) = \int_S C^{surf}(t,x,y)\dot{Q}^{surf}_{electron}(t,x,y)dA \tag{2.9}$$

The local the mass deposition rate, $\dot{m}(t,x,y)$, can be calculated by multiplying the product $C^{surf}(t,x,y)\dot{Q}^{surf}_{electron}(t,x,y)$ by a an elementary area *dA(t,x,y)* surrounding each location on the surface. The incremental increase in height of the deposit, *dh(t,x,y),* for a given position in space (in the direction normal

to the area *dA (t,x,y)*) is equal to the local increase in volume due to the mass deposition, *dV*, divided by the area *dA*. The *dh(t,x,y)* can thus be calculated as follow:

$$dh(t,x,y) = \frac{dV(t,x,y)}{dA(t,x,y)} = \frac{dm(t,x,y)}{\rho dA(t,x,y)} = \frac{\dot{m}(t,x,y)dt}{\rho dA(t,x,y)} = \frac{C^{surf}(t,x,y)\dot{Q}^{surf}_{electron}(t,x,y)dA(t,x,y)dt}{\rho dA(t,x,y)} = \frac{C^{surf}(t,x,y)\dot{Q}^{surf}_{electron}(t,x,y)dt}{\rho} \quad 2.10$$

Where ρ is the density of the deposited solid material and *dt* is the time increment. Details of the numerical growth rate computation and growth procedure are given in Appendix D.

2.2.4 Reactive Electron Flux Model

In order to compute the reactive electron flux appropriate electron induced dissociation and ionization cross sections have to be selected. Cross sections for adsorbed molecular electron induced dissociation and ionization are usually difficult to obtain. Silvis-Cividjian et al. [38] used gas-phase dissociation reaction cross sections to approximate the adsorbed phase precursor dissociation cross sections. In this work, an approach suggested by Fowlkes et al. [72] is used for approximation of the deposition reaction cross section: that is an electron impact gas phase dissociation cross section is applied for electron energies below the threshold energy, corresponding to intersection of the gas phase ionization and gas phase dissociation cross section curves for the precursor, and, for electron energies beyond the threshold, the electron impact gas phase ionization cross section is used for computing the dissociation reaction rate (Equation 2.3). The Alman et al.'s [73] model (Equation 2.11) is used to approximate the electron impact dissociation cross section, while experimental data from Kwitnewski et al. [74] are fitted to a model suggested by Fowlkes et al. [72] to approximate the ionization cross section (Equation 2.12). A general equation for the electron-impact dissociation cross section of a generic C_xH_y is given by [73]:

$$\sigma_d(E) = \begin{cases} 0, \ \mathrm{E} \le \mathrm{E}_{\mathrm{th}} \\ \sigma_{\max}\left(1 - \dfrac{(E_{\max} - E)^2}{(E_{\max} - E_{th})^2}\right), \ \mathrm{E}_{\mathrm{th}} < \mathrm{E} < \mathrm{E}_{\max} \\ \sigma_{\max} e^{(E_{\max} - E)/\lambda}, \ \mathrm{E} \ge \mathrm{E}_{\max} \end{cases} \quad 2.11$$

Where E_{th} is the threshold energy, $E_{\max}$ is the peak energy, and λ is a constant that determines the rate of decay of the dissociation cross section in respect to electron energy away from its peak value of $\sigma_{\max}$.

The commonly used functional form for ionization cross section is:

$$\sigma_i(E) = \frac{A_1}{E^3} + \frac{A_2}{E^2} + \frac{A_3}{E} + A_4\left(\frac{\log E}{E}\right) + A_5\left(\frac{\log E}{E^2}\right) \qquad 2.12$$

Where E is the electron energy in units of electron-volts and A's are fitting parameters. This expression for the ionization cross section is derived from the binary-encounter Bethe model [75] which combines the Mott cross section and the high temperature behavior of the Bethe cross section [72]. According to Fowlkes et al. [72], this functional form is typically reported for energies up to 5 keV, but is expected to be a good fit for higher energies, as well.

The cross sections for C_4H_6, a representative residual hydrocarbon contamination, are used in all simulations hereafter. The reactive electron flux is computed with a cutoff energy of 7 keV for secondary and backscattered primary electrons predicted by Monte Carlo simulations [41]. Figure 2.3 shows final interaction cross section utilized in this work. Refer to Appendix C for list of all related constants and fitting parameters.

The reactive electron flux for a differential area of dA and time increment dt is:

$$\dot{Q}_{electrons}^{surf} = \sum_{0}^{E_{max}} \frac{\mathrm{SE}|_{E=E'}\,\sigma(E')}{dA\,dt} \quad [\frac{1}{s}] \qquad 2.13$$

Where $\mathrm{SE}|_{E=E'}$ is the number of secondary electrons with energy E' emerging from surface element dA during the time dt.

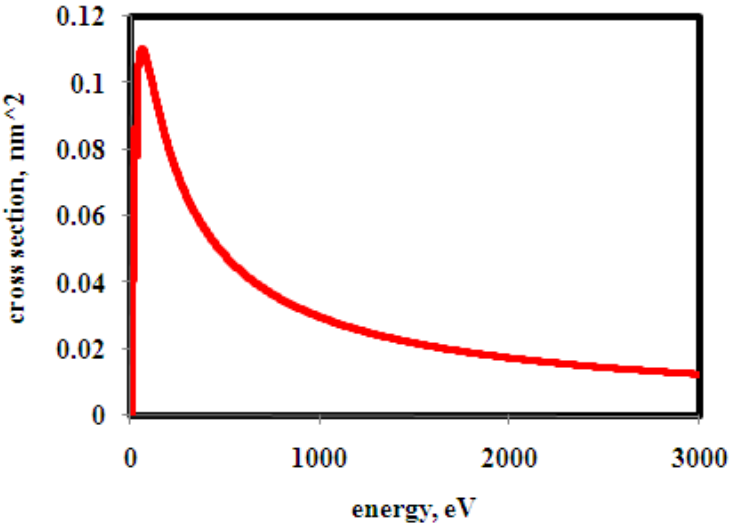

Figure 2.3. Total cross section vs. electron energy utilized in simulations.

2.2.5 Electron transport and generation models

A three dimensional single electron scattering Monte Carlo method described by Joy [76] and recently implemented by Mitsuishi et al.[70] is used in this work. Upon entering the substrate, the primary electron energy and momentum change due to scattering. An electron can experience both elastic and inelastic scattering. In order to simulate an elastic collision the Elastic Mean Free Path (EMFP) and the angle after the collision have to be known. Here, the Rutherford cross section corrected for relativistic effects and screening of the nucleus by inner shell electrons is used since the simulated primary electrons have energies above 10 keV [76]. In order to simulate an inelastic collision the Inelastic Mean Free Path (IMFP), the energy lost, and the angle after collision have to be determined. It is assumed that all energy lost by a primary electron in an inelastic collision is lost to excitation of another, so called generated secondary electron. To compute the inelastic mean free path and energy lost of the primary electrons the Fast Secondary Electron (FSE) model is used. FSE model assumes that secondary electrons are produced only by a knock-on collision with a free electron [76]. For computational efficiency the primary electron is simulated until it reaches a set depth or a radial distance from the center of the beam or reaches a fix maximum number of collisions. The secondary electrons have a very shallow escape depth and may induce deposition, following their creation just below the surface, when a primary electron enters the surface,

within ~5 MFP of the electron entry point (SE^{I}), or following their creation when a backscattered electron leaves the surface (SE^{II}) [76]. Dependent on the deposition settings, the simulation domain of the primary electrons has to be adjusted to allow for an accurate calculation of both SE^{I} and SE^{II} contributions relevant to the deposition process. The straight line approximation is used to approximate transport of the generated, low energy SE's (both SE^{I} and SE^{II}) to the surface. If a SE reaches the surface its energy is modified by probabilities for the absorption and escape from the surface barrier. For simulation of a multipart target with characteristics dimensions comparable to the mean free path of the electron approach taken by Li et al. [77] and Yue et al. [78] is adopted. The small energy change associated with passing boundary between two materials with different Fermi energies and work functions [78] is taken into account in modeling of low energy secondary electrons and is neglected in modeling of high energy primary electrons. Detailed description of all the electron transport and generation models used is given in Appendix C.

2.2.6 Solution Algorithm

2.2.6.1 Axi-symmetric Surface Transport Equation (STE)

Due to its non-linear nature the STE cannot be solved analytically and a numerical approach has to be taken. Since it is a parabolic differential equation it can be numerically integrated by marching in the direction of increasing time from given initial conditions. To develop the marching procedure, which is intrinsically mass-conservative, integration is carried out over the control volume around each node *i* for time step *n* and *n+1*. Each node represents a center of a control volume as schematically shown in Figure 2.2. Since Monte Carlo computation of the secondary electrons is done for ring segments Δs_i and Δs_{i+1} adjacent to the node s_i, the area-weighted averaging of the reactive electron flux terms is being used to compute $\dot{Q}_{1_{ave}}$ for the appropriate ring element Δs_{ave} of each node s_i. This conserves, even locally, the total number of secondary electrons leaving the substrate through each segment of the mesh, which is essential for accuracy of simulations. Assuming stepwise spatial variation of concentration from one control volume to the next and using fully implicit approximation of all derivatives in Equation 2.4 yield an

absolutely stable algorithm, which is first order accurate in time and second order accurate in space, expressed as a system of linear algebraic equations:

$$dC_i^n = aC_{i-1}^{n+1} + bC_i^{n+1} + cC_{i+1}^{n+1} \tag{2.14}$$

where coefficients *a,b,c* and *d* are:

$$a = \frac{D}{r\Delta s_{ave}} \frac{r_{i-1/2}}{\Delta s_i}, \quad c = \frac{D}{r\Delta s_{ave}} \frac{r_{i+1/2}}{\Delta s_{i+1}}, \quad d = -\frac{1}{\Delta t}$$
$$b = \frac{-1}{\Delta t} + \frac{D}{r\Delta s_{ave}} \left(\frac{-r_{i+1/2}}{\Delta s_{i+1}} - \frac{r_{i-1/2}}{\Delta s_i} \right) - \dot{Q}_{l_{ave}} \tag{2.15}$$

Now the problem takes the form of a system of linear algebraic equations with a tridiagonal matrix of coefficients given by Equation 2.14, which is easily solvable using Thomas TDMA matrix inversion routine outlined by Press et al. [79]. Further details of the solution algorithm and computational implementation are given in Appendix C.

2.2.6.2 Generalized Surface Transport Equation (STE)

The generalized STE (Equation 2.5) is solved using FLUENT CFD software. The surface mass transport is simulated using the three dimensional User Defined Scalar (UDS) transport model with a user specified mass sink term. The UDS transport equation is discretized using Finite Volume Method and solved implicitly in time domain. For each individual cell, FLUENT solves the following equation:

$$\frac{\partial \rho \phi}{\partial t} V = \sum_f^{N_{faces}} D_\phi \nabla \phi_f \cdot \vec{A}_f + S_\phi V \tag{2.16}$$

Where $\nabla \phi_f$ is the gradient, D_ϕ is the diffusion coefficient, S_ϕ is the mass source term (Equation 2.3), and ρ is the density of the scalar quantity φ, and V and $\vec{A}_f$ are the volume and face area vector of each cell, respectively. When the solution is confined to a constant height thin shell cell with zero flux boundary conditions on top and bottom face and ρ is set to 1, Equation 2.16 reduces to the height independent Equation 2.17:

$$\frac{\partial \phi}{\partial t} A = \sum_f^{N_{edges}} D_\phi \nabla \phi \cdot \vec{L}_f + S_\phi A \tag{2.17}$$

Where $\vec{L}_f$ is the length of each edge and A is the area of the given face. Further details of the solution

algorithm and computational implementation are given in Appendix D.

2.3 Validation and results

2.3.1 Electron transport and generation

2.3.1.1 Electron scattering and generation on flat silicon substrate

First, the electron transport and generation simulations for scattering on a flat silicon substrate are validated. Figure 2.4 compares the simulated secondary electron and backscattered electron yields to experimental data from D.C. Joy's electron-material interactions database [80]. It is important to note that most assumptions taken in primary electron transport models are not valid below ~5-10 keV. Figure 2.5 shows typical secondary and backscattered electron energy distributions resulting from simulation of 100,000 primary electrons impinging on flat silicon substrate at 30 keV.

As shown in Figure 2.5b, most of backscattered electrons have energies slightly below that of the primary electrons and significantly higher than the cut off energy of 7keV for deposition (see sections 2.2.4 and 2.2.5). Thus, in the reaction-limited deposition regime, backscattered electrons do not contribute significantly to the deposition process. Under certain conditions, when deposition occurs under diffusion-limited conditions, growth induced by backscattered electrons can be comparable to that induced by the secondary electrons due to severely depleted precursor surface concentration near the center of the beam [39]. Growth dynamics in the reaction-limited, diffusion-limited, and mixed regimes are explored in the following sections.

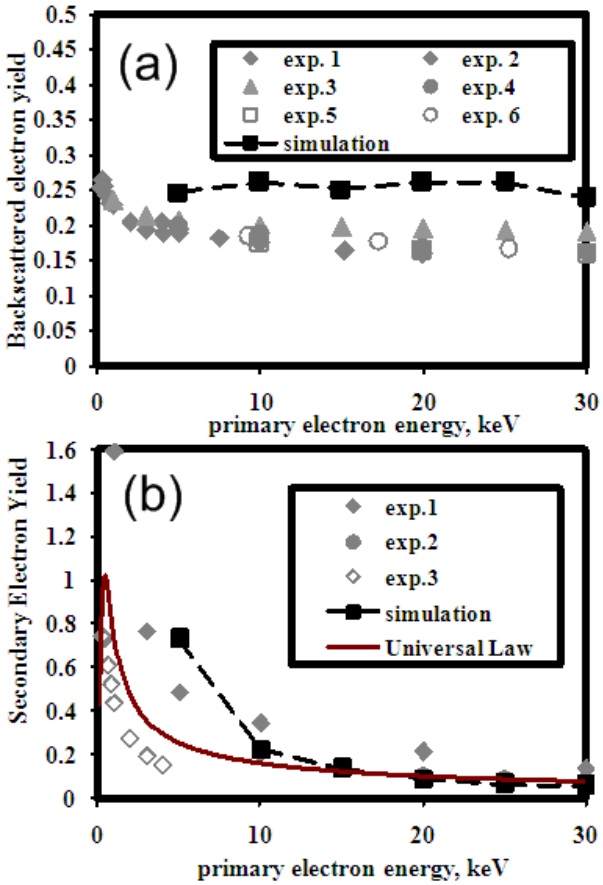

Figure 2.4. Comparison of simulation and experiments: (a) Backscattered electrons (BSE), and (b) Secondary electrons (SE) yields from flat silicon substrate. The simulated and experimental SE yields are also compared to the SE yield universal law from Lin and Joy [81].

The corresponding spatial distributions of backscattered electrons and secondary electrons are presented in Figure 2.6. It is important to point out that, for an electron beam with Full Width at Half Maximum (FWHM) diameter of 10 nm, 90% of the total generated secondary electrons are emitted within ~25 nm of the center of the beam. In contrast, only about 0.25% of total generated backscattered electrons are emitted within same size circle.

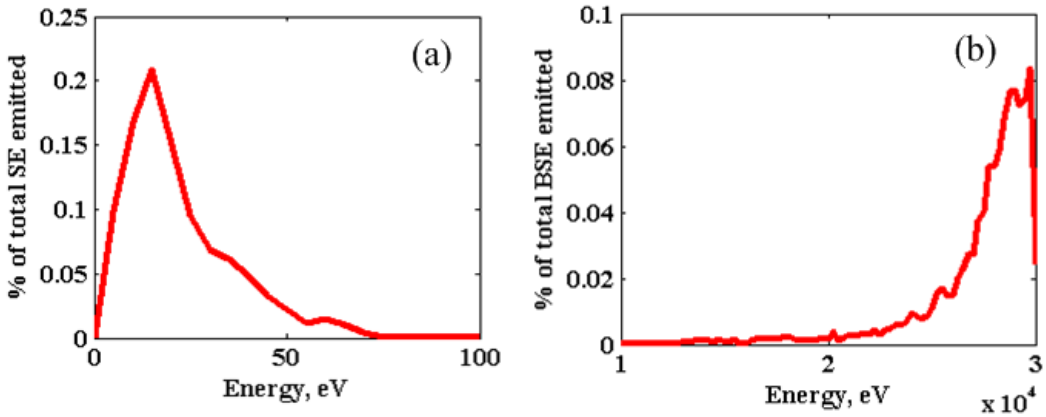

Figure 2.5. Example of (a) SE, and (b) BSE energy distributions resulting from simulation of 100,000 PE impinging on the flat silicon substrate at 30 keV.

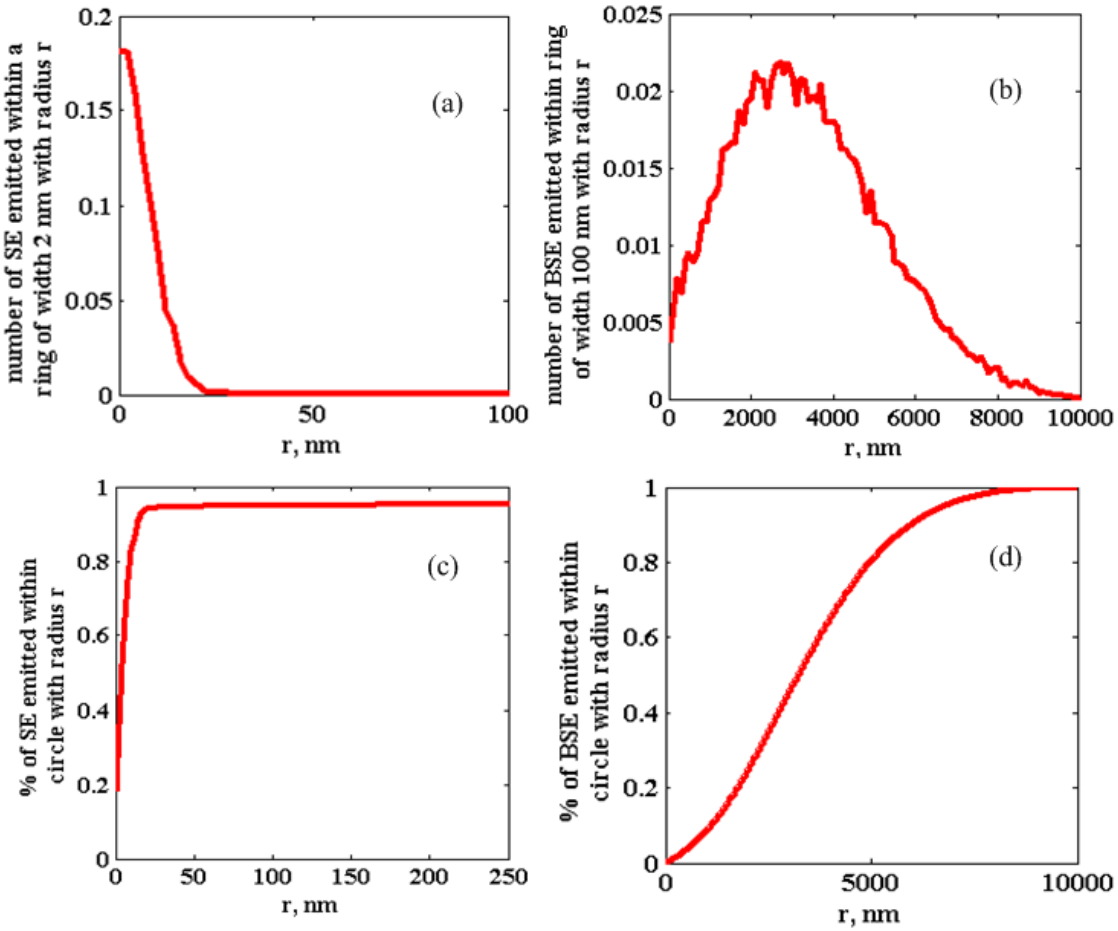

Figure 2.6. Number of (a) SE and (b) BSE emitted inside of a rings of radius r (number of electrons normalized to the total number of (a) SE and (b) BSE emitted). (c) Percentage of total emitted SE inside circle of radius r, and (d) Percentage of total BSE emitted inside circle of radius r. Results from simulation of 100,000 primary electrons impinging on the flat silicon substrate at 30 keV with FWHM diameter of 10 nm.

2.3.1.2 Electron scattering and generation within MWNT and substrate geometry

In this Chapter, the MWNT is modeled as a solid amorphous carbon cylinder resting on flat Si substrate. To validate the geometrical aspects of the electron scattering and generation simulations, electron transport within MWNT resting on flat substrate is simulated. Figure 2.7 shows two-dimensional projections of trajectories of 50 representative electrons with three different energies scattering within a MWNT with diameter of 50 nm laying on flat silicon substrate. As expected, penetration depth of the primary electrons increases with the increase in their energy.

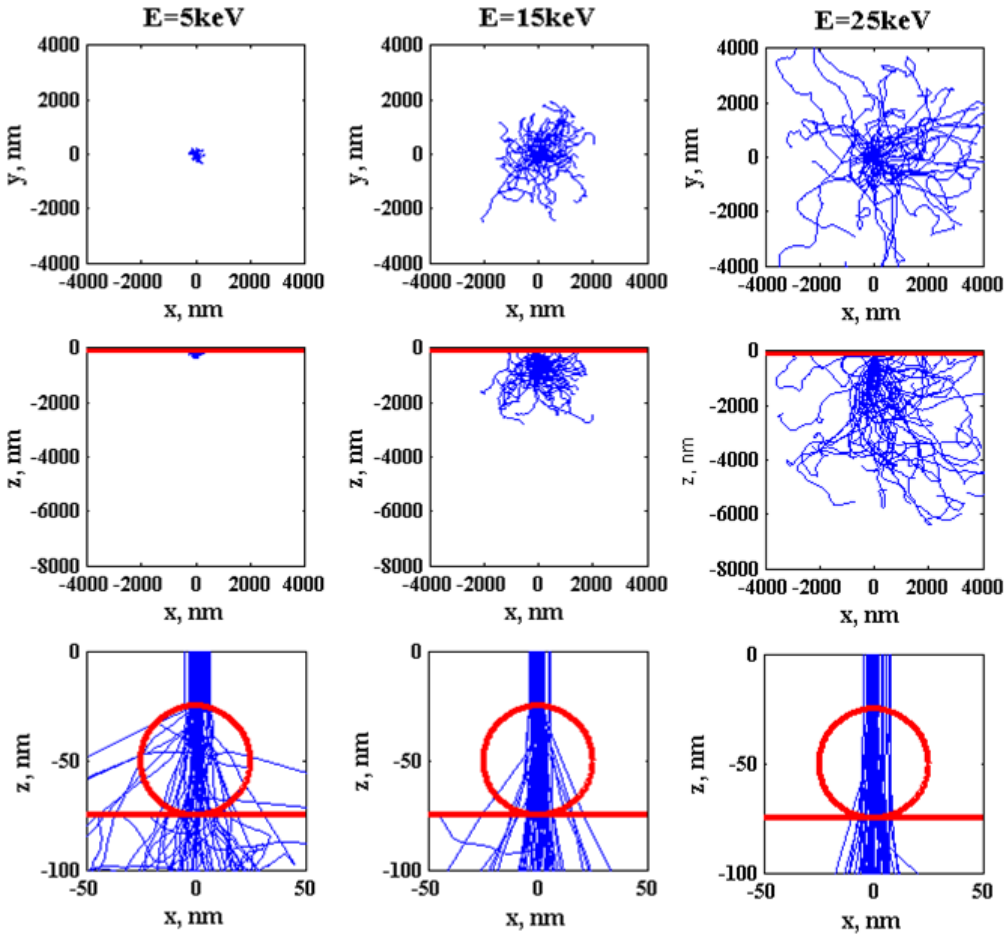

Figure 2.7. Examples of top (xy-plane) and side (xz-plane) projections of trajectories of 50 electrons at 5keV, 15keV, and 25keV from a beam with FWHM diameter of 5 nm centered at the origin. The target material consists of a MWNT with diameter of 50 nm and length of 800 (with center at the origin) laying on a flat silicon substrate, as shown using red-contour lines at bottom panel of figures.

As illustrated in Figure 2.7, with increasing energy primary electrons experience a significant decrease in

scattering within the MWNT itself. However, as shown in Figure 2.8, as the center of the beam is moved away from the axis of the tube, the number of primary electrons scattering out of the side and the bottom of the tube increases. An increase in the number of scattering events near the surface of the specimen causes a significant increase in the local SE yield and is commonly referred to in electron microscopy as the *edge effect*.

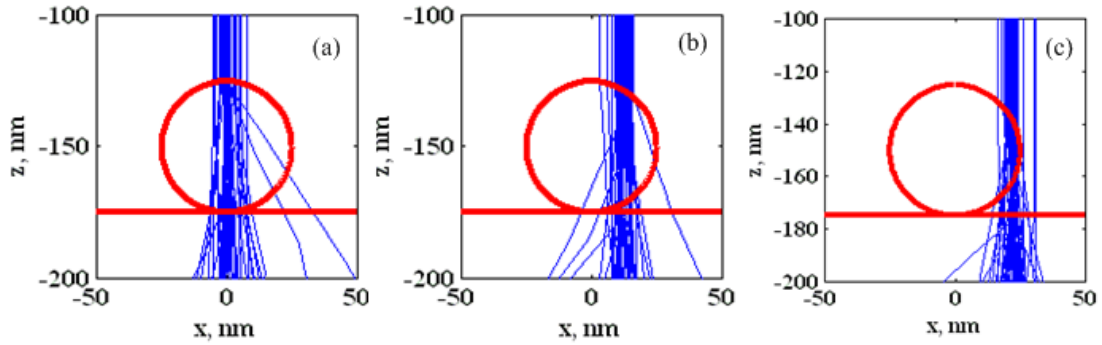

Figure 2.8. Example of side (x-z -plane) projections of trajectories of 50 electrons at 25 keV from a beam with FWHM diameter of 5 nm impinging at a MWNT with diameter of 50 nm laying on a flat Silicon substrate at distance of (a) 0 nm, (b) 12 nm, and (c) 22 nm off-center of the tube.

The geometrical aspects of the electron transport and generation simulation are validated by comparing the simulated and experimental line scan across a MWNT for four different electron beam settings. As shown in Figure 2.9, very good agreement is obtained between predictions and measurements. It is important to point out that this comparison is qualitative because of the experimental line scan data is not quantitative (contrast and brightness of the measurement are automatically adjusted by the ESEM user interface software).

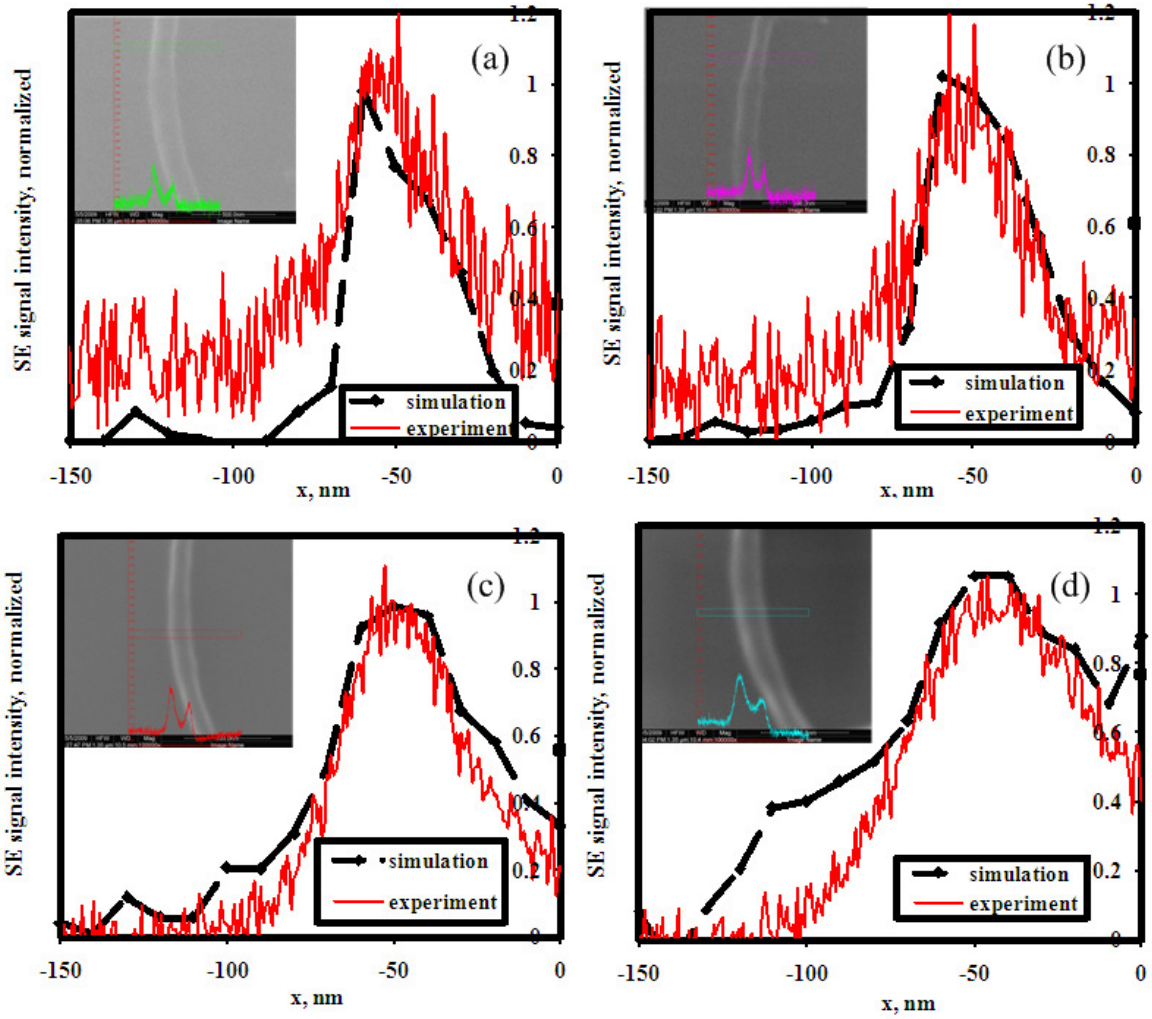

Figure 2.9. Simulated and experimental line scans across a MWNT with diameter of ~125 nm with primary electron energy of 30 keV and (a) FWHM diameter of 10 nm and current of ~1 pA, (b) FWHM diameter of 20 nm and current of ~5 pA, (c) FWHM diameter of 40 nm and current of ~21 pA, (d) FWHM diameter of 80 nm and current of ~80pA. All yields were calculated from simulation of 50000 PE. All experiments were performed in Tungsten Filament FEI Quanta 200 ESEM with current measured with a Faraday cup. The theoretically estimated FWHM diameters were obtained from the microscope manufacturer (FEI company).

2.3.2 Mass transport

The surface mass transport simulations are validated by comparing numerical and analytical solutions to the problem described in Figure 2.10a. As shown in Figure 2.10b and Figure 2.10c, the quasi three-dimensional (confined to a thin "virtual" shell in order to simulate a 2D surface transport, see Appendix D for details) mass transport simulation results compare well to one dimensional solution of the axi-

symmetric problem [82] (Equation 2.18).

$$C^*(r,t) = 1 - \sum_{m=1}^{\infty} \frac{J_0(\lambda_m r) e^{-D\lambda_m^2 t}}{\lambda_m r_0 J_1(\lambda_m r_0)} \qquad 2.18$$

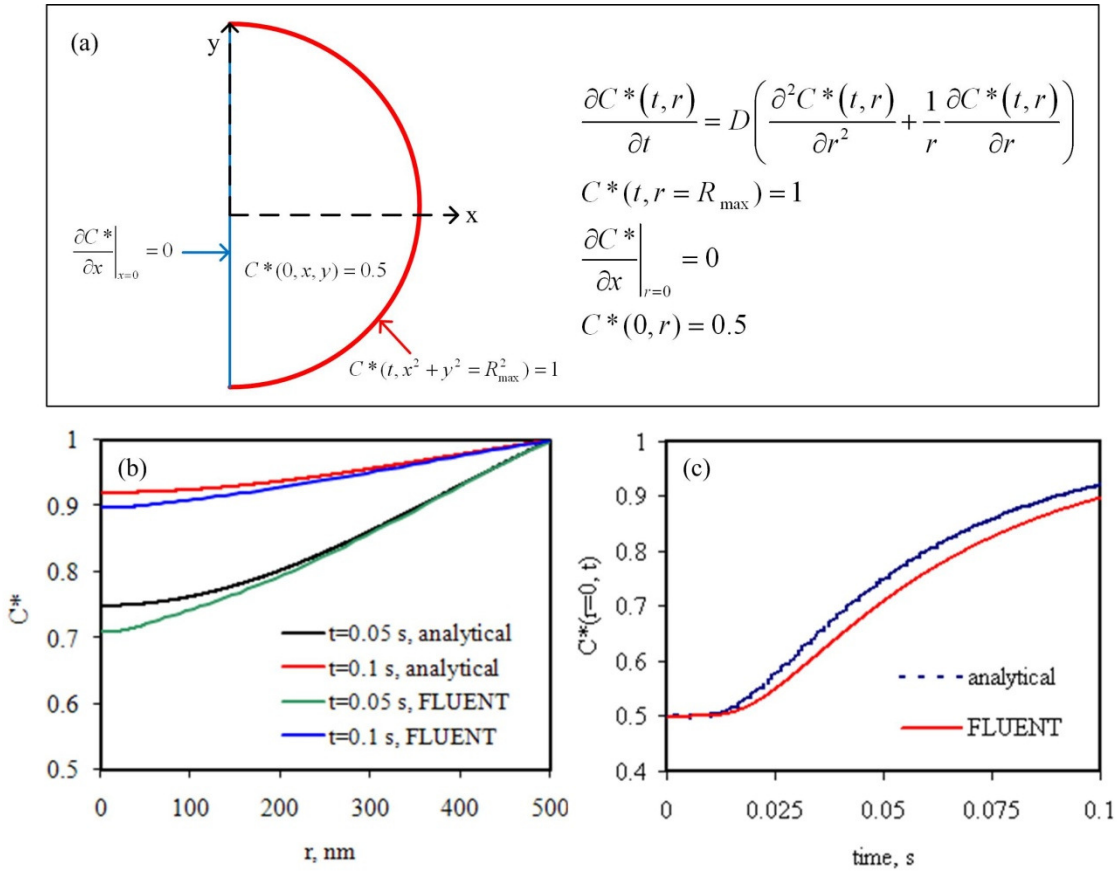

Figure 2.10.(a) Schematic of the mass transport test case and mathematical description of the related one dimensional problem, (b) Simulated and analytical solution of concentration spatial profiles of dimensionless surface concentration, and (c) Simulated and analytical profiles of dimensionless concentration at r=0 versus time.

2.3.3 Surface Mass Transport with Electron Beam Induced Reaction

Surface mass transport on a flat substrate with mass sink term specified by an electron beam induced reaction is simulated for complete model validation. Figure 2.11 shows the resulting dimensionless surface concentration spatial distribution as well as its time evolution. These results compare well with results of Rykaczewski et al. [41] obtained by solving the axi-symmetric surface transport equation for similar deposition conditions on a silicon substrate.

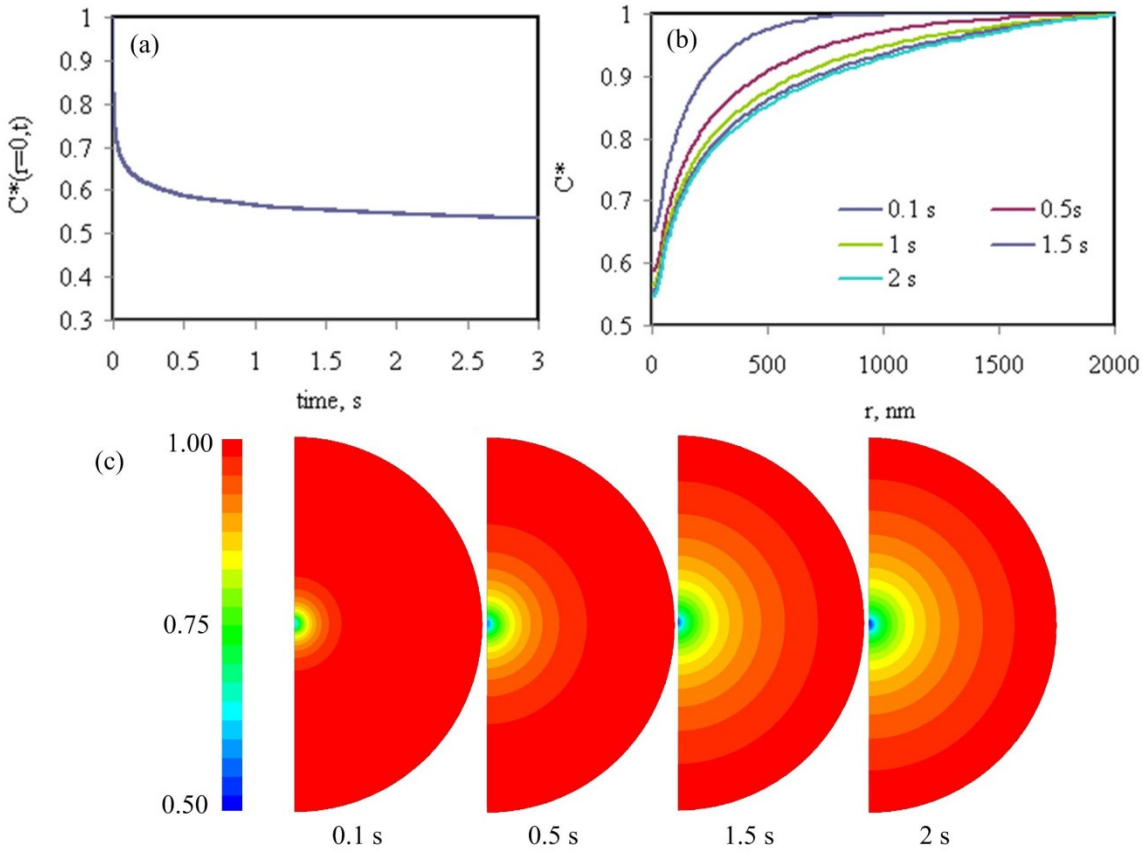

Figure 2.11. (a) Time evolution of dimensionless concentration at the center of the deposition zone versus time, (b) one and (c) two dimensional dimensionless concentration profiles for simulation of EBID amorphous carbon growth on a flat carbon target for electron beam with FWHM diameter of 100 nm, current of ~21 pA, and accelerating voltage of 25keV. An adsorbed residual hydrocarbon initial surface concentration of 6.3 ng/cm^2 and surface diffusion coefficient of 10^6 nm^2/s are assumed.

2.3.4 EBID deposit growth

Conditions for reaction-limited, diffusion-limited and mixed-growth regimes can be identified using scaling analysis. The general scaling analysis for three possible deposition cases is discussed in detail in Appendix B. Different growth regimes are defined by the relative magnitudes of the diffusion (t_{diff}) and reaction (t_{sink}) time scales associated with the STE, as well as their comparison to the observation time scale (t_{obs}) on which deposit growth occurs. Three possibilities exist:

1. $t_{diff} \gg t_{sink}$

2. $t_{diff} \ll t_{sink}$

3. $t_{diff} \sim t_{sink}$

In the first case the deposition reaction is much faster than the surface diffusion. Since the main goal of the simulation is to capture the growth rate and evolution of the deposit the observation time, t_{obs}, is of the same order of magnitude as t_{sink}. This case represents a diffusion-limited case. In the second case surface diffusion is much faster than the reaction. As in the previous case t_{obs} is of the same order of magnitude as t_{sink}. Such a situation represents a reaction-limited case. The third case is most general and occurs when both t_{diff} and t_{sink} are similar and of the same order of magnitude as t_{obs}. In this case the STE cannot be simplified and the growth rate and shape evolution of the deposit is significantly influenced by both the reaction and surface diffusion. In the following sections deposit growth for each growth regime is simulated, including formation of ring within pillar deposits, and compared to experimental results.

2.3.4.1 Deposit growth in reaction-limited, diffusion-limited, and mixed growth regimes

In order to simulate the three possible deposition scenarios a set of physical variables corresponding to appropriate relationships between the relevant time scales is selected. To represent a realistic situation primary electron beam characteristics corresponding to settings in FEI Quanta 200 ESEM are selected. At Spot Size 3 and accelerating voltage of 30keV the beam diameter is $d_{50\%}$=40 nm and beam current is ~100 pA. Since the type and amount of contamination is unique to each experimental run it is difficult to identity one dominant residual hydrocarbon which is a primary participant of the deposition reaction. Due to its well-studied adsorption chemistry acetylene on silicon case was used as a representative molecule for hydrocarbon contamination. Taylor [83] determined a monolayer saturation coverage of 0.83 for C_2H_2 on Si(100). An ideally reconstructed Si(100)-(2x1) surface exposes 3.4×10^{14} Si_2 cm^{-2} as dimer sites [83]. For calculation of the maximum initial surface concentration it is assumed that 83% of the available dimer sites are occupied by acetylene. Based on the adsorption kinetics constants provided by Taylor, full monolayer coverage at 300K and 5×10^{-6}Torr is reached within one second. The magnitude of the surface diffusion coefficient is used as an adjustable parameter to demonstrate different growth regime possibilities.

For the specified primary beam conditions SE yield is expected to be ~0.07 (taken from Lin and Joy [81]) yielding the reactive electron time scale ~0.001s. To simulate the mixed-growth regime the diffusion

time scale is set equal to the reactive electron flux time scale. The value of the surface diffusion coefficient is solved for, yielding ~10^6 nm^2/s. For the simulation of the diffusion-limited case the surface diffusion coefficient is reduced by two orders of magnitude to ~$10^4 nm^2/s$. For the reaction-limited case the surface concentration is assumed to be uniform and constant at all times to reduce the simulation time required. Total deposition time is 2.1s in each simulated case, which required 15,000 integration cycles with a time step of 140μs. The reactive electron flux is calculated from an average of 150,000 primary electrons.

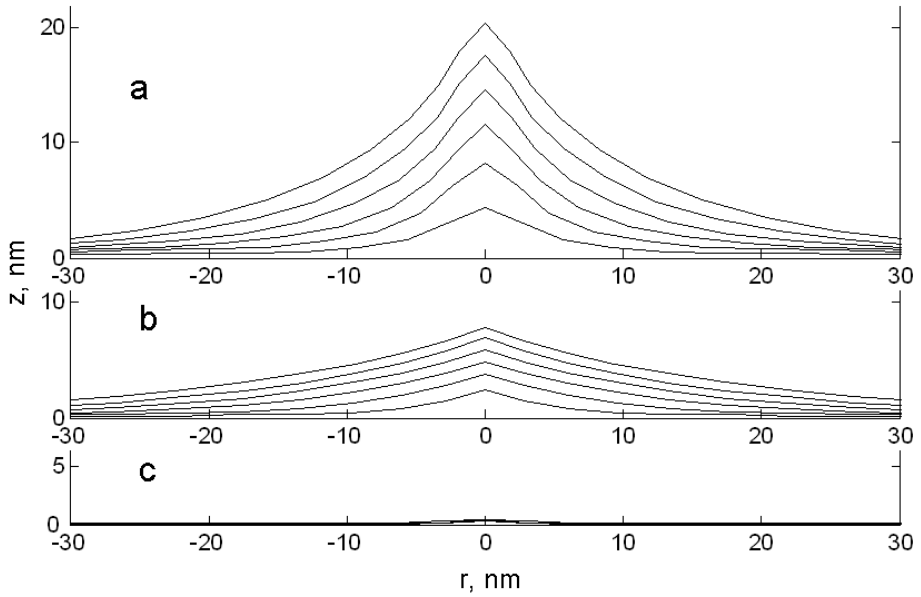

Figure 2.12.Transient evolution of the EBID deposits for the three growth regimes of (a) reaction-limited, (b) mixed (reaction-diffusion), and (c) diffusion-limited cases, shown in steps of 0.35 s [41].

The evolution of the deposit has been simulated for the reaction-limited, mixed (diffusion-reaction), and diffusion-limited cases, and results are shown in Figure 2.12a, Figure 2.12b, and Figure 2.12c, respectively. The corresponding precursor concentration profiles are only shown for the mixed (Figure 2.13a) and diffusion-limited (Figure 2.13c) cases (the precursor concentration in the reaction-limited case remains constant at all time, and therefore is not plotted). As expected, the maximal average vertical growth rate is achieved in the case of the reaction-limited deposition and is equal to ~9.7 nm/s. In the case of mixed (diffusion-reaction) deposition, a decrease in the precursor supply to the reaction zone starts

playing a role, leading to a decreased average vertical growth rate of ~3.7 nm/s (Figure 2.13b). The simulation of the diffusion-limited regime resulted in slowest growth and formation of a thin film within the deposition area. Because of the severely restricted replenishment of the deposition area with new precursor molecules, a thin film deposit is formed due to decomposition of the reagent initially present on the surface.

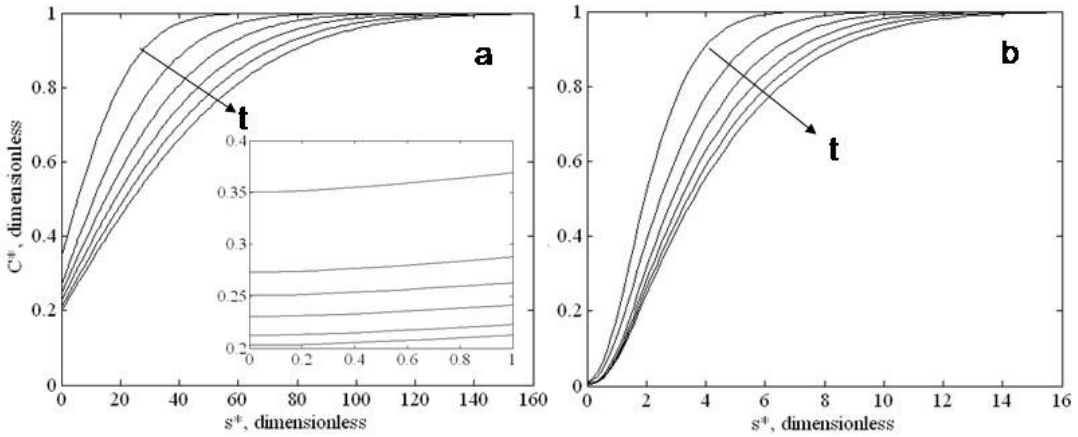

Figure 2.13. Concentration profiles for the (a) mixed (diffusion-reaction), and (b) diffusion-limited deposition regimes shown in steps of 0.35 s. The inset in (a) is a magnified view of the concentration field in the vicinity of the symmetry axis of the deposit, clearly showing vanishing gradient of concentration at r=0 [41].

Figure 2.14 illustrates a drastic difference in the amount of precursor available for deposition reaction for different growth regimes by showing the precursor concentration at the centerline (middle of the deposition area) as a function of time. In addition to a much reduced magnitude of concentration as deposition becomes more diffusion-limited, as it is clearly seen in Figure 2.13b and Figure 2.14, the dynamics of decay is also much faster in the case of the diffusion-limited growth, leading to further reduction in the growth rate of the deposit. For all growth regimes, the value of the precursor concentration in the deposition area reaches a quasi-steady state value within a few seconds of start of the deposition process. By taking this fact into account, one could reduce the complexity of the simulation in the later stages of the deposition process, by assuming a constant and uniformly reduced precursor concentration within the deposition area.

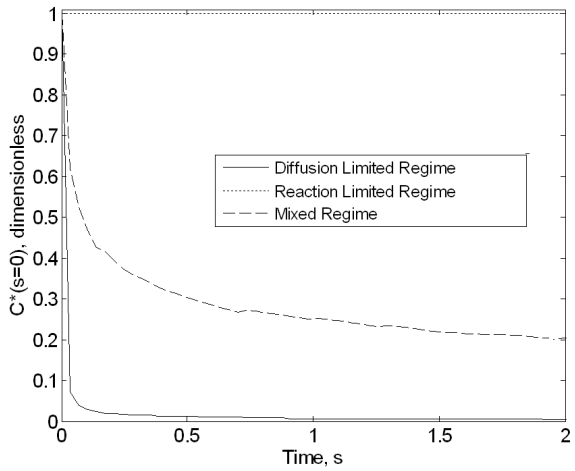

Figure 2.14. Precursor concentration at the centerline (middle of the deposition area, r=0) as a function of time for the three growth regimes [41].

Nanostructures formed in different deposition regimes not only grow at different rates, but also are different in shape. As shown in Figure 2.15, when mass transport becomes a physical mechanism that limits deposition, not only it takes much longer to deposit the same amount of the material, but also broadens the shape of the deposit. This leads to much better spatial resolution (tall and narrow structures) for the purely reaction-limited growth, and not as good resolution for the mixed (i.e., broad base, short structures shown in Figure 2.15) and especially for the purely diffusion-limited growth, resulting in thin film rather than nanostructure deposition.

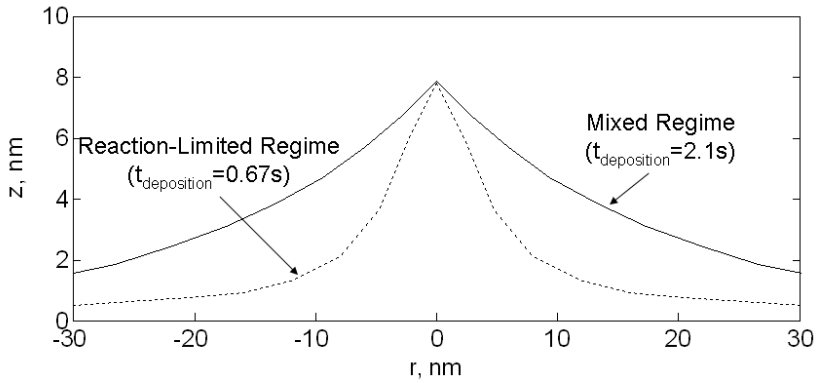

Figure 2.15. Comparison of deposit shapes simulated for the reaction-limited and mixed (diffusion-reaction) regime grown to the same height. The growth of the mixed regime deposit takes much longer (0.67s) as compared to that (2.1s) for the reaction-limited deposit [41].

Lastly, three-dimensional deposit growth in the mixed (diffusion-reaction) reaction regime is simulated. The resulting evolution of the surface concentration and height of the deposit in the center of the deposition zone, as well as the deposit cross section and final shape, are presented in Figure 2.16. While the shape of the deposit matches well the axi-symmetric results presented above [41], the growth rate of the deposit is significantly higher. It is important to note that a grid independent solution is achieved only when an extremely small mesh is used. The computational requirements for both the MC electron transport and generation as well as for the FLUENT mass and growth simulations for such small mesh scale are difficult to implement. Thus, the presented three-dimensional growth simulations are only qualitative in respect to time. Further details of simulations are given in Appendix D.

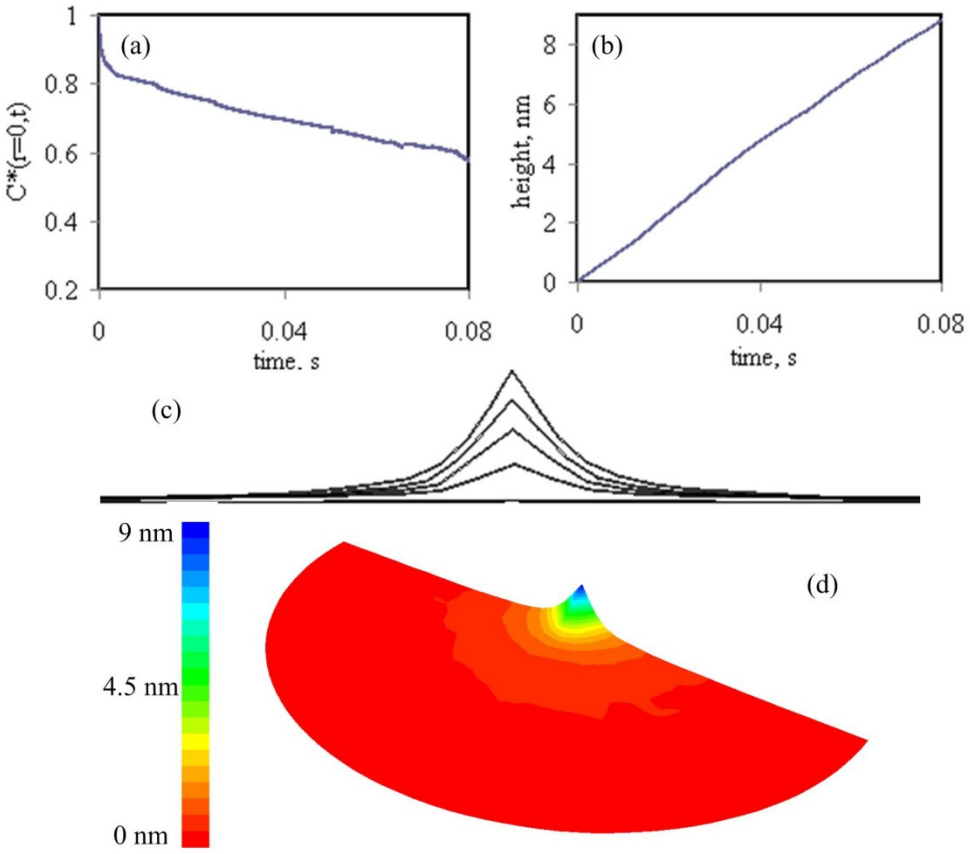

Figure 2.16. (a) Time evolution of dimensionless concentration at the center of the deposition zone versus time, (b) Time evolution of height of the deposit in the center of the deposition, (c) Corresponding cross sections of the deposit shape in steps of 0.002s, and (d) Isotropic view of the topography of the deposit at t=0.08s for simulation of EBID amorphous carbon growth on a flat carbon target for electron beam with FWHM diameter of 100 nm, current of ~21 pA, and accelerating voltage of 25keV. An adsorbed residual hydrocarbon initial surface concentration of 6.3 ng/cm^2 and surface diffusion coefficient of 10^6 nm^2/s are assumed.

2.3.4.2 Pillar-within ring deposit growth

Inserts in Figure 2.17c and Figure 2.17d show AFM images of a nanopillar-within-a-micro-ring deposit formed by EBID with accelerating voltage of 15keV, beam current of 376 pA, and deposition time of (c) 5 minutes and (d) 25 minutes. During the early stage of the deposition process only the dot/pillar like nanostructures are produced at the point of impact of the electron beam.

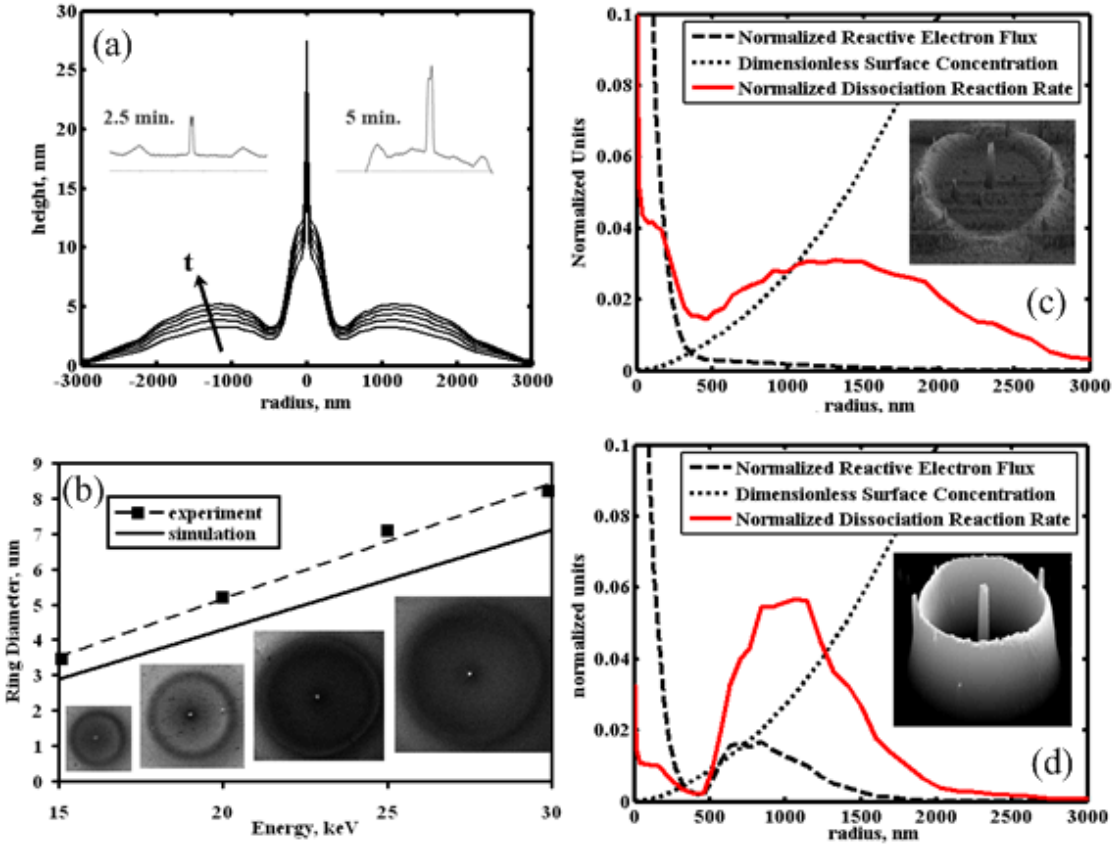

Figure 2.17. (a) Transient deposit profiles predicted in time steps of ~45 seconds (final deposition time of 5 minutes). The inset in top right corner shows AFM profiles of the corresponding rings deposit formed via EBID with accelerating voltage of 15keV, beam current of 376 pA measured at 5 minutes, (b) Comparison between experiments and theoretical predictions of the micro-ring deposit diameter as function of the beam accelerating voltage. Insets show SEM images of corresponding ring deposits for electron beam accelerating voltages 15, 20, 25, and 30 kV, (c)-(d) Illustration of ring formation mechanism by showing radial distribution of normalized reactive electron flux, dimensionless surface concentration of precursor molecules, and normalized dissociation reaction rate for (c) initial deposition and (d) 5 minutes into deposition. The insets show 3D AFM image of the corresponding ring and pillar deposits at (a) 5 minutes and (b) 25 minutes into the deposition process [39].

In later stages, a secondary ring-like deposit began to form around the initial deposit. Specifically, at the 5-minute deposition time the height of the ring deposit (~8 nm) is less than half of the center pillar height

(~20 nm). However, at the 25-minute deposition time both the ring and center deposit reach about equal height of ~90 nm. As shown in Figure 2.18, the height of the center-located deposit increased linearly with time, while the peripheral ring grew at an increasing rate with time. Diameter of the deposited micro-ring shows linear dependence on the electron beam accelerating voltage, increasing from ~3.5 μm to ~10 μm as the voltage increases from 15 keV to 30 keV (Figure 2.17b)

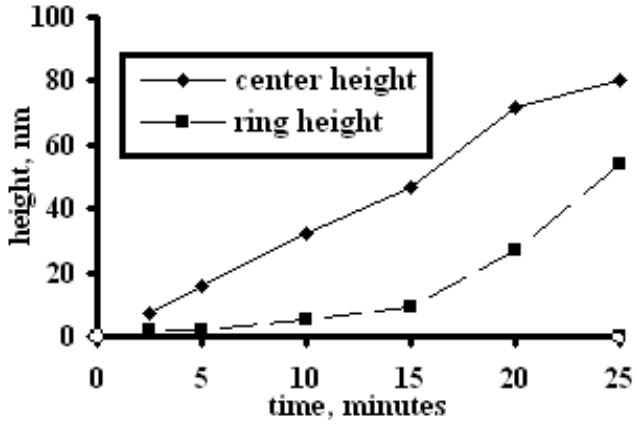

Figure 2.18. Height of the pillar and ring deposits as a function of time [39].

Early growth deposition is simulated using one million primary electrons impinging on a Si(100) substrate. The estimates for initial concentration ($C_0 = C_\infty \approx 0.25\ \mu g/cm^2$) and surface diffusion coefficient ($D \approx 7.5x10^4\ nm^2/s$) of the adsorbed residual hydrocarbons are obtained by calibration of simulated results against experimentally observed growth of the central nano-pillar. Figure 2.17a shows deposit profiles predicted in time steps of ~45 seconds with a final deposition time of 5 minutes for the beam accelerating voltage of 15 keV and electron beam diameter (full width at 50%) of 200 nm. The final simulated heights of ~6 nm and ~25 nm for the ring and center deposit, respectively, correspond well to the experimental observations. To better illustrate the mechanism of ring formation Figure 2.17c shows the spatial distribution of the scaled reactive electron flux ($\dot{Q}_1$), dimensionless precursor concentration ($C(s,t)$), and the resulting dissociation (deposition) reaction rate given by a product of the former two terms. Formation of the ring deposit in Figure 2.17a can be now readily explained by the secondary peak of the dissociation (deposition) reaction rate at around radius *r*~1500 *nm*, resulting from convolution of the secondary and backscattered electron distribution and the concentration profile of adsorbed precursor

molecules established by surface diffusion.

To investigate the effect of the beam energy, the dissociation (deposition) reaction rates for accelerating voltages of 15, 20, 25, and 30 keV are also simulated. Consistent with experimentally observed growth of carbon micro-rings, the radial distance between the center of the electron beam and the predicted secondary reaction rate peak increases linearly with an increase in accelerating voltage. Experimental data and simulation results are compared in Figure 2.17b. The concentration of surface adsorbed precursor molecules near the center of the electron beam reaches a quasi-steady state within a short time period after beginning of the deposition process. The time necessary to reach the quasi-steady state depends on the surface diffusion coefficient *D*, magnitude of the reactive electron flux $\dot{Q}_1$, and the initial precursor concentration C_0 [41]. For the set of EBID condition used in our experiments, a quasi-steady state concentration is reached within ~30 seconds from the beginning of the deposition process. Changes in the reactive electron flux distribution depend on the growth rate of the deposit, which occurs on a much longer time scale (~minutes) than the changes in the surface concentration (~seconds). Thus, beyond the initial transient surface spreading of the precursor, both the local surface concentration and reactive electron flux in the center of the deposit do not change appreciably on the ~second timescale, resulting in a constant growth rate of the central nanopilar. A constant growth rate at the center implies a linear time variation of the nanopillar deposit height, which agrees with our experimental observations.

To gain insight into later stages of the deposition process the reactive electron flux is simulated for the final shape of the deposit shown in Figure 2.17d. Figure 2.17d shows the spatial distribution of the scaled reactive electron flux ($\dot{Q}_1$), dimensionless precursor concentration ($C(t,s)$), and the resulting dissociation (deposition) reaction rate for the late stage growth of the hybrid nanopillar-microring deposit. In contrast to the initial growth, during the later stages of the growth process the dissociation (deposition) reaction rate is greater at the location of secondary peak (r~1500 nm) than in the center of the electron beam. This theoretically predicted increase in the relative growth rate of the ring deposit with time, as compared to the centrally-grown nanopillar, is consistent with the experimentally observed trends.

2.4 Concluding remarks

A comprehensive dynamic model of Electron Beam Induced Deposition (EBID) of residual hydrocarbons coupling mass transport, electron transport and scattering, and species decomposition to predict deposition of carbon structures is developed. The axi-symmetric surface transport equation governing the diffusion of the adsorbed precursor species is derived based on first principles and generalized to arbitrary 3D deposit geometries. A 3D Monte Carlo electron transport and SE generation simulation combined with 2D surface mass transport enable a fully 3D deposit growth simulation. The models are validated by comparing simulation results to analytical predictions, as well as experimental and theoretical results available in the literature. Qualitative agreement between simulated and experimental electron beam line scans across a MWNT on a Si substrate is demonstrated. Physical conditions for diffusion-limited, reaction-limited, and mixed (diffusion-reaction) deposit growth regimes are identified using scaling analysis and verified by simulations. The simulations are also used to predict the details of deposit growth dynamics as well as spatially-resolved evolution of the precursor concentration during the deposition process.

The results obtained from the simulations of the different growth regimes demonstrate the influence of the surface diffusion coefficient and the initial surface concentration of the precursor molecules on both the deposit shape and the magnitude of the deposition rate. The fastest growth rate as well as highest spatial resolution are shown to occur in the case of the reaction-limited growth. The difference in shape of the deposit during the initial growth period is significant and is shown to depend mainly on the rate-limiting physical process. Lastly, the model developed is used to investigate the transient formation of hybrid, topologically complex microring-nanopilar deposits. The simulation results compared well with experimentally observed topology of the ring and pillar deposits during the early stage of deposition process. Several distinct experimental trends, such as (1) linear increase in the ring diameter with electron beam energy, (2) linear increase of the height of the centrally-located nanopillars, and (3) an increasing growth rate of microring deposits during the latter stages of EBID are successfully captured and explained using the simulations. In contrast to previously reported simulations, which focus on growth predictions on the local deposition length scale (i.e., given by a diameter of the electron beam) [38, 70, 71], this work

demonstrates the capability for predicting EBID of residual hydrocarbons for the macroscopic domains whose size is two orders of magnitude greater than the local deposit scale.

CHAPTER 3

INFLUENCE OF EBID CARBON MWNT-ELECTRODE JOINT GEOMETRY AND PROPERTIES ON ITS ELECTRICAL CHARACTERISTICS

3.1 Introduction

While application of EBID of amorphous carbon for improved CNT-electrode interface has been reported [16, 17, 19, 23, 42, 47, 51, 52], little attention has been dedicated to fundamental understanding of the influence of process parameters, such as electron beam energy, current, geometry, and deposition time on the interface geometry and resistance. Since Bachtold et al. [16] demonstrated that high resolution electron beam imaging of MWNT significantly lowers its electrical contact resistance to the substrate, numerous groups [8, 17, 18, 23, 84] have followed this empirical ah-hoc approach. The accelerating voltages and currents used vary from 5 kV and 7 pA [17] to 20 kV [16] and 100 pA [21]. The characterization of the EBID amorphous carbon interface has been limited to electrical [16, 17, 19, 23, 42, 47, 51, 52] and structural (TEM imaging [8, 44]). Yoshikawa et al. [84] determined that while the EBID-made carbon interface comprises of a tunneling and ohmic resistance, at room temperature and above the tunneling resistance can be neglected.

The total measured resistance of a MWNT interconnect is equal to the sum of the individual resistances of each of the components as shown in Figure 2.19. According to Slade [85] electrical contact resistance, $R_{contact}$, is equal to the sum of the constriction resistance and interfacial film resistance. In case of a MWNT interconnect with an amorphous carbon joint, two interfacial films can contribute to the contact resistance: at the amorphous carbon joint-MWNT interface ($R_{aC\text{-}MWNT\ \text{interface}}$) and at the amorphous carbon joint-metal electrode interface ($R_{aC\text{-}metal\ interface}$). If the joints on both ends of the MWNT are assumed to be identical, the total resistance of a MWNT interconnect, R_{total}, equals:

$$R_{total} = 2R_{\text{aC-MWNT interface}} + 2R_{\text{aC}} + 2R_{\text{aC-metal interface}} + 2R_{\text{spreading}} + R_{\text{MWNT}} \qquad 2.19$$

Here R_{aC} is the constriction resistance of the amorphous carbon joint itself, $R_{spreading}$ is the spreading resistance of the metal electrode (on a deposition substrate), and R_{MWNT} is the resistance of the MWNT. The location of each of the components contributing to R_{total} is schematically shown in Figure 2.19.

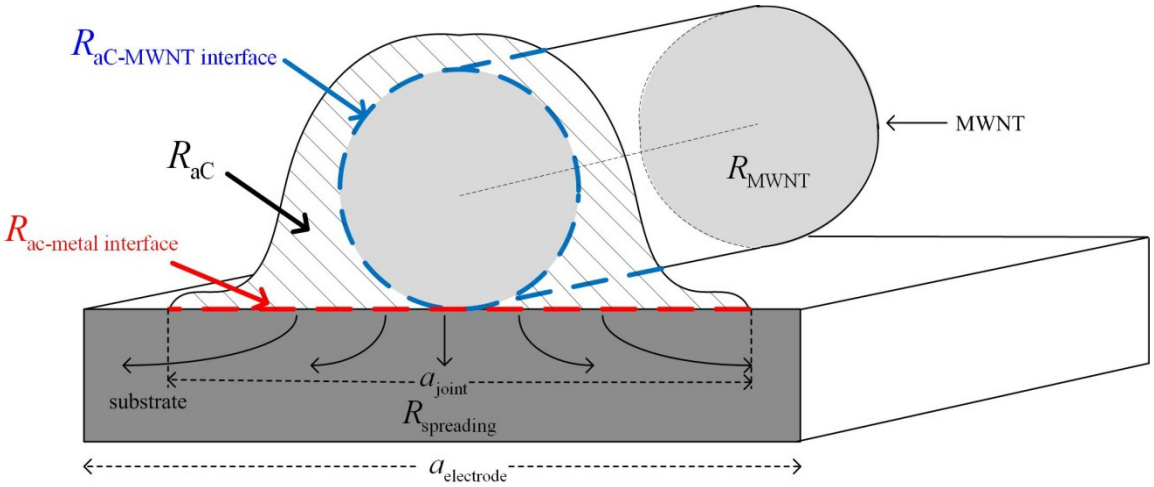

Figure 2.19. Schematic representation of the components contributing to the R_{total}.

In the first part of this Chapter the MWNT interconnect fabrication procedure and the influence of the electron beam on electrical characterization of the MWNT interconnects are described. The rest of the Chapter focuses on experimental study of the influence of the geometry and properties of the carbon joint on the contact (and thus the total) resistance of a MWNT interconnect. The relative importance of each of the components and the limiting factor in total resistance of an interconnect are determined.

3.2 MWNT interconnect fabrication procedure

3.2.1 Metal electrode fabrication

The 100 nm thick chromium electrodes on top of a 2 μm insulating silicon oxide layer are fabricated on a silicon wafer using standard photolithography techniques [86]. Several other groups [7, 51, 52, 87] have taken a similar approach with metal electrode material varying from platinum [2] to aluminum [7]. The electrodes are designed such that both the fixed [52] and the floating point dielectrophoretic (DEP) [87] alignment experiments are possible. Seven devices (inset in Figure 2.20b) with twelve possible interconnect sites in each device with varied electrode width and spacing are fabricated on a single wafer.

3.2.2 MWNT selection

To ensure high quality of the MWNT, samples from six different companies are procured and compared. Specifically, the MWNT samples with varied averaged diameters and lengths from Cheap

Tubes Inc. [88], Catalytic Materials [89], Nanostructured and Amorphous Materials [90], SES Research [91], Nanolab [92], and Helix Materials [93] companies are investigated. The MWNT samples are evaluated using micro-Raman analysis and SEM inspection. The G (at ~1589 cm^{-1}[94]) to D (at ~1321-1341 cm^{-1} [94]) band Raman intensity ratio of the MWNT sample is a good indicator of the number of structural defects present [95]. The MWNT with diameters of 100-150 nm from Cheap Tubes Inc are found to have the highest G/D band ratio, and also the best quality from the SEM images. The Raman spectra and SEM images of the selected MWNT are shown in Figure 2.20a.

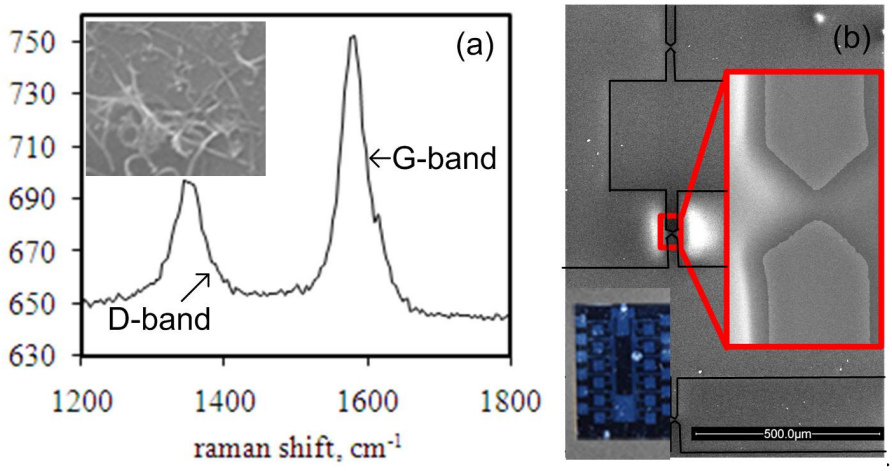

Figure 2.20. (a) Raman Spectra of the selected MWNT [88] (inset on the right shows the corresponding SEM image), (b) SEM images of typical fabricated electrodes (inset on the left shows a set of twelve electrodes).

3.2.3 MWNT Purification

As purchased, the MWNTs contain residual metal catalyst particles. In order to rid of these contaminants, the MWNT powder is purified using procedure outline by Ko et al. [96]. Specifically the MWNT powder is refluxed in nitric acid for 48 hours and centrifuged five times at 5000 revolutions per minute for 10 minutes. Figure 2.21 shows Electron Dispersive Spectroscopy (EDS) of the tube powder before and after purification. As demonstrated by the EDS spectra, the purification procedure effectively removes iron and nickel catalyst contamination.

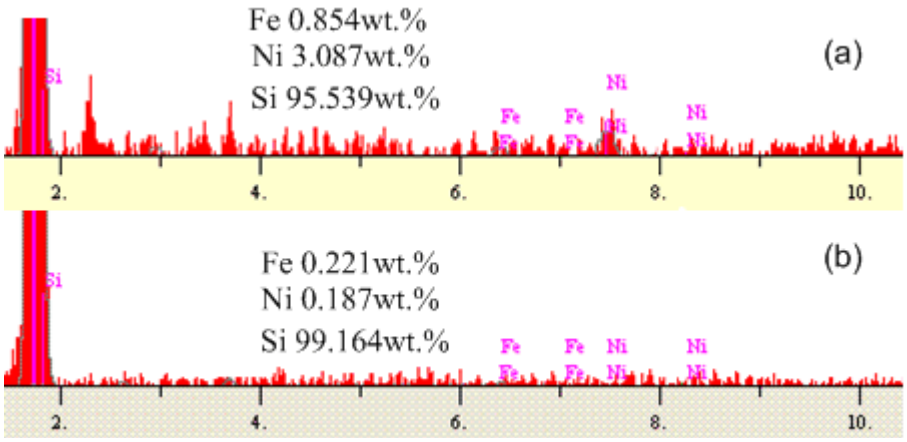

Figure 2.21. Electron Dispersive Spectroscopy (EDS) spectra of (a) unpurified and (b) purified MWNT.

3.2.4 MWNT powder dispersion

Several different methods of MWNT powder dispersion are tested. Best results are obtained by placing a trace amount of MWNT powder in solutions of ethanol [7], 1% Sodium Dodecyl Sulface (SDS)-deionized water (DI) [87], and Dimethylformamide (DMF) and ultrasonicating the solution for a period of 15-25 minutes. The ethanol-dispersed MWNT are difficult to work with because the solution wets the surface of the electrodes and evaporates too quickly for the DEP alignment to work. Also, SDS is known to form a thin coating over the MWNT [97], which has to be removed by soaking of the aligned tube in dionized water for 30 minutes [87]. In contrast, DMF evaporates quickly and does not contaminate the surface of the MWNT. To simplify the fabrication procedure and reduce amount of possible MWNT contamination, DMF is used.

3.2.5 Dielectrophoretic MWNT alignment

The procedure for DEP CNT alignment [51] consists of placing a small droplet of the MWNT solution in a region containing electrodes and applying DC, AC, or DC-AC voltage signal for a short period of time to “active” electrode, while grounding the second electrode and allowing the third electrode’s potential to float [98]. If the strength of the non-uniform interelectrode electric field is sufficiently high to overcome Brownian motion [51], the CNT align themselves between the “active “ and “floating” electrodes [87].

Song et al.[51] and Subramanian et al. [52] found the DEP alignment process to be sensitive to the electrode gap, an applied voltage, the MWNT solution concentration solution, a droplet size, and a duration of the process. The final DEP procedure utilized in this work consists of the following steps:

- Fine needle injects a 1-2 μL droplet of the MWNT-DMF solution in a region containing several chromium electrodes (solution MWNT concentration: 1-10 μg/mL, electrode spacing: 1-5 μm);
- AC voltage signal is applied with frequency of 5 MHz and peak-to-peak voltage of 1-10 V for period of 1 minute;
- Residual droplet is removed to avoid excessive tube deposition [52]

As shown in Figure 2.22, some of the tubes become align and bridge a gap between the electrodes.

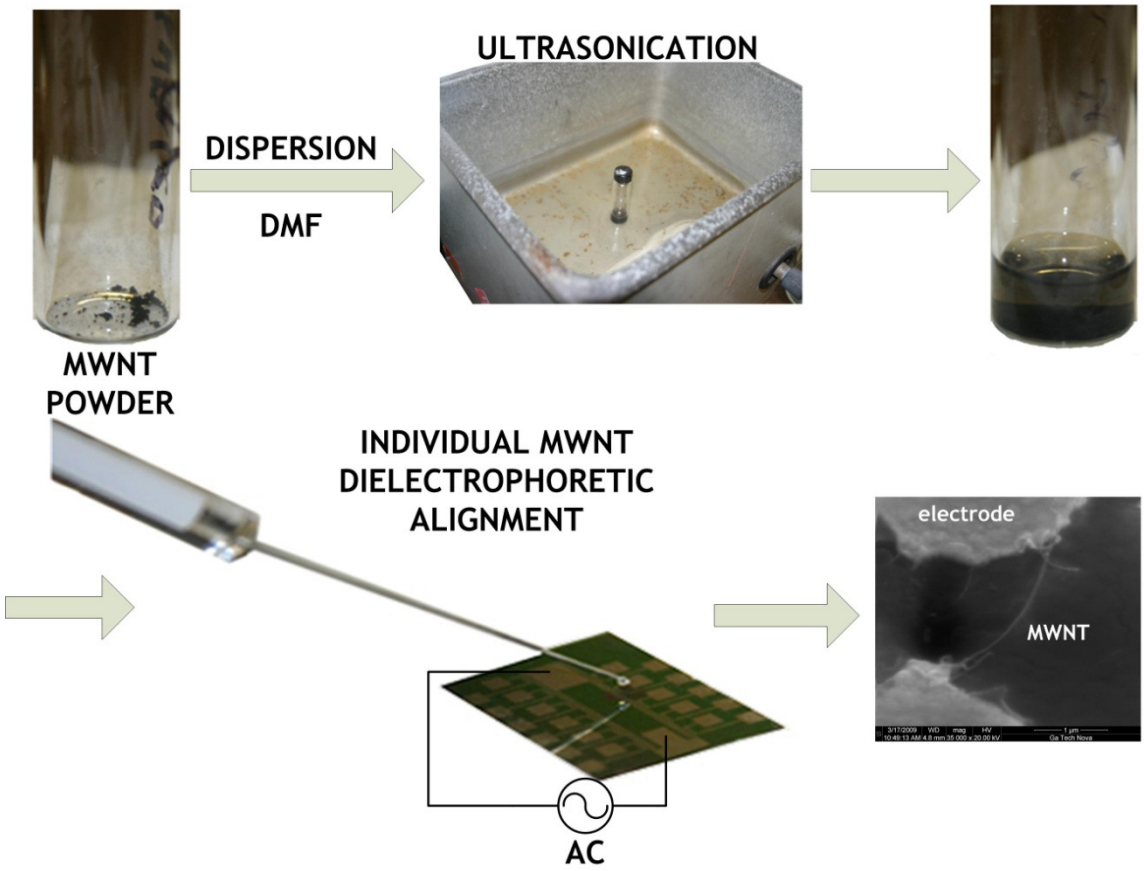

Figure 2.22. Schematic of MWNT dispersion and DEP alignment procedure.

3.2.6 MWNT end opening

The fact that most of MWNTs are capped at the ends [99] prevents establishment of electrical connection with the inner shells of the tube. Annealing [99, 100], chemical etching [101, 102], high energy electron beam [103], water assisted electron beam etching [104] and focused ion beam (FIB) [105] cutting have been tried in cutting of MWNT. According to Tsang et al. [101], chemical etches indiscriminately damage all high curvature regions of CNTs and are difficult to control. In this work three methods for MWNT opening are tested. First, the MWNT powder is annealed in air at a temperature of 550˚C. Annealing at a higher temperature, even for a short period of time, results in complete destruction of the tubes. While attractive due to its simplicity, this method results in sporadic opening and cutting of the tubes. Second, water assisted electron beam etching of aligned MWNT is tested.

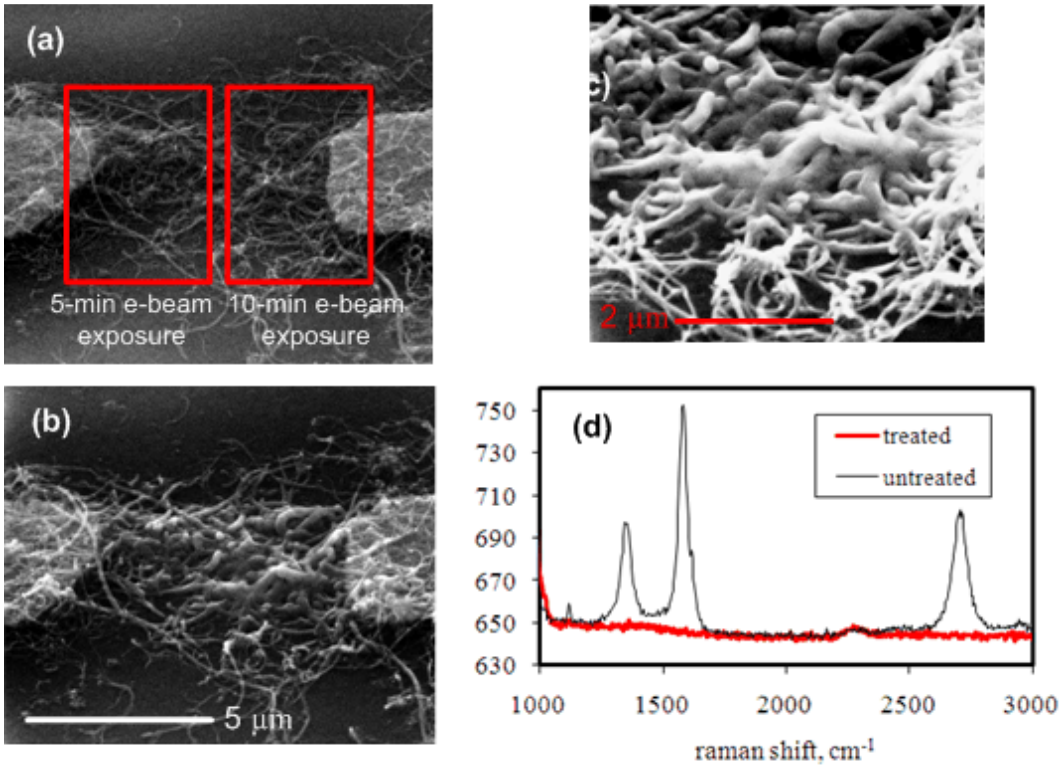

Figure 2.23. (a) Untreated multiple MWNT aligned between two electrodes with regions to be exposed to electron beam for 5 and 10 minutes indicated, (b) post-exposure SEM of the same region, (c) close up SEM image on the 10 minute exposure region, (d) Raman spectra corresponding to untreated and treated MWNT. (Raman measurements were performed by Dhaval Kulkarni and Srikanth Singamaneni from Professor Tsukruk's group at Georgia Institute of Technology)

Different water vapor-nitrogen and water vapor-air mixtures are injected into the SEM chamber using a very fine needle. Simultaneous gas mixture injection and electron beam exposure of the MWNT alters the structure of the MWNT and unfortunately does not result in localized cutting of the tubes. Figures 3.5a and 3.5b show typical before and after SEM images, respectively, of MWNT exposed to water vapor and electron beam for a period of five and ten minutes. As confirmed by Raman spectroscopy (Figure 2.23c), this treatment results in complete loss of crystallinity of the MWNT.

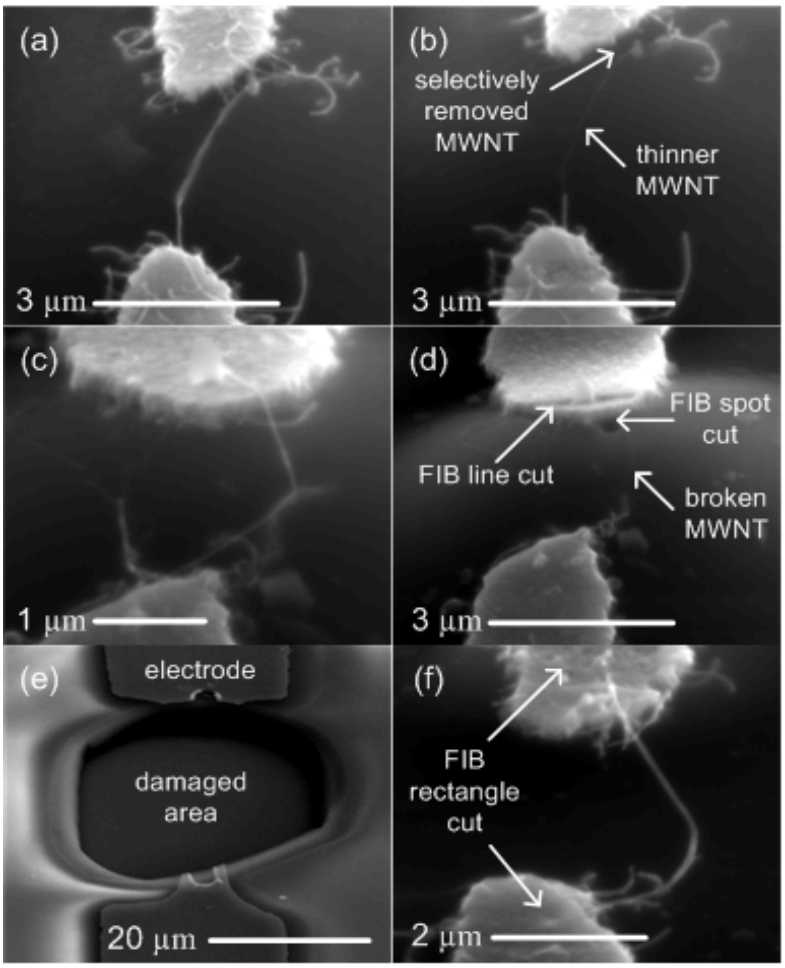

Figure 2.24. SEM images showing various damage to the MWNT due to the direct and secondary ion exposure before (a, c) and after (b, d, f) FIB milling (e) FIB induced delamination of silicon oxide layer..

Finally, localized FIB cutting of the MWNT is tested. The MWNT are cut with high precision using Gallium ions beam with energy of 30 keV and current of 23 pA (Figure 2.24). As shown in Figures 3.6a and 3.6b, the unwanted MWNT are selectively cut away. Unfortunately, secondary ion exposure of other

parts of the MWNT, a side effect of the FIB milling process, results in significant damage to the MWNT and degradation of its electrical properties (extremely high resistance). The FIB induced damage to MWNT is displayed through significant thinning of the MWNT (Figure 2.24b) or breaking of the tube (Figure 2.24d). However, even seemingly undamaged MWNT, such as one in Figure 2.24f, are internally damaged and do not conduct current after the FIB milling. In addition, ion exposure of the electrode region often causes localized delaminating of the silicon oxide layer and destruction of electrodes (Figure 2.24e). In summary, all three methods for MWNT end opening fail to yield reproducible results, and therefore electrical measurements are performed on closed-ended MWNT.

3.3 Electrical resistance measurements

3.3.1 Experimental set up

As shown in Figure 2.25, the FEI Quanta 200 ESEM is modified so that a DC voltage signal can be applied between electrodes, and the resulting current is measured using Keithley 6485 Picoammeter in situ during the operation. The current data are directly imported into Microsoft Excel using the ExcelLINK program.

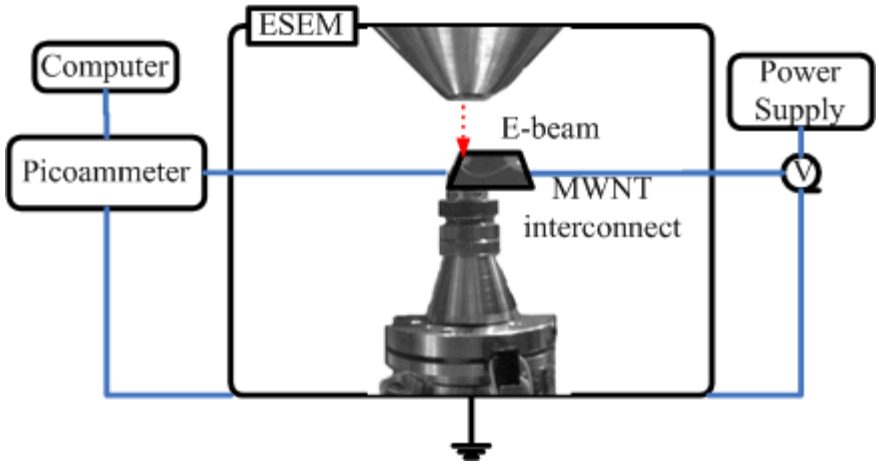

Figure 2.25. Schematic of the modified FEI Quanta 200 used for in-situ current measurements.

The electrical measurements are performed in two ways. In the first method, a desired input voltage is applied and the resulting current is recorded during the deposition process. This in-situ approach has been previously applied by Ando et al. [23] and Madsen et al.[42]. In the second method, a set of current vs.

voltage data is collected in vacuum, but with the electron beam turned off. To measure changes in resistance of the carbon joint, the procedure is repeated after each consecutive stage of the deposition process. Next two sub-sections describe the voltage selection procedure for the in-situ experiments, and the influence of the electron beam on in-situ current measurements.

3.3.1.1 Voltage difference adjustment for in-situ current measurements

Figure 3.8 shows a typical current versus time measurement for EBID carbon joint formation. The results obtained compare well to those of Ando et al. [23] and Madsen et al. [42]. In this case EBID is performed at an accelerating voltage of 25 keV, spot size 3, high vacuum conditions (~10^{-6} Torr) and a fixed electrode DC bias of ~1.5 V. Biasing of substrate with low (~2-5 V) voltage does not significantly impact the electron scattering and generation process [106], but an induced increase in the surface temperature can significantly impact the surface diffusion coefficient, mean surface lifetime, and sticking coefficient of hydrocarbon precursor molecules [107]. Focusing the electron beam on small areas surrounding the ends of MWNT for 10-20 minutes gradually increases the measured current (corresponding to a gradual decrease in the contact resistance due to a build-up of the carbon deposit) until a drastic drop in resistance is observed. According to Banhart et al. [44], Yoshikawa et al. [84], and Kahng et al. [8] this change can be attributed to the Joule heating-induced partial or full graphitization of the deposited amorphous carbon.

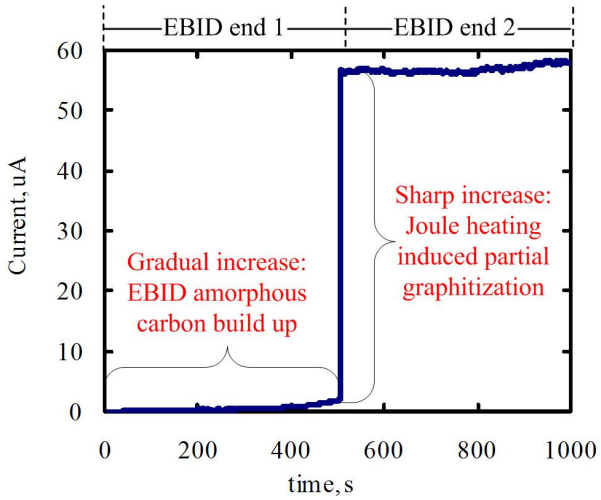

Figure 2.26. Typical current vs. time measurement of EBID carbon MWNT-electrode interface.

In order to deconvolute the change in resistance of the carbon joint due to geometrical factors and the properties of the deposited material, the in-situ measurements are performed at a lower bias voltage. Before deposition experiments, the DC voltage difference between metal terminals connected by MWNT is adjusted to a certain value (V_0), so that the resulting current is on the order of few hundred picoamps. The V_0 value depends on the initial resistance of the MWNT interconnect and ranges from 0.05 to 2 V. Following the approach of Kahng et al. [8] and Yokishiwa et al. [84], the changes in the material properties due to Joule heating are studied after the deposition process. Specifically, the bias voltage across the interconnect is gradually increased until a sharp increase in the current, corresponding to the graphitization of the amorphous carbon, is observed. The effects of Joule heating on the resistivity and composition of amorphous carbon are presented in sections 3.3.4 and 3.4.

3.3.1.2 Influence of electron beam on electrical measurements

Influence of the electron beam on in-situ electrical measurements is investigated. The electron beam contributes to the measured current in two ways. First, a fraction of the impinging primary electrons are scattered within a tube and add directly to the measured current. Second, the impinging primary electrons contribute indirectly to the measured current by generation of multiple secondary electrons during inelastic collisions within the material. In the next two sub-sections the extent to which the primary electrons alter the in-situ current measurement is analyzed using experimental measurements.

3.3.1.2.1 Direct Contribution of the Primary Electrons

Figure 2.27 shows current versus time measurement corresponding to the gap bridging deposition experiment shown in the inset. Initially, the measured current is negative and corresponds to the number of primary electrons impinging on the substrate minus the number of backscattered and secondary electrons [108]. As a metal-to-tube connection begins to form, the flow of electron from one electrode to the other increases due to applied bias voltage and dominates the current resulting from the impingement of the primary electrons from the electron beam (see results past ~850seconds in Figure 3.9).

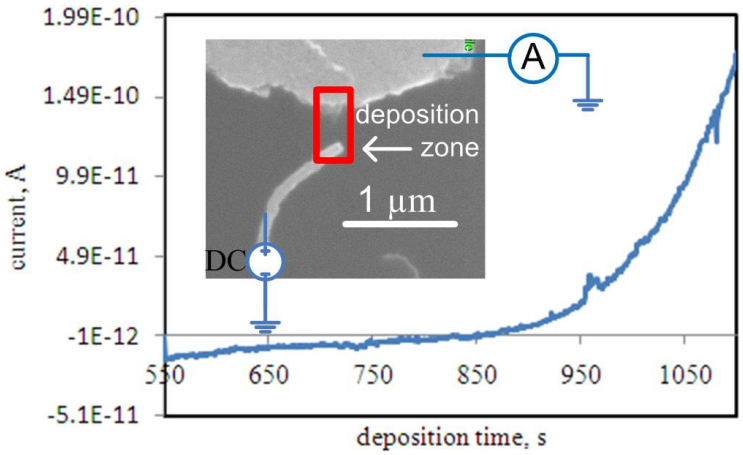

Figure 2.27. Current vs. time measurement during electrode-MWNT gap bridging experiment. Insert shows corresponding SEM image of the gap (the other end of the MWNT is connected to the second electrode).

The current due to the impingement of primary electrons is negative because the primary electrons penetrate through the thin insulator layer and are collected at the ground terminal (Figure 2.25). However, the direct contribution of the primary electrons on the measured electrical current is on the order of the electron beam current (~pA) and can be neglected when measuring much higher currents (~nA-µA) generated upon applying an external DC bias voltage between metal terminals connected by MWNT.

3.3.1.2.2 Indirect Contribution of the Primary Electrons

When scattered within a medium each primary electron undergoes multiple inelastic collisions in which low energy secondary electrons are generated. A small fraction of the generated secondary electrons emerges from the substrate. Without an external bias the rest of the generated secondary electrons reequilibrate within the substrate [108]. However, when an external bias is applied the generated electrons can migrate between the electrodes [109]. Figure 2.28 shows the time evolution of measured current during consecutive stages of a deposition process, consisting of building a sequence of square deposit blocks to bridge the gap between MWNT and the metal electrode (Figure 2.27).

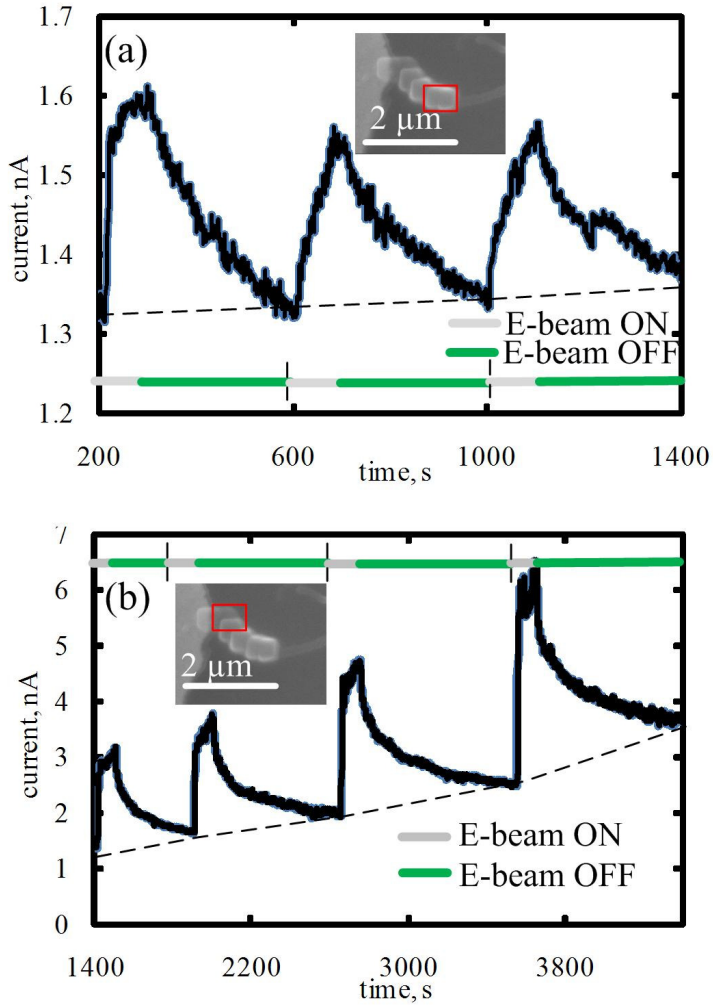

Figure 2.28. Current vs. time for consecutive stages of a deposition process consisting of building a sequence of square deposits blocks bridging the gap between MWNT and the metal electrode. Regions exposed to the electron beam are marked in SEM images in insets (a) and (b). The dashed line shows the base line current, which drifts over time.

The measured current increases when the electron beam is turned on and decreases when the electron beam is turned off, following a sharp rise and a slow exponential decay in time. As shown in Figure 2.28, this behavior is repeatedly observed during multiple electron beam on/off cycles. When the electron beam is focused on the amorphous carbon bridging connection between MWNT and a metal electrode (Figure 2.28b), the baseline current (the steady current value at the end of each decay cycle) gradually increases.

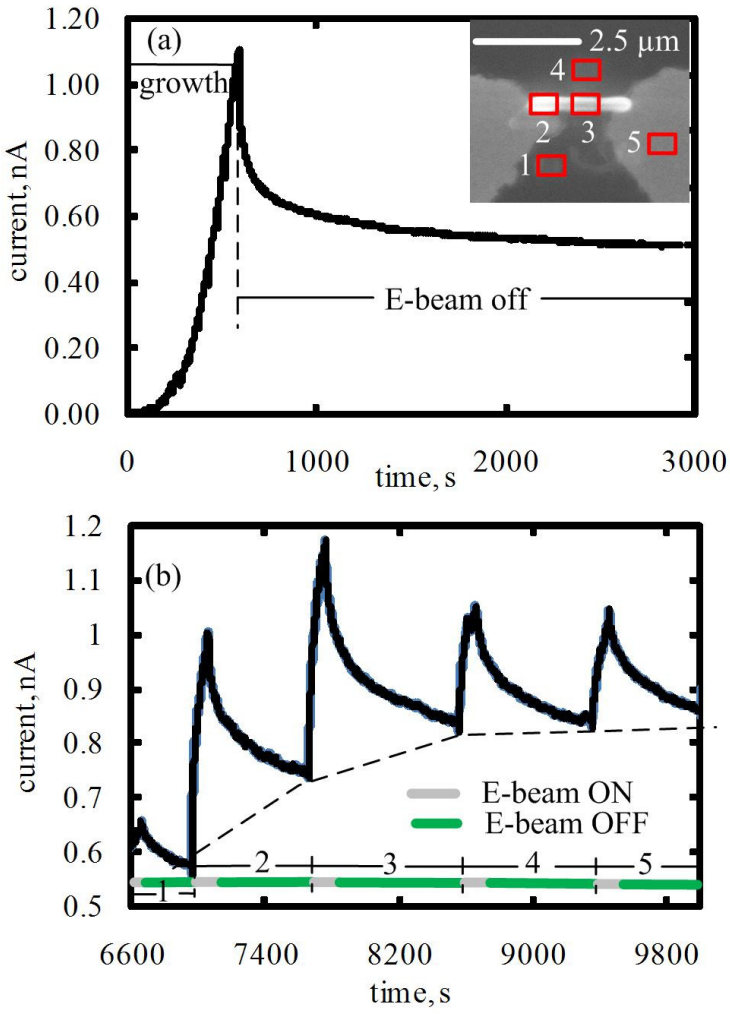

Figure 2.29. (a) Current vs. time measurement for Platinum line deposition experiment, (b) Current vs. time resulting from turning the electron beam on and off in various regions on and around the Platinum line. Regions exposed to the electron beam are marked in SEM image in insets in (a). The dashed line shows the baseline current.

An increase in the current corresponds to a decrease in the resistance of the bridge due to the extra amorphous carbon deposition. At the same time, the baseline current in Figure 2.28a does not appreciably increase because the deposition occurs on top of the already low resistance MWNT. The current vs. time evolution is also studied during deposition of a Platinum line between two metal electrodes with constant electric potential bias across. The electron beam is turned on during the deposit growth process, and then intermittently turned on and off while focusing on different regions of the deposited line (when Pt-

containing precursor is no longer supplied into the chamber of the SEM). As shown in Figure 2.29a, the electric current increases during the growth of the line and decays exponentially when the beam is turned off. As shown in Figure 2.29b, the baseline current increases only when electron beam is focused on a Platinum line. As in the bridging gap experiment, the increase in the baseline current can be attributed to lowering the resistance of the conducting line due to extra material deposition. Similar experimental trends have been recently observed by Porrati et al.[110], who attributed the exponential decay of the current when an electron beam is turned off to migration of the extra injected primary electrons towards the electrode. However, the Porrati's hypothesis cannot explain the above experiments because the current due to the injected primary electrons is orders of magnitude lower than the measured current. On the other hand, each primary electron undergoes multiple inelastic collisions and produces multiple low energy electrons. For example, a primary electron with energy of 25 keV scattering within silicon substrate has a penetration depth of ~6 μm and can undergo several hundred collisions before losing all its energy. The magnitude of the observed decay current suggests that it is due to mostly the generated, not primary, electrons. To explain the long exponential time-decay it can be noted that the EBID deposited material acts as a charge capacitor. The capacitive element is charged during electron injection and slowly discharges when the beam is turned off, providing a transient capacitive-like current rise and decay over the baseline DC current.

Irrespective of the physical mechanism responsible for transient changes in measured current, in-situ current measurements cannot be used for quantitative determination of the changes in the MWNT interconnect resistance. The in-situ current trends can only be utilized as a qualitative measure of the relationship between EBID carbon deposit and the resistance of the formed joint between MWNT and a metal pad. To avoid measurement distortion, quantitative resistance measurements must be taken before and after each deposition step. Specifically, the DC current vs. voltage data are taken at least ~10 minutes after the electron beam is turned off and the DC current reaches its steady-state value.

3.3.2 Cone-shaped carbon joint deposition experiments

The change in MWNT interconnect resistance due to deposition of conical amorphous carbon joints is

investigated. Figure 2.30 shows typical in-situ current and step-wise resistance measurements, and the corresponding top view SEM images of the carbon joints (the entire interconnects are shown in Figures 3.12c and 3.12d). As demonstrated in Figure 2.30a, the in-situ measured current scales linearly with the deposit diameter. The trend is quantitatively confirmed by the fact that the total resistance of an interconnect scales with the inverse of the diameter of the deposit (Figure 2.30b).

The effect of the electron beam energy and current is also investigated. In each case the experiments are performed on MWNT with diameter of ~50-100 nm for total deposition time of 5 minutes. The time necessary for the current to reach 90% of its value 5 minutes into the deposition process, $t_{90\%}$, is used as a comparison measure for the different settings. Figures 3.13a and 3.13b show the dependence of $t_{90\%}$ on energy and current of the electron beam, respectively. While the value of $t_{90\%}$ does not depend on the electron beam energy for electron beam energy in 20 to 30 keV range, it shows strong dependence on the electron beam current (spot size) in the 5-140 pA range. Specifically, the value of $t_{90\%}$ decreases from ~275 s to ~50 s with the corresponding current increase from ~5 pA to ~140 pA.

The trends in Figures 3.13a and 3.13b can be explained by the dependence of the time evolution of the deposit diameter on the electron beam settings. As shown in Figure 2.31c, the diameters of deposits formed at the spot size 3 and varied electron beam energies do not differ significantly for corresponding deposition times. In contrast, the diameters of deposits formed at energy of 25 keV and varied spot sizes are much different for the early deposition times. Specifically, the diameter of the deposit formed after 1 minute of deposition at 25 keV and the spot size 2 is much smaller than a corresponding diameter of a deposit formed at 25keV and the spot size 4. However, after 5 minutes of the deposition process, diameters of the deposits formed at those two different settings are similar. Thus, the diameter of deposits formed at lower spot size increases steadily with time, while the diameter of deposits formed at higher spot sizes increase rapidly but then saturates. Accordingly, the resistance of the deposits formed at low electron beam spot size decreases steadily, resulting in a long settling time $t_{90\%.}$ The resistance of deposits formed at high spot sizes decreases rapidly and saturates, resulting in a short settling time $t_{90\%}$.

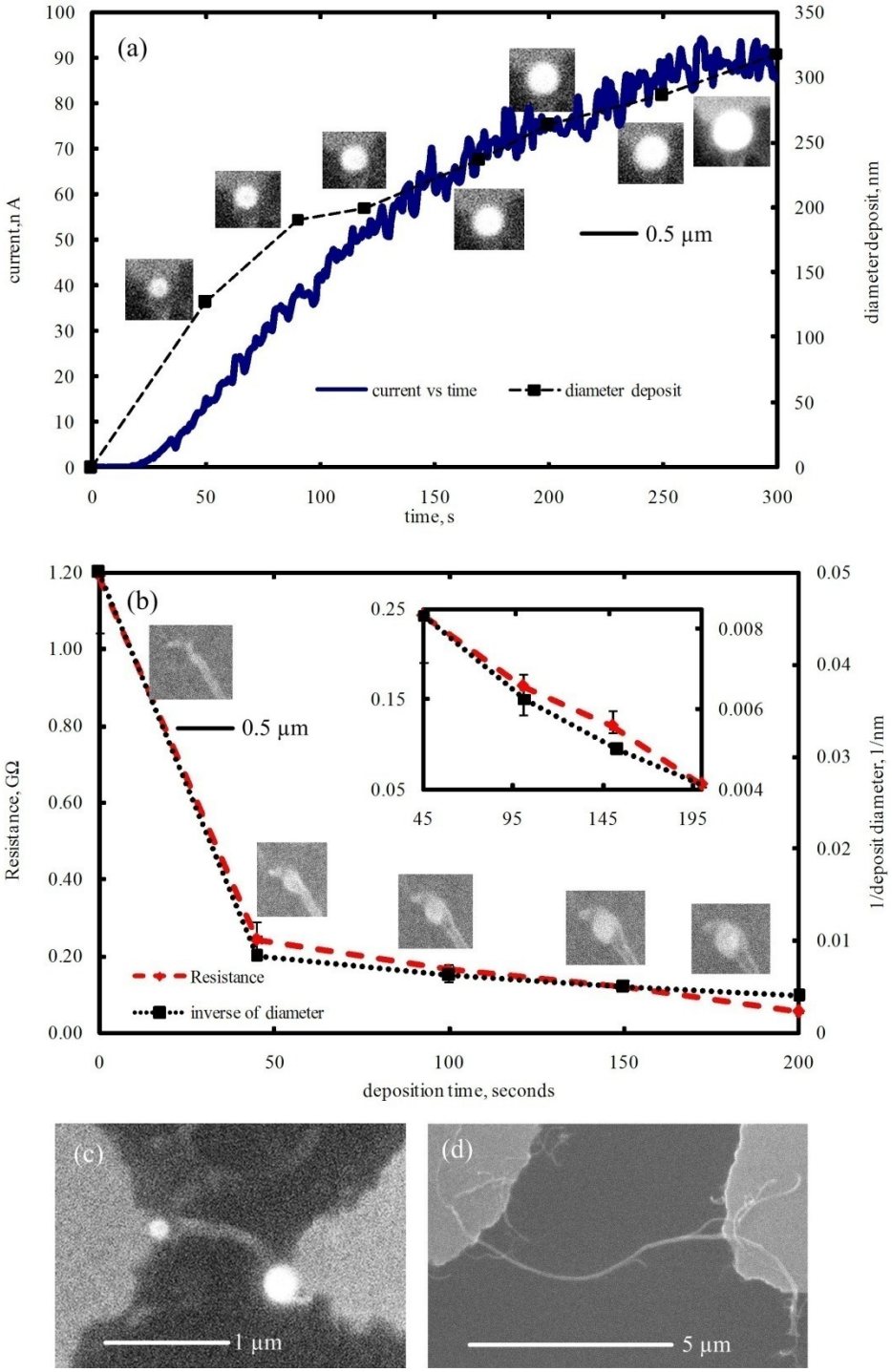

Figure 2.30. (a) In-situ current vs. time measured during deposition on the left end of the interconnect shown in (c). (b) Resistance of the interconnect vs. total deposition time for deposition on the left end of the interconnect shown in (d). The inset shows a detailed view during the later stages of the deposition process (the resistance measurements were taken ~10 minutes after the end of each deposition stage. The SEM images corresponding of the joint at different stages of the deposition are shown in the inset in (a) and (b)).

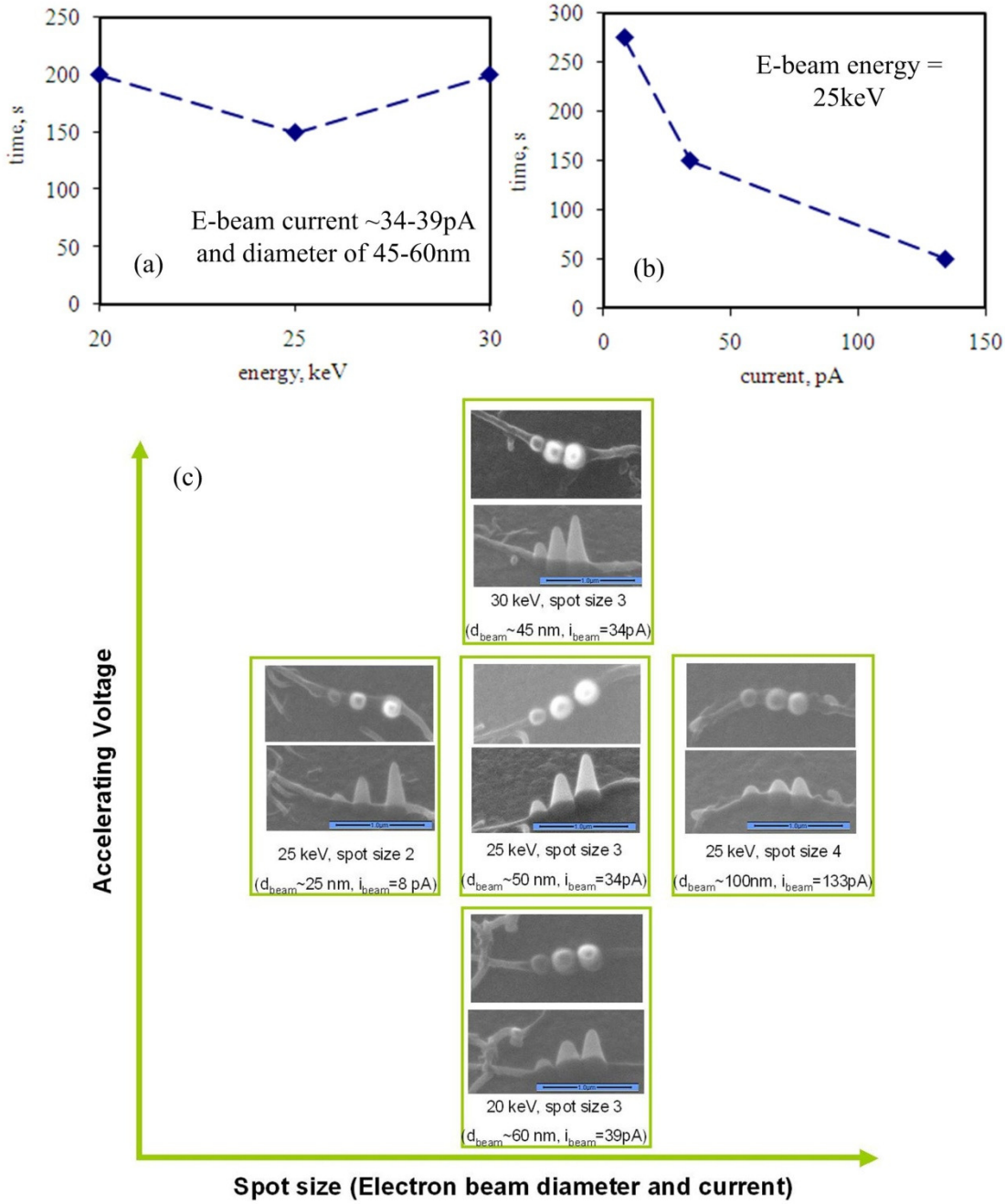

Figure 2.31. The time necessary for the current to reach 90% of its final value during 5 minute deposition experiment in spot mode as a function of (a) electron beam energy and (b) electron beam current (spot size), (c) Top and 45º cone-shape deposits on MWNT formed after 1, 3, and 5 minutes of deposition with settings corresponding to those in (a) and (b).

3.3.3 Multiple square carbon joint deposition experiments

The results obtained in the preceding section demonstrate direct dependence of the contact resistance on the carbon joint geometry. However, the relation between the components contributing to the total resistance of the MWNT interconnect (see Figure 3.1) cannot be inferred from this experiment because the volume of the amorphous carbon joint, the carbon joint-metal and the carbon joint-MWNT interfacial areas increase at the same rate during the deposition process. Thus, a decrease in the total resistance of the MWNT interconnect cannot be attributed to a decrease of any individual component of the total resistance because.

Referring to Figure 3.1, if the joint is assumed to have a circular base area, $R_{spreading}$ can be estimated using an expression derived by Kennedy [111]:

$$R_{spreading} = \frac{\rho_{\text{metal}} H}{\pi a_{\text{joint}}} \qquad 2.20$$

Where ρ_{metal} is the resistivity of the electrode metal, a_{joint} is the diameter of the base area, and H is spreading resistance factor. The spreading resistance factor is a function of the lateral dimension of the base area, (radius a_{joint} if cylindrical shape is assumed), and thickness (h) and a representative length scale ($a_{electrode}$) of the metal electrode. For a_{joint}=10 nm, h=200 nm, and $a_{electrode}$=2500 nm, H ~ 3. If the electrode is made out of copper and has the specified dimensions the spreading resistance equals 0.6 Ω and can be neglected.

The electrical resistance of a circular interfacial films is equal to [112]:

$$R_{\text{interface}} = \frac{\sigma}{\pi a_{\text{joint}}^2} \qquad 2.21$$

Where σ is equal to the product of the layer resistivity and thickness and is assumed to be constant. The bulk electrical resistance of the carbon joint, R_{ac}, depends on the specific geometry of the joint,

$$R_{\text{aC}} \sim \frac{\rho_{aC} l_s}{A_s} \qquad 2.22$$

Where ρ_{aC} is the bulk resistivity of the carbon, l_s and A_s are the representative length and cross section of the joint, with their ratio equal to one over the representative length scale of the deposit, L_{ac}. The electrical resistance of a MWNT depends on the number of defects in the structure of the tube, its length, the number of conducting shells, and their diameter [6]. The resistance of a single shell equals [6]:

$$R_{shell} = \frac{h}{2e^2 N}\left(1 + \frac{L_{MWNT}}{\lambda}\right) \quad 2.23$$

Where $h/2e^2$ is the quantum resistance and equals 12.9 kΩ, and L_{MWNT}, λ, and N are the length of the tube, a mean free path of an electron, and the number of conduction channels in the shell, respectively. The number of conducting channels depends on the tube diameter, D, and for D>3 nm can be approximated as [6]:

$$N_{shell}(D) \approx aD + b \quad 2.24$$

Where a=0.0612 nm^{-1} and b=0.425. The error introduced by the above equation due to different chirality of the tubes is within 15% for all values of D. According to Jiang et al. [113], the electron mean free path in a metallic nanotube equals:

$$\lambda = \frac{D\sqrt{3}\pi\psi^2}{2\sigma_\varepsilon^2 + 9\sigma_\psi^2} \quad 2.25$$

Where ψ is the nearest neighbor tight-binding parameter, ε is the on-site energy, σ_ε and σ_ψ and are the variances of ε and ψ, respectively. Ψ, σ_ε and σ_ψ are approximately constant. According to Li et al. [6], the electron mean free path in a semiconducting nanotube equals:

$$\lambda = \frac{D v_F}{\alpha T} \quad 2.26$$

Where v_F is the Fermi velocity of electrons in carbon nanotubes (~8×10^5 m/s), α is the coefficient of electron scattering rate, and T is the absolute temperature. Irrespective of the nature of the shell, the mean free path depends linearly on the diameter of the tube and can be approximated as $\lambda \cong 1000 \cdot D$ (with D in nm) [6]. Thus, a MWNT with diameter of 100 nm, length ~1 μm, and only the outer shell conducting has a resistance of ~2 kΩ. Conduction through multiple shells significantly lowers the total resistance of the tube.

As made, a typical ~5 μm MWNT interconnect has a total resistance on the order of a few to few hundred MΩ, while MWNT itself has a resistance of a few kΩ. Thus, initially the resistance of the carbon nanotube itself is negligible in comparison to the total resistance of the interconnect. Further, if one assumes the contact resistance of one of the ends to be much smaller than the other (for example if one of

the ends already has a good connection established using EBID), Equation 2.19 reduces to:

$$R_{total} \approx R_{contact} \approx R_{\text{aC-MWNT interface}} + R_{\text{aC}} + R_{\text{aC-metal interface}} \approx \frac{\rho_{aC}}{L_{aC}} + \frac{\sigma_{aC-metal}}{L^2_{aC-metal}} + \frac{\sigma_{aC-MWNT}}{L^2_{aC-MWNT}} \quad 2.27$$

Where $L_{aC-metal}$ and $L_{aC-MWNT}$ are the length scales for the carbon joint-metal and carbon joint-MWNT interfaces, respectively.

The change in MWNT interconnect resistance due to deposition of multiple square amorphous carbon joints in different locations on the MWNT end is investigated to define the dominant resistance in Equation 3.1. Figure 2.32 shows typical in-situ current and resistance measurements and the corresponding top view SEM images of the carbon joints. Each EBID-made carbon square has dimensions of ~300x300 nm and is deposited by scanning the electron beam at energy of 25 keV and current of ~140 pA at a frame time of 0.411s and resolution of 2048x1768 for a period of ~4-5 minutes. In both cases the first square deposit (labeled "1" in Figure 2.32) is made at the end of the MWNT, and the following three square deposits (labeled "2", "3", and "4" in Figure 2.32) are deposited on the electrode without making direct contact to the MWNT. The fifth square deposit (labeled "5" in Figure 2.32) is deposited on the part of the MWNT resting on top of the insulator ($Si0_2$) layer. The continuity of the deposit sequence is assured by a slight overlap of adjacent squares. The in-situ measured current increases only during the deposition of the first and second squares (Figure 2.32 a), resulting in a respective resistance decrease in Figure 2.32b. A further increase in the deposit size or contact area to the electrode or MWNT does not decrease the total resistance of the MWNT interconnect. Additionally, the geometrical arrangement of the individual square deposits does not impact the results. As shown in Figure 2.33, the squares are grown in a straight line and to both sides of the MWNT. Making the second, third, and fourth deposits increases only L_{aC} and $L^2_{aC-metal}$ (these two terms increase at the same rate since a thin carbon square is deposited). During the deposition of the fifth square only the contact area of the amorphous carbon-to-MWNT interfacial film increases $\left(\sim L^2_{aC-MWNT}\right)$. Since the resistance does not change during the deposition of the fifth square, the area of the initial contact $\left(\sim L^2_{aC-MWNT}\right)$ resulting from the deposition of the first square is sufficient to decrease $R_{\text{aC-MWNT interface}}$ significantly below the value of the sum of R_{aC} and $R_{\text{aC-metal interface}}$. A decrease of the resistance during

deposition of the second square is due to further decrease in the values of R_{aC} and $R_{\text{aC-metal interface}}$. The saturation of the resistance during deposition of the third and fourth squares demonstrates that the resistance could not be decreased by further increase in L_{aC} and $L^2_{aC-metal}$.

In summary, these results show that for EBID-made carbon joints $R_{\text{aC-MWNT interface}} \ll (R_{\text{aC}} + R_{\text{aC-metal interface}})$ and a much smaller contact area between the amorphous carbon deposit and the MWNT is required, as compared to that between the amorphous carbon deposit and the metal electrode, to establish an effective Ohmic contact.

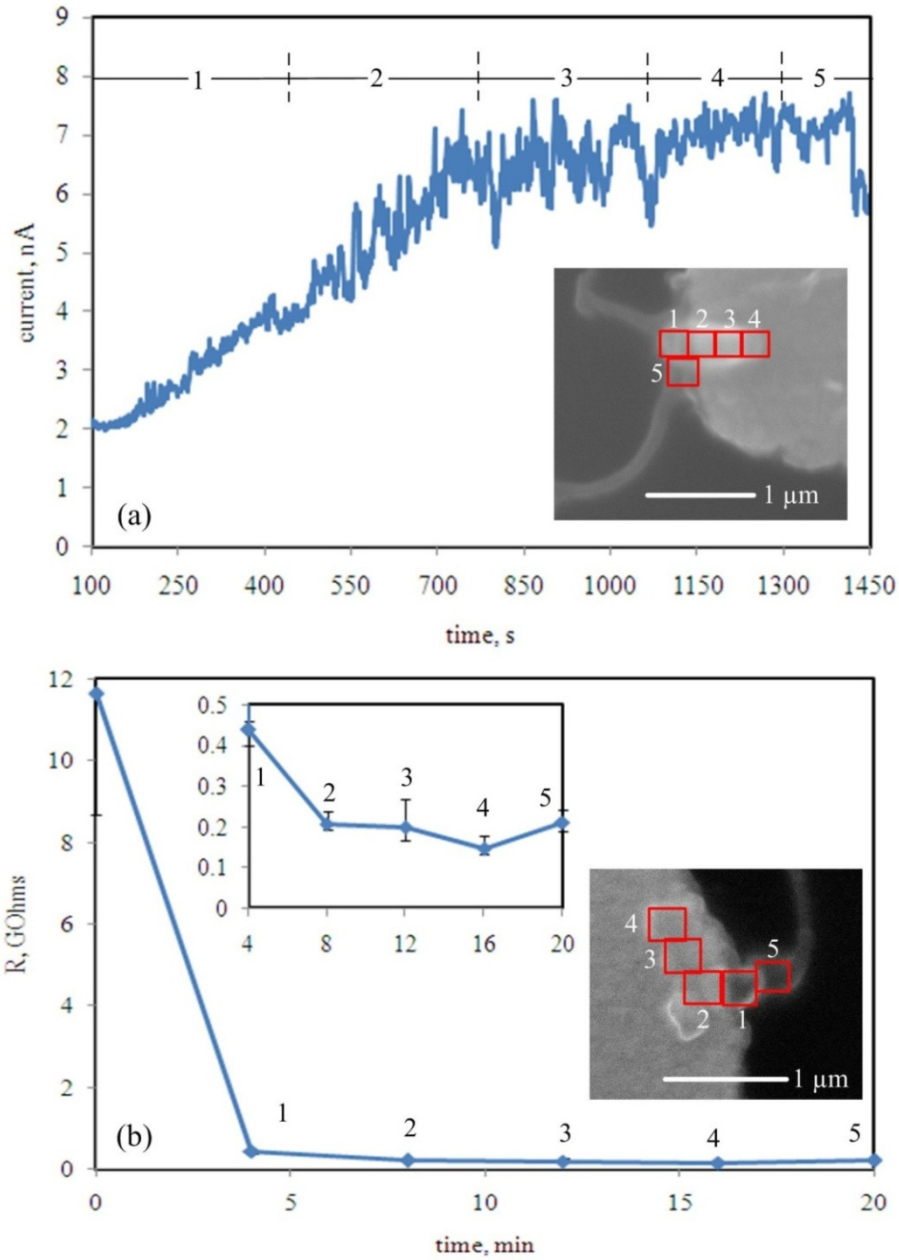

Figure 2.32. (a) In-situ current vs. time measured during deposition for the MWNT end shown in the inset (b) Total resistance of interconnect vs. total deposition time for deposition the MWNT end shown in the inset. The inset on the left shows a detail view of resistance change during the later stages of the deposition process (all resistance measurements are taken ~10 minutes after the end of each deposition stage).

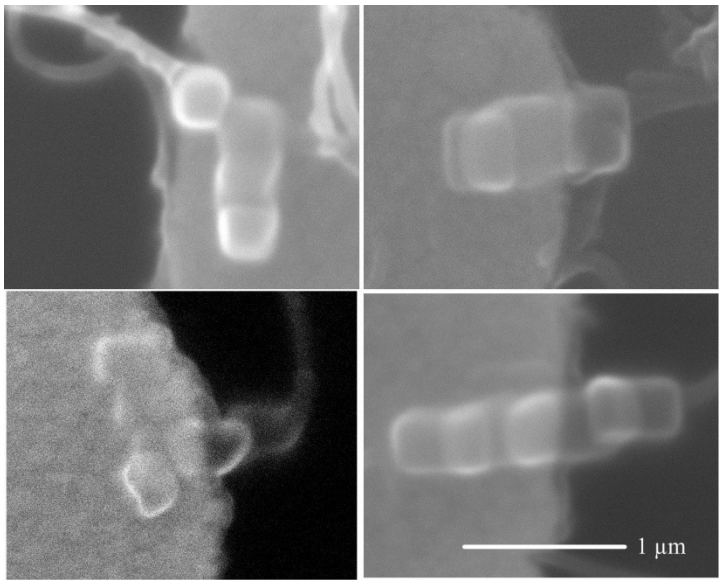

Figure 2.33. Different arrangements of the amorphous carbon connection comprising of multiple deposited squares.

3.3.4 Joule-heating-induced partial graphitization of the carbon connection

A typical current vs. voltage curve for a Joule-heating-induced graphitization of a MWNT interconnect with EBID-made amorphous carbon joint is shown in Figure 2.34. A drastic increase in the current is observed when the voltage is increased to 2.5 V. Exact measurement of the post-graphitization resistance is difficult because MWNT tend to burn out during the phase transition of the carbon joint. The inset in Figure 2.34 shows the MWNT interconnect from Figure 2.30 after it broke during graphitization.

The change in the resistivity of the amorphous carbon deposit due to Joule heating is investigated. Amorphous carbon film is grown between two electrodes and partially graphitized in the same manner as the MWNT interconnects. The before and after graphitization current vs. voltage curves and the corresponding SEM image of EBID carbon film are shown in Figure 3.17. Before-graphitization and after-graphitization resistances of the film are estimated from the linear part of the current vs. voltage data. The film resistance decreases from ~2 MΩ to ~0.05 MΩ, which corresponds to a resistivity decrease from $2x10^5$ Ωμm to $5x10^3$ Ωμm. It should be noted that the resistivity of the partially graphitized film is still ~1-2 orders of magnitude higher than that of graphite [114].

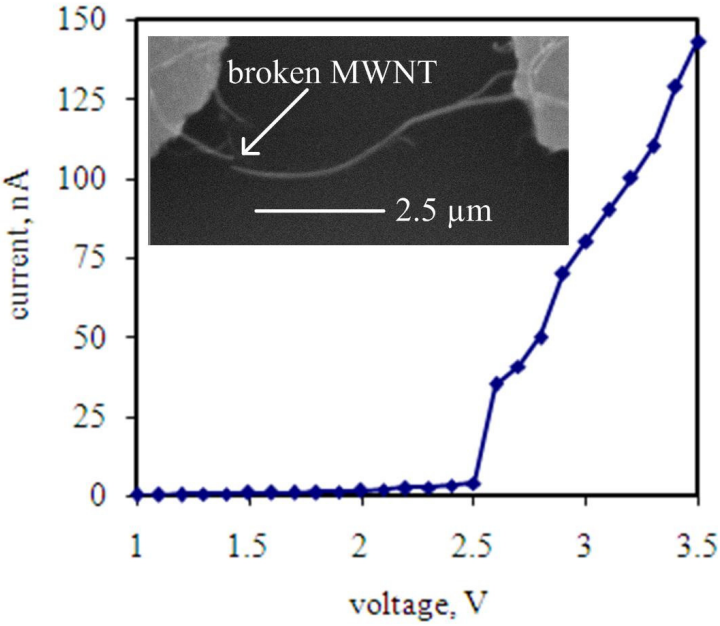

Figure 2.34. Typical current vs. voltage curve for a Joule-heating-induced partial graphitization. Inset shows the MWNT after it broke during the Joule heating experiment.

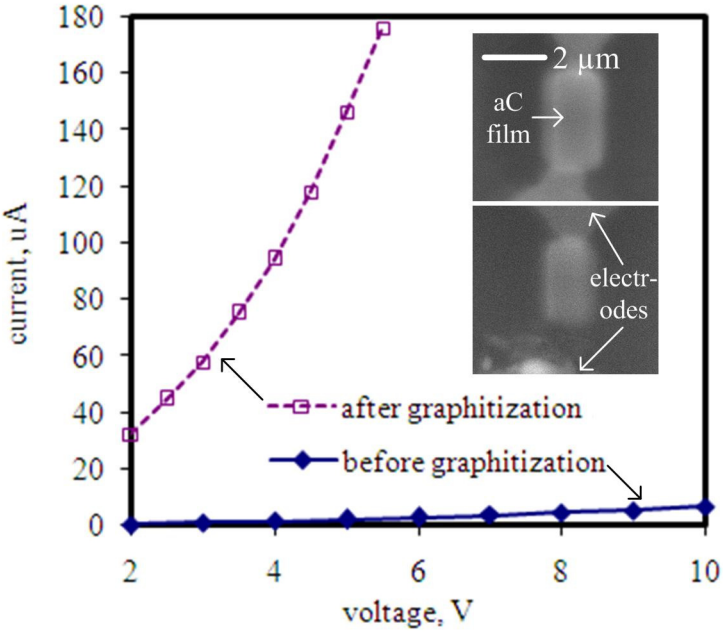

Figure 2.35. Before and after partial graphitization current vs. voltage curves for carbon film grown using EBID of residual hydrocarbons. Insets show the film before graphitization and after it broke due to high current passage.

The initial resistivity of the EBID carbon highly depends on the nature of residual hydrocarbons used as a

precursor and reported values vary significantly [115]. Full graphitization of the film is difficult to achieve because of the severe degradation of the film with an increased Joule heating (see lower inset in Figure 3.17).

The temperature rise due to Joule heating of the EBID-enabled MWNT interconnect is estimated using a Finite Element Method electro-thermal simulation. Since the dependence of resistivity and thermal conductivity of amorphous carbon on the annealing temperature is unknown, material properties corresponding to those of unannealed and partially graphitized carbon deposit are simulated. For a MWNT with diameter of 30 nm and length of 10μm with hemispherical carbon joints with diameter of 100 nm, the temperature rise due to a voltage difference of 1-5 V was estimated to be 125-2450ºC and 75-1300ºC for the unannealed and partially graphitized carbon joints, respectively. This result confirms that the decreases in interconnect resistivity is due to significant Joule heating of the MWNT-electrode carbon joint. Details of the thermal analysis are presented in Appendix E.

3.4 EBID carbon composition experiments

To further understand the phase composition of the EBID-made carbon joints is investigated using Raman spectroscopy. Raman spectroscopy is a powerful analytical technique for probing the physical and chemical properties of various carbon nanostructures such as carbon nanotubes, graphene, and electron beam deposits. Diameter and the electronic state (metallic vs. semiconducting) dependence of radial breathing mode, strain sensitivity of graphitic band (G Band) and the second harmonic of disorder band (G' band) are exploited to characterize carbon materials [96, 116-119]. Of particular significance for the present study is the ratio of the areas under the disorder band (D band) and the graphitic band (D/G ratio), which quantifies the size of the degree of graphitization (size of microcrystalline regions and the phase composition (amorphous vs. crystalline)[120-122]. Specifically, the influence of annealing at different temperatures on the EBID-made carbon is analyzed. Figure 3.18 g-h shows the Raman micromapping of carbon square acquired by integrating intensity from 1500cm^{-1} to 1700 cm^{-1} and the corresponding SEM image.

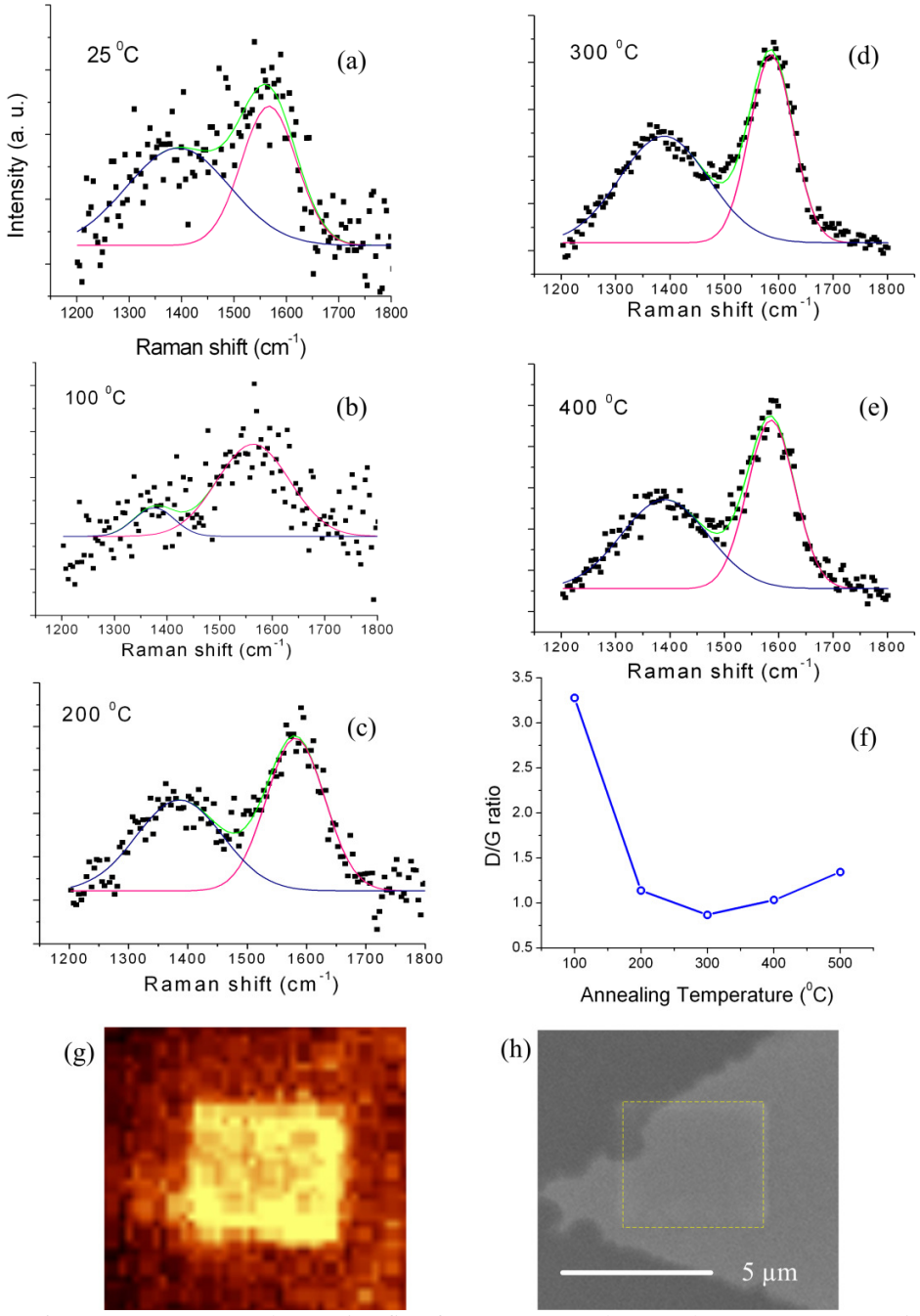

Figure 2.36. Raman spectra (and Gaussian fits) for EBID amorphous carbon squares at (a) 25ºC, and annealed at (b) 100 ºC , (c) 200 ºC , (d) 300ºC, (e) 400ºC (the spectrum is deconvoluted into overlapping D and G band spectra), (f) Ratio of areas under the D and G bands as a function of temperature. (b) Ratio of the areas under the D and G bands as a function of temperature, (g) Confocal Raman map of an EBID-made carbon square acquired by integrating the area under the spectra from 1500cm^{-1} to 1700 cm^{-1}, and (h) Corresponding SEM image. (Raman measurements were performed by Dhaval Kulkarni and Srikanth Singamaneni from Professor Tsukruk's group at Georgia Institute of Technology).

The Raman spectra (and the Gaussian fits) for carbon square annealed in air for 3 minutes at 100ºC, 200ºC,

300ºc, and 400ºC, the area ratio for D and G bands are shown in Figure 3.18 b-f. One can clearly distinguish the characteristic G band (1580 cm^{-1}) and D band (1350 cm^{-1}).

Two distinct trends associated with amorphous carbon graphitization can be deduced from these data. First the D/G band ratio decreases significantly with an increase of the film annealing temperature from 100ºC to 200ºC. Second the full width at half maximum (FWHM) of the G band decreases from 125.9 cm^{-1} to 80.4 cm^{-1} with concomitant increase in the intensity of the peak. Finally, the G band peak position shifted from 1562 cm^{-1} to 1586 cm^{-1} as the carbon was annealed at elevated temperatures. The decrease of the D/G band ratio and the narrowing of the G band and the shift of the G band to higher wavenumbers clearly suggest the conversion of sp^3 bonds to sp^2 bonds, removal of hydrogen, and conversion of amorphous carbon to crystalline graphite materials, all significantly affecting contact resistance discussed above [123].

3.5 Concluding remarks

The influence of EBID-made carbon joint geometry and properties on the total resistance of MWNT interconnects is investigated. Procedure for fabrication of the MWNT interconnects is developed and described. MWNT with diameters of 50-150 are purchased from a commercial vendor [124], purified by refluxing in nitric acid for 48h, and dispersed by ultrasonication in Dimethylformamide (DMF). Individual MWNT are aligned between two metal electrodes on a Si chip using dielectrophoresis. Three methods for MWNT end opening are tested. Annealing of the MWNT powder, water assisted electron beam etching of the tube, and Focused Ion Beam cutting are attempted, but do not yield a clean cut of MWNT without destroying the tube or the electrodes. Thus, EBID-made carbon joints are investigated aiming at establishing contact only to the outer shell of the MWNT.

EBID carbon joints are fabricated using Quanta 200 ESEM with residual hydrocarbons as a precursor. The influence of the EBID-made carbon deposit on the electrical resistance of the MWNT interconnects is measured in two ways. First, the current resulting from a DC bias imposed on the metal electrodes bridged by MWNT is measured in-situ during the deposition process. Second, the deposition process is performed in several steps, and current vs. voltage data sets are collected ~10 minutes after the end of each deposition

stage. It is found that the electron beam can influence the measured current through an interconnect in a direct and an indirect way. The direct contribution of the injected primary electrons to the measured current is found negligible. However, the secondary electrons generated in inelastic collisions of the primary electrons are numerous and significantly alter the measured current. Specifically, turning on the electron beam significantly increases the measured current, while turning the beam off causes an exponential decay of the measured current. This behavior is consistent with an interpretation that the EBID-deposited material acts as a capacitor for the electron beam generated electrons. The capacitive element is charged during electron injection and slowly discharges when the beam is turned off. As a result, the in-situ current measurements during the deposition are intrinsically transient in nature, and to obtain steady DC current vs. voltage characteristics measurements have to be performed ~10 minutes after an end of the deposition process as the system achieves a steady state.

EBID-made cone-shape carbon joints in the 20-30 keV energy range and ~5-140 pA current range with a deposition time of 5 minutes are fabricated. The in-situ measured current is found to vary directly with the cone base diameter. This trend is quantitatively confirmed when the total resistance of the MWNT interconnect is found to change proportionally to the inverse of the deposit diameter. Since the material composition and interfacial film properties do not change during deposition experiments, only geometrical factors contribute to the lowering of the interconnect resistance. These results thus demonstrate the direct dependence of the contact resistance on the carbon joints geometry. The relation between the components contributing to the total resistance of the MWNT interconnect cannot be inferred from such global experiment because all the relevant geometric scales $\left(L_{aC},\, L^2_{aC-metal},\, L^2_{aC-MWNT}\right)$ increase at the same rate.

In order to individually vary the geometric characteristics of deposited carbon joints, deposition of multiple square EBID-made carbon joints is performed. The EBID square carbon joints with dimensions of ~300x300 nm are deposited by scanning the electron beam at energy of 25 keV and current of ~140 pA for a period of ~4-5 minutes. Deposition of the first EBID square is analogous to the cone-shaped experiments: all relevant geometric scales increased at the same rate. However, by varying the location of the successive EBID-made squares, contact is selectively established only to the electrode or to the

MWNT. Comparison of the changes in the resistance of the interconnect with the corresponding changes in the relevant geometric scales of the deposit demonstrates that for EBID-made carbon joints $R_{\text{aC-MWNT interface}} \ll R_{\text{aC}} + R_{\text{aC-metal interface}}$ and that a much smaller contact area between the carbon joint and MWNT is necessary as compared to that between the carbon joint and metal electrode.

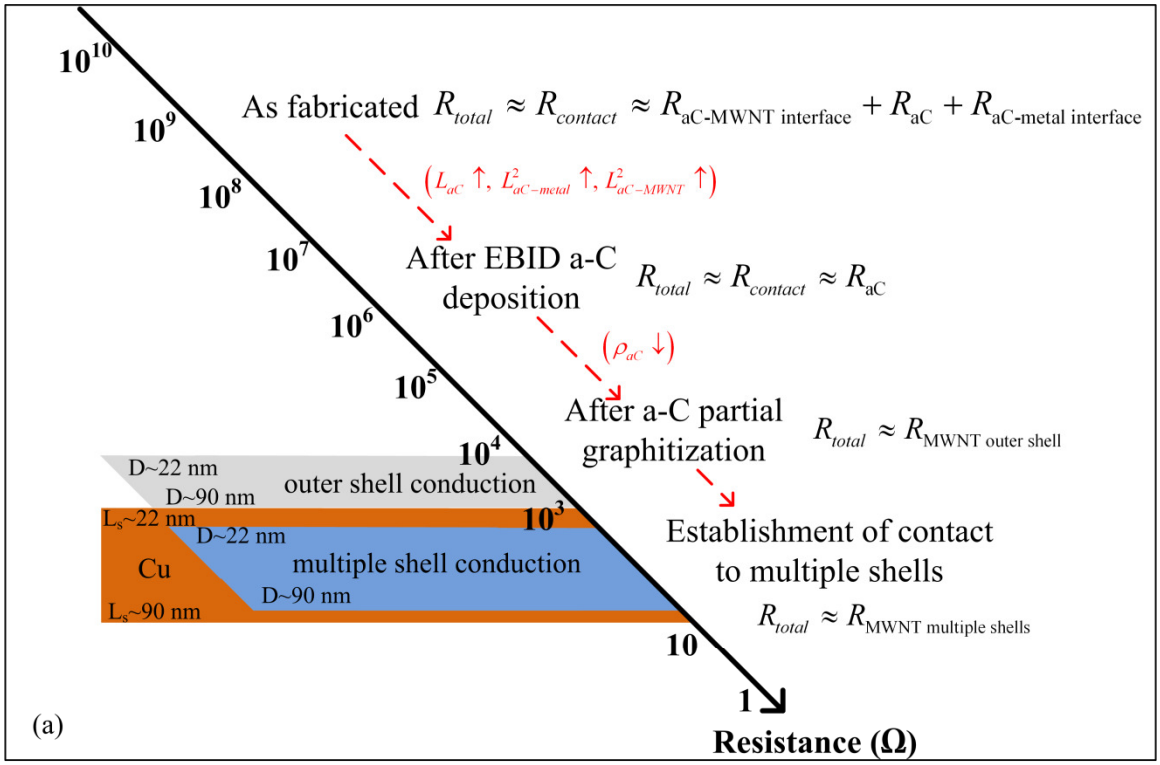

Figure 2.37. (a) Chart summarizing dominating factors in resistance of EBID-enabled MWNT interconnects. (MWNT resistance values assume a 5 µm length of the tube), and (b) Comparison of theoretical resistivity of MWNT and copper interconnects[125].

Lastly, the deposited amorphous carbon joints are partially graphitized by increasing the DC voltage across the interconnect. The resistance of the interconnect decreases significantly due to the Joule heating caused by passage of a large electric current. To confirm the impact of Joule heating on the resistivity of deposited carbon, the voltage across EBID-made carbon line connecting two electrodes is varied in same manner. It is shown that the resistivity of EBID carbon line decreases from $2x10^5$ Ωμm to $5x10^3$ Ωμm during the Joule heating line experiments. Resistance measurement of the fully graphitized EBID carbon joints and lines are not possible due to mechanical failure of the MWNT and carbon lines. The partial graphitization of EBID amorphous carbon due to annealing is confirmed using Raman spectroscopy. Under the assumption that Joule heating does not affect the electrical resistivity of the amorphous carbon-metal electrode interface $(\sigma_{aC-metal})$, only the resistivity of the amorphous carbon (ρ_{aC}) changes due to Joule heating. Since the total resistance of the interconnect changes only when the bulk carbon resistivity, ρ_{aC}, is varied, $R_{\text{aC}} \gg R_{\text{aC-metal interface}}$.

In summary, the resistance of the carbon joint itself seems to be the dominating factor contributing to the total resistance of the MWNT interconnect. As fabricated, the total resistance is limited by the sum of the metal electrode-carbon joint interfacial resistance, carbon joint resistance, and the MWNT-carbon joint interfacial resistance. After deposition of a sufficiently large EBID amorphous carbon joint, when increases in $L^2_{aC-MWNT}$ L_{aC}, $L^2_{aC-MWNT}$, and $L^2_{aC-metal}$ no longer decrease the resistance, the total resistance is limited by the joint material resistance. Partial graphitization lowers the resistivity of the deposited amorphous carbon by two orders of magnitude. As shown in Figure 2.37a, after partial graphitization of the interface the total resistance of the MWNT interconnect is no longer limited by the contact resistance, but by the resistance of the outer shell of the MWNT. Further decrease in the total resistance of the MWNT interconnect can only be achieved through establishing an electrical contact to the inner shells of the MWNT. As shown in Figure 3.19b, MWNT interconnects have comparable or lower resistivity than copper interconnects only if contact to all shells is established.

CHAPTER 4

GROWTH DYNAMICS OF EBID OF RESIDUAL HYDROCARBONS IN THE PRESENCE OF MWNT

4.1 Introduction

In Chapter 2 a model of EBID of residual hydrocarbons on flat substrate is developed. Three distinct growth regimes are identified using scaling analysis and verified using simulations. It is demonstrated that the model developed can successfully capture the complex growth dynamics of pillar within ring deposits. The significant impact of the EBID carbon joint geometry on the electrical properties of the MWNT interconnect is demonstrated in Chapter 3. The relative importance of geometrical parameters such as the EBID carbon-MWNT and EBID carbon-metal electrode contact areas is established. In this Chapter the influence of a MWNT on the growth dynamics of the EBID process is investigated experimentally and theoretically using tools described in Chapters 2 and 3.

Presence of MWNT can impact four processes contributing to the EBID growth dynamics: (1) the surface mass transport and concentration of the precursor material, (2) the electron induced dissociation and ionization reaction of the precursor, (3) the primary electron transport and secondary electron generation, and (4) the secondary electron transport and emergence from the surface. Since adsorbed phase electron induced dissociation and ionization cross sections for most precursor gases are not available and gas-phase equivalents are used instead, it is assumed that the electron induced reaction on the surface of the silicon and MWNT follows the same mechanism as described in Chapter 2. According to Joy [41], the high energy primary electron elastic and inelastic scattering models are functions of electron energy, atomic number, atomic weight, and density of the scattering medium only. Since the atomic number, atomic weight, and the density is the same for graphite and MWNT, primary electron scattering and secondary electron generation within the MWNT can be approximately treated as scattering within a solid graphite cylinder of the same size. There is lack of fundamental experimental and theoretical knowledge about the transport of low energy secondary electrons within the MWNT. One thing that can be noted is that conduction electron transport within the MWNT is highly anisotropic, and so could be the low energy

secondary electron transport. The simulations coupled to EBID experiments allow one to investigate such a possibility.

While secondary electron emission from single wall carbon nanotubes (SWNT) [126, 127] and from carbon nanofibers (CNF) [128-130] has been explored, low energy secondary electron transport within MWNT has not been addressed. For low energy secondary electron transport, a possibility of isotropic and anisotropic scattering must be taken into account. We investigate this possilibity by simulating two scenarios. In the first case, it is assumed that scattering within a MWNT does not differ from scattering within a solid carbon fiber and is isotropic in all directions. In the second case, the increased probability of secondary electrons having a preferential scattering direction along the tube's axis is included in simulations using the mean free path of electrons (see Figure 2.38).

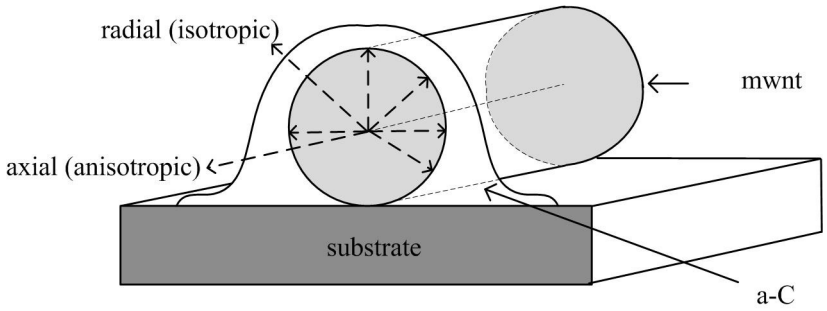

Figure 2.38. Schematic of secondary electron scattering directions within the MWNT.

In both cases, the inelastic mean free path of the secondary electrons is calculated using the Seah and Dench's formula [131]. However, in the second case, it is assumed that the secondary electron inelastic mean free path in the axial direction, λ_{axial}, was greater than the inelastic mean free path in the radial direction, λ_{radial}, with a multiplier K ($\lambda_{axial} = \lambda_{radial}K$) being a parameter varied in simulations. For secondary electrons with trajectories not along either the axial or the radial directions of the tube, the effective inelastic mean free path is calculated by taking the square root of the sum of the squares of the anisotropic inelastic mean free paths multiplied by the corresponding directional cosines [132].

First the influence of MWNT secondary electron scattering properties on the EBID process is investigated. The secondary electron yield for free standing MWNT is measured and compared to Monte

Carlo simulations of secondary electron yields with different SE scattering properties. The carbon pillar growth dynamics on MWNT resting on a silicon substrate is explored and compared to the carbon pillar deposition on geometrically similar amorphous carbon lines. Simulations of the growth process for the isotropic and anisotropic secondary electron scattering modes are used to explain the experimental results. Lastly, the EBID carbon growth on the edge of the tube are simulated and related to experimental results from Chapter 3.

4.2 Secondary electron yield estimation

Electron beam current impinging on a substrate can be accurately measured by grounding the stage of the SEM and measuring the resulting current using a picoammeter. According to Bret et al. [108] the measured current is proportional to number of primary electrons minus the number of backscattered electrons plus the number of emitted secondary electrons ($i_{total}=i_{PE}-i_{BSE}+i_{SE}$). The number of backscattered and secondary electrons depends on the energy of the electron beam and geometry of the substrate. When the substrate is thin most of the primary electrons penetrate all the way through the substrate. In other words, the current measured during impingement of an electron beam on a small target, such as a free standing MWNT or edge of a silicon wafer, is primarily due to the secondary electrons. In this section, the current resulting from electron beam impingement on a free standing MWNT is measured and computed to estimate the secondary electron yield from the tube. In order to quantify the accuracy of this method, measurements and predictions of the current resulting from electron beam impingement on an edge of a silicon wafer are compared against each other.

4.2.1 Secondary electron current measurement from silicon edge

In order to verify this method of measuring the secondary electron current, the current resulting from electron beam impingement at 45º a varied distances away from an edge of a silicon wafer was measured and simulated. Experiment and simulation results for electron beam energy of 15 keV and 25 keV are compared in Figure 2.39a and Figure 2.39b.

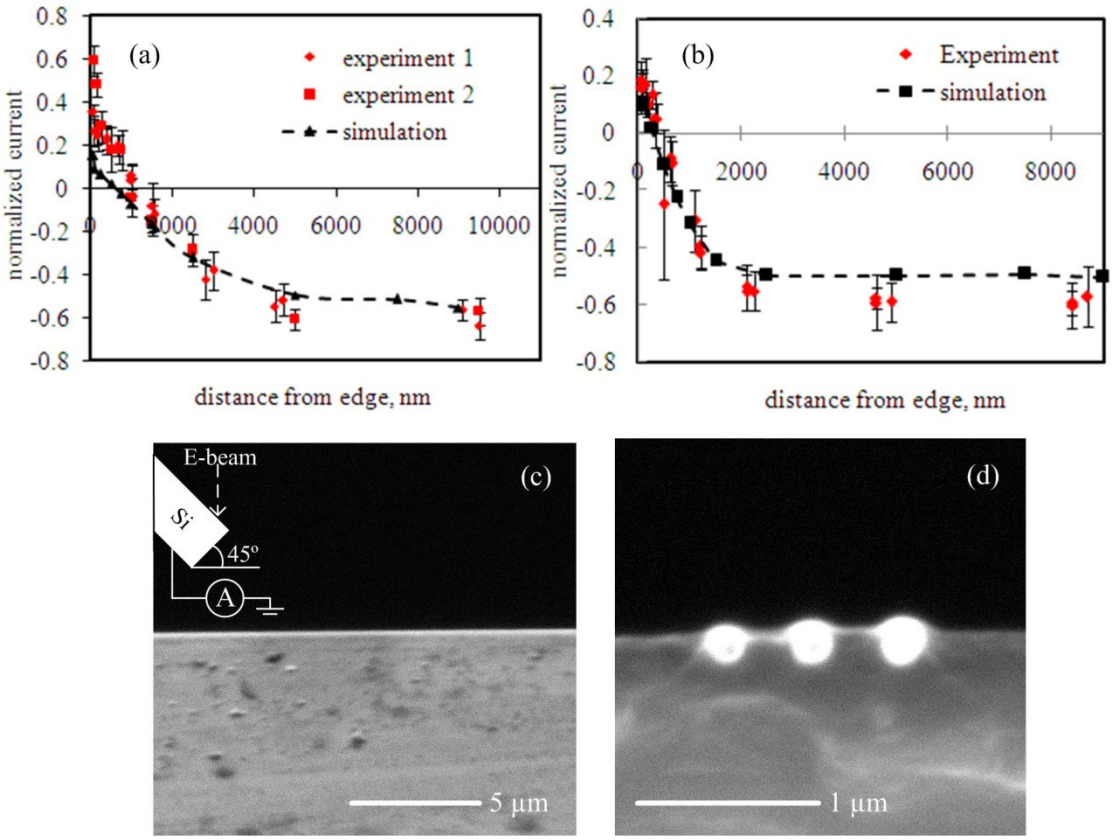

Figure 2.39. Normalized experimental and simulated current resulting from impingement of primary electron beam with energy of (a) 25 keV and (b) 15 keV at 45º angle at a Si wafer edge, (c) SEM image of the Si edge (the inset shows a schematic of the experiment), and (d) carbon deposit resulting from 10, 20, and 30 seconds of exposure of the edge of the Si wafer to an electron beam at 25 keV.

The simulations correctly predict that near the edge of the silicon wafer current increases from its baseline negative value to zero and eventually becomes positive. The switch in the sign of the current is due to a decreased contribution of primary electrons (negative charge) and an increased contribution of the holes (positive charge) produced during generation of secondary electrons, which leave the substrate. The experimental results within ~50-250 nm of the silicon wafer edge are difficult to quantitatively compare to simulations due to imperfections in the structure of the edge (not perfect 90º cut) and a quick build-up of contamination deposit (see Figure 2.39d). While the structural imperfections should not be an issue in free standing MWNT experiments, the build-up of amorphous carbon could alter the results and complicate interpretation of the experimental data.

4.2.2 Secondary Electron current measurement from Free Standing MWNT

Secondary electron current resulting from electron beam impingement at 45º angle on free standing MWNT with diameter in the 30 to 80 nm range is measured. MWNT film with thickness of ~40 µm grown using Chemical Vapor Deposition (CVD) on iron catalyst at ~700ºC [133] is used as a measurement sample.

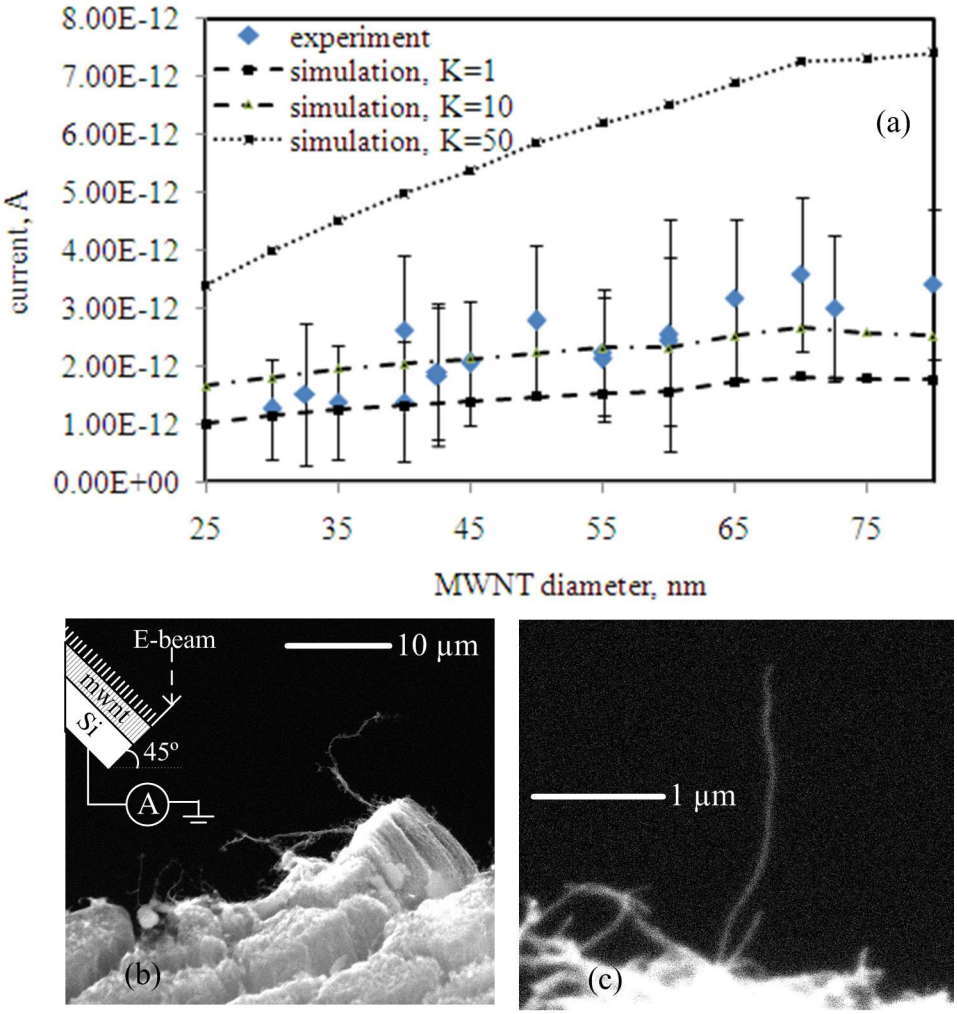

Figure 2.40. Experimental and simulated current resulting from impingement of the primary electron beam with energy of 25 keV, diameter of 50 nm, and current of ~34 pA at 45º angle for MWNT with varied diameters (b) SEM image of the MWNT forest edge (the inset shows a schematic of the experiment), and (c) close up of an individual freestanding MWNT.

SEM images of the edge of the MWNT film and an individual MWNT are shown in Figure 2.40b (see inset for schematic of experiment configuration) and Figure 2.40c, respectively. The stage current is recorded

for 10 seconds while the electron beam is focused on the center of individual MWNT. The experimental and simulation results for varied degree of anisotropy of secondary electron scattering within the MWNT (mean free path ratio of K=1, 10, and 50) are presented in Figure 2.40a. While the values of the experimental and simulated currents for K=1 and K=10 are similar, quantitative comparison of trends is difficult due to a scatter in the measured data. Specifically, the current measured for a free standing MWNT with diameters of 30-80 nm is on the same order of magnitude as the simulated current for K=1 and K=10. The significant noise in the measured data is caused by intrinsic vibration of the SEM stage, electron beam drift, and carbon deposition from always present contamination. Estimation of the actual secondary electron yield is also complicated by the fact that not all primary electrons impinge on the MWNT (since diameter of the beam is comparable to the size of the tubes). Based on the simulation results, the true secondary electron yield (number of secondary electrons emitted per primary electron impinging on the MWNT) for the experimental results is somewhere between ~0.05 and 0.1. At the same time, the secondary electron yield for the K=100 case should be in the ~0.2 to 0.25 range as predicted by simulations. This value is slightly higher than the ~0.04 secondary electron yield for electron beam at 25 keV impinging on flat carbon substrate.

4.3 EBID carbon pillar growth

EBID carbon pillar growth on top of capped and open-ended MWNT and amorphous carbon lines of similar dimensions is investigated. Pillars are deposited by keeping the electron beam stationary for a varied period of time. To assure similar deposition conditions, the electron beam is blanked for one minute between each deposition experiment.

4.3.1 EBID pillar growth on capped MWNT resting on silicon substrate

EBID pillar are deposited on MWNT with diameters of ~50-150 nm resting on silicon substrate. Figure 2.41 shows typical deposits grown for a period of 1, 3, and 5 minutes with an electron beam energy of 25 keV, diameter of 50 nm, and current of 34 pA on top of MWNTs with diameters of 80, 90, and 130 nm (see Figure 2.31c for more examples).

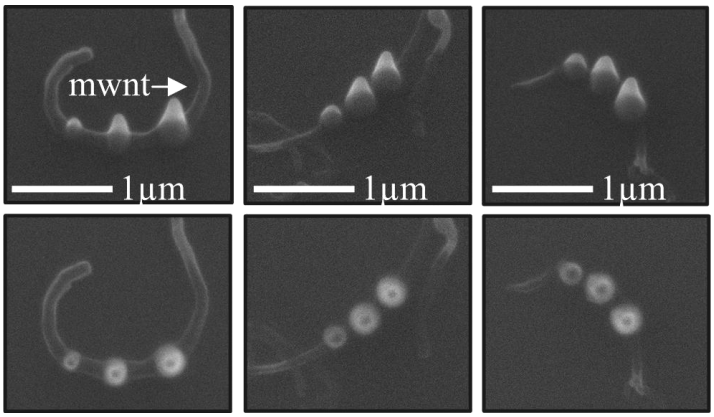

Figure 2.41. Tilted at 30º and top view SEM images of EBID carbon pillars grown for a period of 1, 3, and 5 minutes on a MWNT with diameter of (a) 130nm, (b) 90nm, and (c) 80nm [132].

4.3.2 EBID pillar growth on a FIB-cut MWNT resting on silicon substrate

To ensure that the capped ends of the MWNT do not impact the deposition process, EBID pillars are grown on top of MWNT with FIB-cut ends. In order to open up the ends of the MWNT, the FIB is scanned in a rectangular region at the end of the MWNT. The FIB cutting is performed using FEI Nova Dual Beam FESEM with Gallium ions beam with energy of 30 keV and current of 23 pA. Figure 2.43 shows FIB cuts and subsequent EBID pillar deposits grown for 5 minutes with electron beam energy of 25 keV, diameter of 50 nm, and current of 34 pA on varied locations of a MWNT with diameter of ~100 nm. As shown in Figure 2.42 the deposit location on the MWNT as well as the opening of the tube's ends do not affect the shape of the deposits.

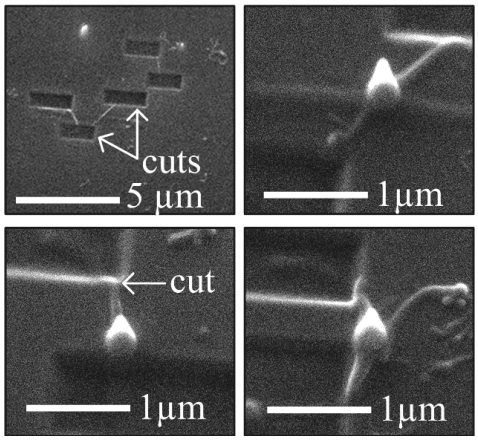

Figure 2.42. Tilted at 30º SEM images of EBID carbon pillars grown for a period of 5 minutes on FIB-cut MWNT with diameter of ~100 nm.

4.3.3 EBID pillar growth on amorphous carbon lines

The 4 μm long amorphous carbon lines are grown by scanning the electron beam in line mode at a frame time of 3.7 s for a period of 2.5, 5, 7.5, and 10 minutes. To assure similar deposition conditions, the electron beam is blanked for one minute between each deposition experiment. The SEM images of pillars grown on four lines and on the silicon substrate are shown in Figure 2.43.

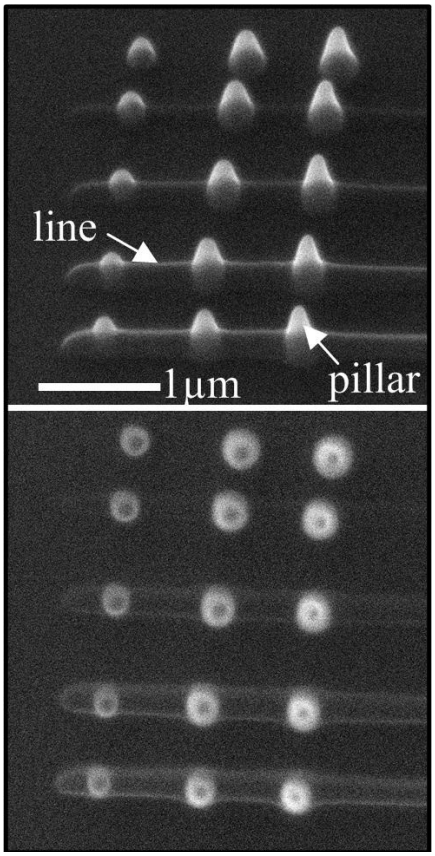

Figure 2.43. 30º and top view SEM images of EBID pillars grown for a period of 1, 3, and 5 minutes on amorphous carbon lines grown for 2.5, 5, 7.5, and 10 minutes and on bare silicon substrate (top set of deposits) [132].

Comparing Figure 2.41 and Figure 2.43 shows that the pillar deposits grown on a MWNT match the pillar deposits grown on EBID-deposited amorphous carbon lines for all three deposition times.

4.4 Simulation of EBID pillar growth on MWNT

In order to explain the experimental results, EBID pillar growth on MWNT is simulated. In simulations, the surface diffusion coefficient and the initial surface concentration of adsorbed residual

hydrocarbons are set to 10^6 nm^2/s and 0.25 $\mu g/cm^2$, respectively, corresponding to the mixed deposition regime [41, 134]. The electron beam conditions corresponding to those used in the experiments (the accelerating voltage of 25 kV, the electron beam current of 35 pA, and a full-width at half-maximum (FWHM) beam diameter of 50 nm) are used. The early growth stages of the deposit are simulated for a total deposition time of 5 ms for a representative case of a MWNT with diameter of 50 nm (see Figure 2.44). The reactive electron flux term is updated every 0.5 ms based on simulation of 50,000 primary electrons.

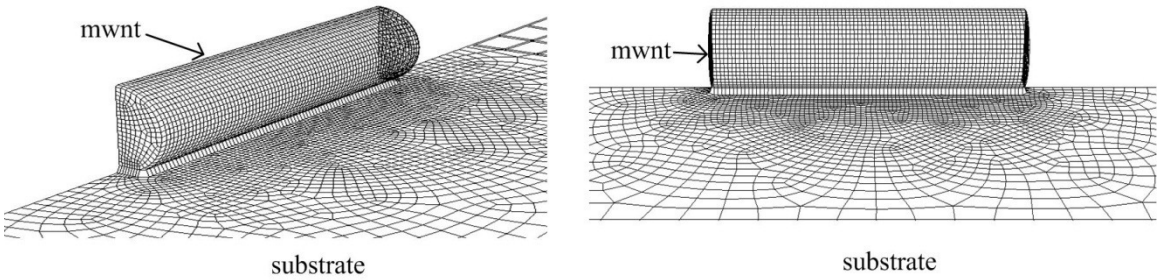

Figure 2.44. Schematic of the MWNT and the substrate geometry mesh with quad elements with lengths scale of ~2 nm used in simulations [132].

Figure 2.45 shows the simulation results at two different time instants for the two cases (isotropic vs. anisotropic scattering) as previously described. While the spatial distribution of reactive electron flux and surface concentration of the adsorbed species for the two simulated cases differ significantly, the resulting instantaneous growth rates for isotropic and anisotropic scattering cases are comparable after the initial (~1ms) deposition period. The final shape of the deposits at the end of the early growth stage (a-b), resulting from time integration of the instantaneous growth rates, is also similar for the simulated cases of isotropic and anisotropic secondary electron scattering. In both simulated cases, the maximal thickness of the deposited amorphous carbon layer is about 4 nm.

Since the cutoff energy for the dissociation reaction is about 7 keV [39], only secondary electrons substantially contribute to the deposition process. Figure 2.46c shows the secondary electrons yield as a function of time for the isotropic and anisotropic secondary electron scattering cases.

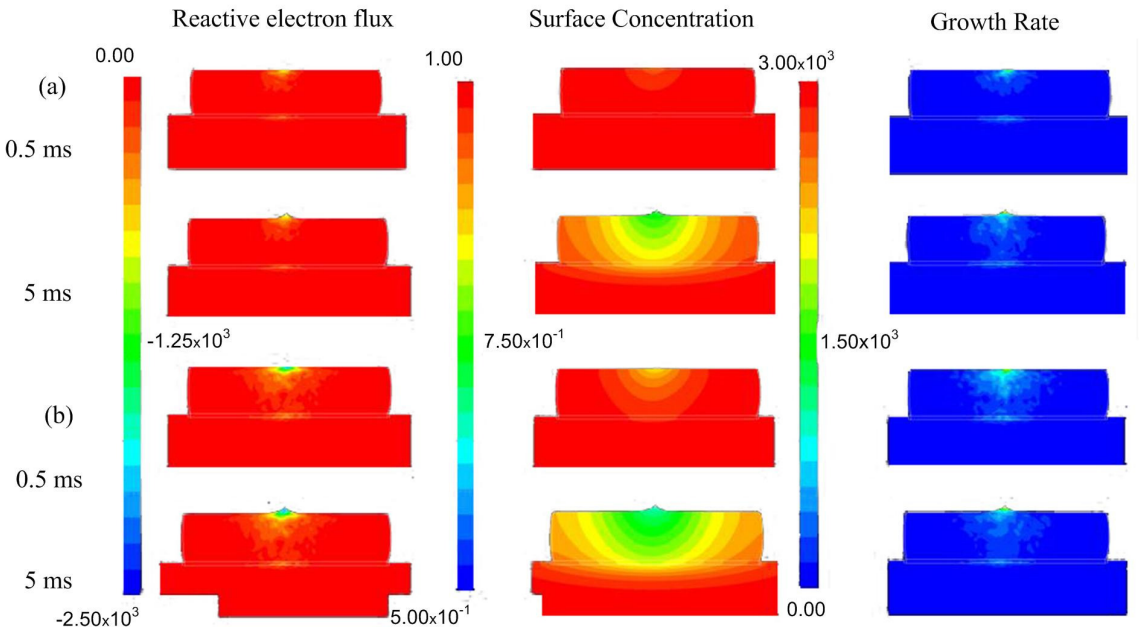

Figure 2.45. Surface distributions (side views along the axis of MWNT) of the reactive electron flux $\dot{Q}_{electrons}^{surf}$ (s^{-1}), precursor concentration C (normalized by C_0), and instantaneous deposit growth rate (nm/s) for the cases of (a) isotropic and (b) anisotropic secondary electron scattering [132].

As expected, in the isotropic scattering case, the secondary electron yield increases with time due to changes in the shape (increased surface area) of the deposit [108]. In the anisotropic scattering case, the secondary electron yield remains constant. This behavior can be attributed to the following competing effects: a decrease in the yield due to shielding of secondary electrons generated within the MWNT by deposited amorphous carbon on the surface of the MWNT and an increase in the yield due to an increase of the surface area of the growing deposit. Deposition of even a few nanometers of amorphous carbon drastically reduces the probability of a secondary electron generated within the MWNT reaching the surface of the deposit. For example, secondary electrons with energies of 10 eV and 50 eV generated next to the surface of the MWNT and travelling through 4 nm of amorphous carbon have probabilities of reaching the surface of ~0.13 and ~1.6×10^{-6}, respectively. The secondary electron yield for the two simulated cases converges towards the same value at the end of the simulated early growth period. This predictions support the experimentally observed fact that deposition of amorphous carbon on the surface of the MWNT rapidly diminishes the impact of properties of the MWNT on the deposition process. As a result, the deposit growth rates and the resulting deposit shape will be similar for the later growth stages

regardless whether the EBID pillar deposits are grown on top of a MWNT or a similarly-sized amorphous carbon line.

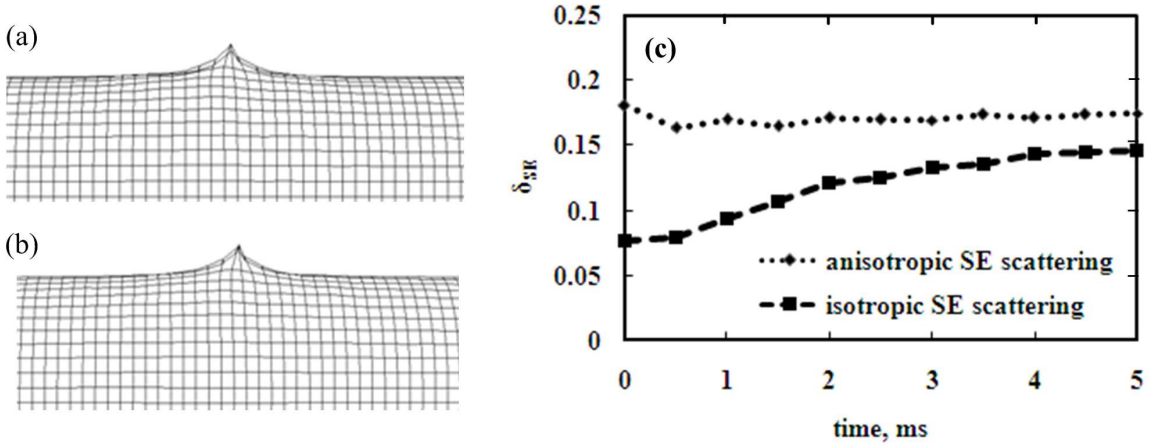

Figure 2.46. Simulated deposit shapes after 5 ms of deposition for (a) isotropic and (b) anisotropic secondary electron scattering within the MWNT (mest grid size of 2 nm in each case), and (c) the corresponding secondary electron yields as a function of time [132].

4.5 Simulation of MWNT-substrate EBID carbon joint formation

In the preceding section it is demonstrated that properties of the MWNT do not impact the process, and only the geometry of the tube influences the EBID growth. The effect of the tube geometry is most pronounced in the early stages of EBID at the edge of the MWNT. In this section, MWNT-substrate EBID carbon connection formation is explored using simulations. Both early and later stages of EBID carbon connection formation at the end of a MWNT with diameter of 30 nm resting on a flat carbon substrate is simulated for low (10 keV) and high (25 keV) electron beam energies, and three electron beam impingement positions. The MWNT is modeled as a carbon cylinder gradually merging into the substrate (see Figure 2.47). The deposit shape evolution, precursor surface concentration, reactive electron flux, and growth rates for varied conditions are analyzed to gain an insight on the potential capabilities of the deposition process.

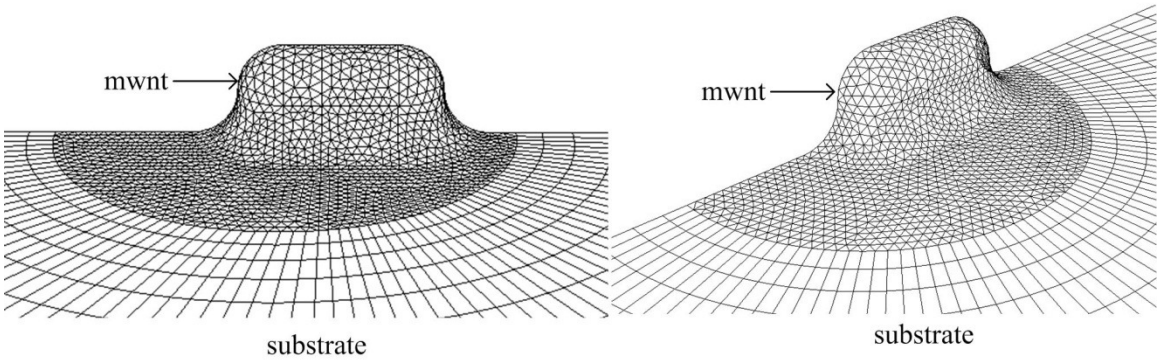

Figure 2.47. Geometry of MWNT with diameter of 30 nm gradually merging into the substrate. Inner region triangular grid size is ~2.5 nm.

4.5.1 Initial EBID growth on MWNT edge

The precursor surface concentration, reactive electron flux, and growth rate at 0.5 ms into the deposition process are shown in Figure 2.48 and Figure 2.49 for electron beam energy of 10 keV and 25 keV and varied electron beam impingement positions.

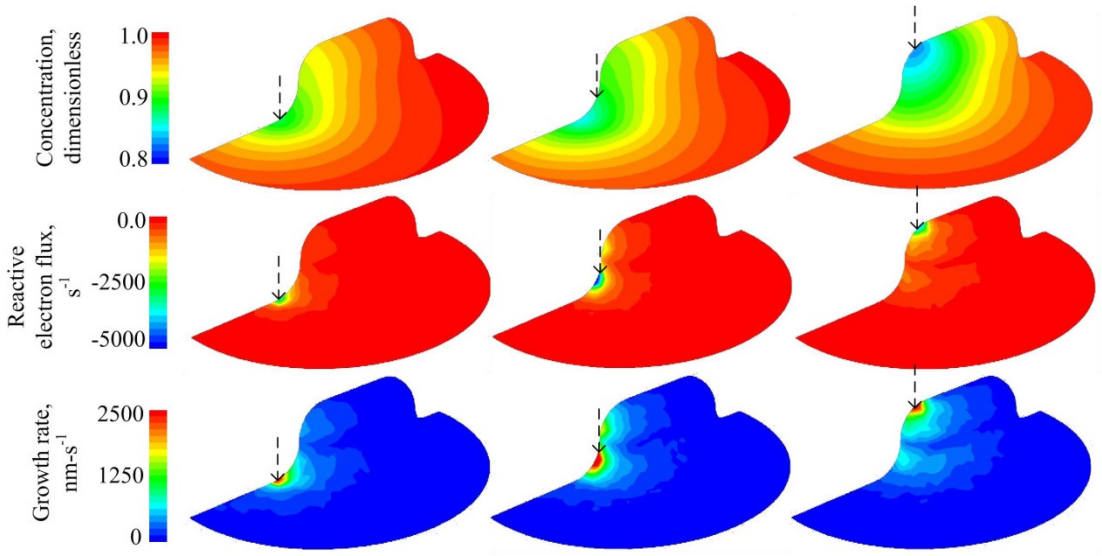

Figure 2.48. Precursor surface concentration, reactive electron flux, and spatial distribution of the deposit growth rate 0.5 ms into the deposition process for electron beam energy of 10 keV, current of 100 pA, and beam diameter of 50 nm for three electron beam impingement locations (indicated with black arrow).

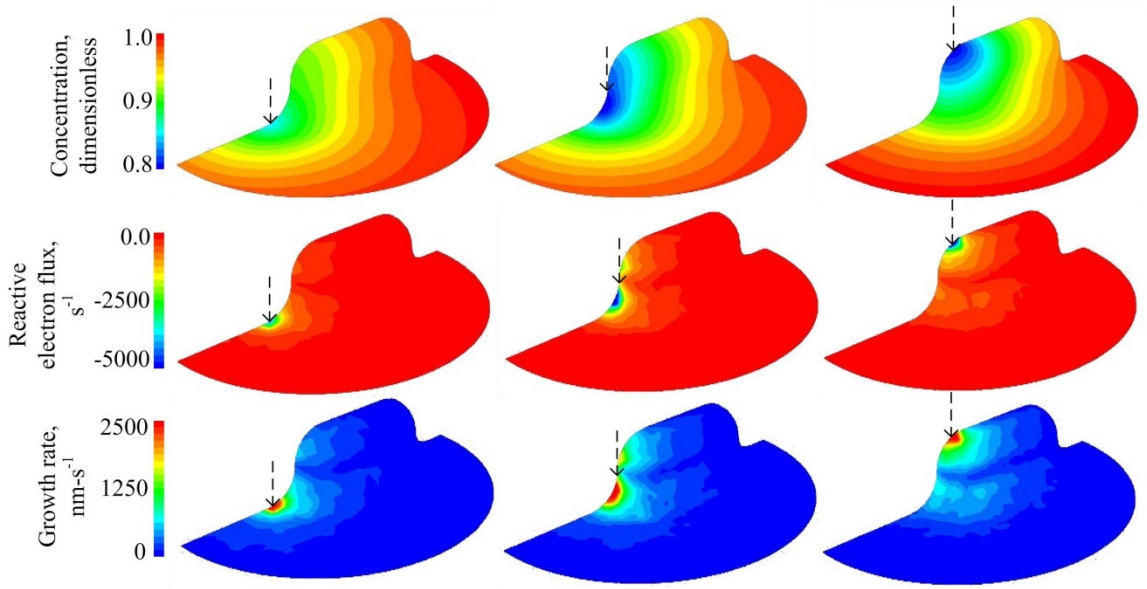

Figure 2.49. Precursor surface concentration, reactive electron flux, and spatial distribution of the deposit growth rate 0.5 ms into the deposition process for electron beam energy of 25 keV, current of 100 pA, and beam diameter of 50 nm for three electron beam impingement locations (indicated with black arrow).

Cross sectional profiles of the carbon deposit along the MWNTs axis during the early growth stages for the low and high electron beam energy and three electron beam impingement position are shown in Figure 2.50 and Figure 2.51, respectively. The corresponding time evolution of secondary electron yield is shown in Figure 2.52.

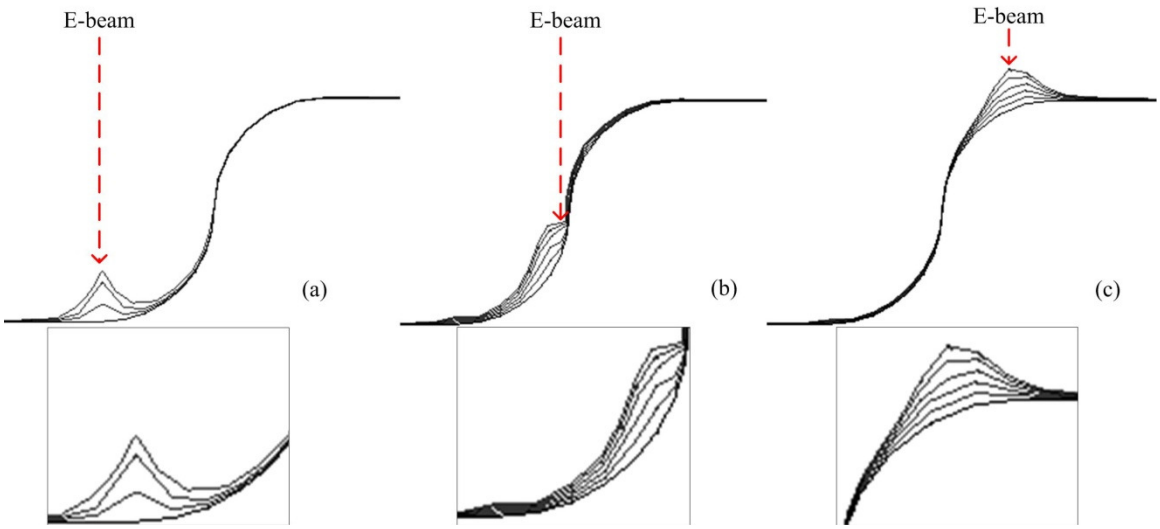

Figure 2.50. Cross sections (along the MWNT axis) of EBID carbon connection formation shown in steps of 0.01 s for electron beam energy of 10 keV, current of 100 pA, and beam diameter of 50 nm for the electron beam impinging (a) on a substrate 10 nm away from the end of MWNT, (b) at the edge of the MWNT and, (c) on MWNT 10 nm away from the MWNT end (simulation mesh size is ~2.5 nm).

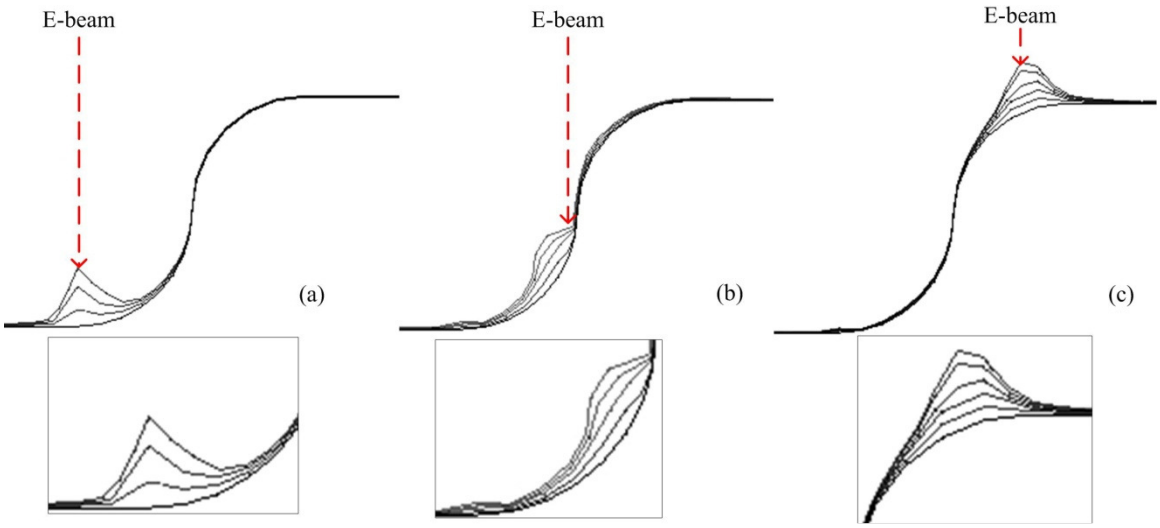

Figure 2.51. Cross sections (along the MWNT axis) of EBID carbon connection formation shown in steps of 0.01 s for electron beam energy of 25 keV, current of 100 pA, and beam diameter of 50 nm for the electron beam impinging (a) on a substrate 10 nm away from the end of MWNT, (b) at the edge of the MWNT and, (c) on MWNT 10 nm away from the MWNT end (simulation mesh size is ~2.5 nm).

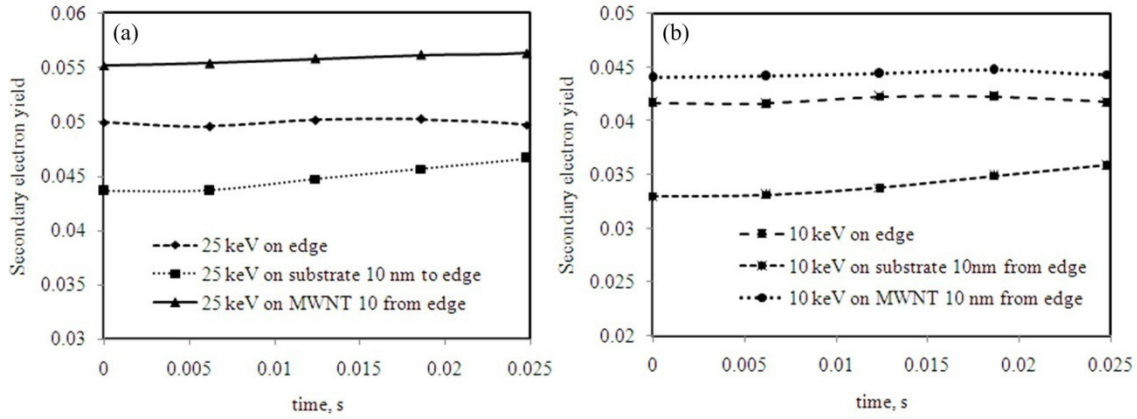

Figure 2.52. Yield of secondary electrons contributing to reactive electron flux (SE with energy above the electron induced dissociation cross section threshold of 10 eV) at early growth stage for electron beam with energy of (a) 25 keV and (b) 10 keV.

The energy of the electron beam does not significantly impact the early growth stages of the deposit. The yield of secondary electrons contributing to the dissociation reaction and thus the reactive electron flux increases with an increase in the electron beam energy. However, the increase in the reactive electron flux is offset by the reduction in the magnitude of the precursor surface concentration; thus, the resulting growth

rate of the deposit is similar for the low and high electron beam energies.

As evident in Figures 4.13 and 4.14, the shape of the EBID carbon deposit strongly depends on the location of electron beam impingement. When the electron beam impinges on the substrate 10 nm away from the edge of the MWNT, the deposit growth is primarily vertical and a typical cone-like EBID pillar begins to form. When the electron beam impinges at the edge of the MWNT, the resulting growth is primarily normal to the MWNT surface and thus the interface begins to locally thicken. When the electron beam impinges on the MWNT about 10 nm away from the edge, the growth is again primarily vertical, similar to the pillar growth on the substrate. In this case however, some growth also occurs on the upper part of the MWNT edge. The secondary electron yield remains constant during the initial deposition stage. Lastly, the yield of secondary electrons contributing to the reaction is highest when the electron beam impinges on the MWNT and lowest when the electron beam impinges on the substrate.

4.5.2 Later-stage EBID growth on MWNT edge

In this section later-stage growth dynamics of the MWNT-substrate EBID carbon connection formation is investigated. Cross sectional profiles along the MWNTs axis of such deposits for the low and high electron beam energy and three electron beam impingement position are shown in Figure 2.53. The corresponding time evolution of secondary electron yield contributing to the dissociation reaction is shown in Figure 2.54. The precursor surface concentration, reactive electron flux, and the growth rate at the final deposition time (0.2s) are shown in Figure 2.55 and Figure 2.56 for electron beam energy of 10 keV and 25 keV and varied electron beam impingement position.

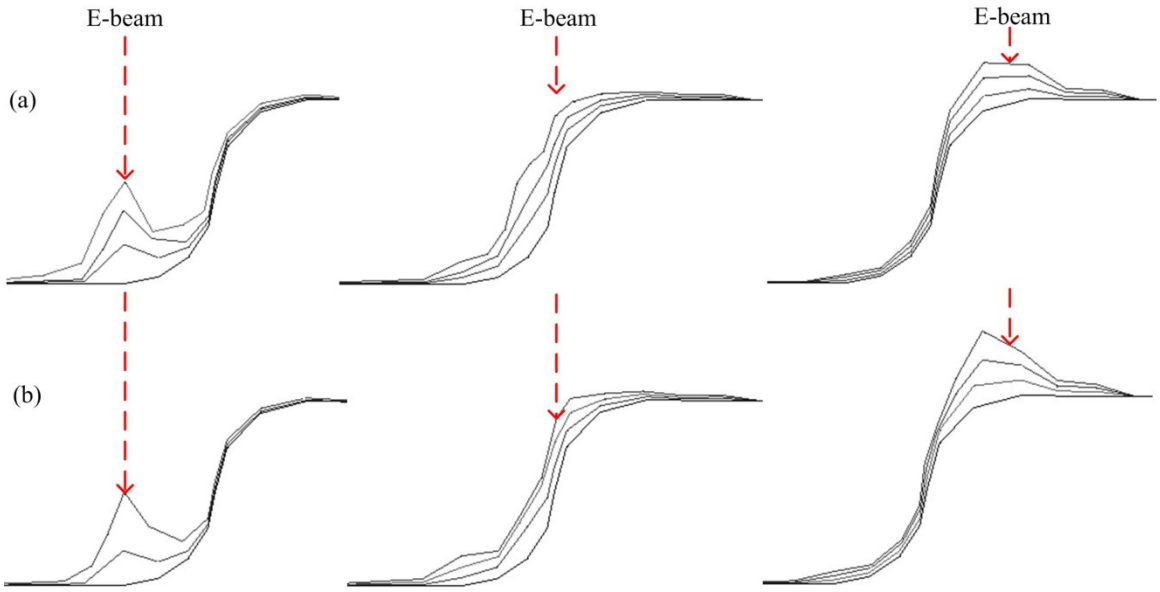

Figure 2.53. Cross sections (along the MWNT axis) of EBID carbon connection formation shown in time steps of 0.07 s for (a) 10 keV and (b) 25 keV beam (simulation mesh size is to ~ 5 nm).

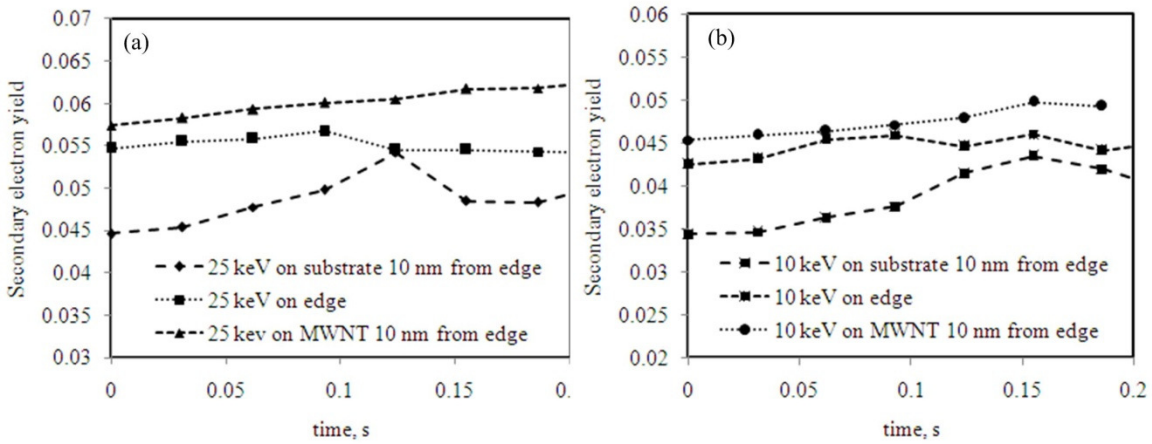

Figure 2.54. Yield of secondary electrons contributing to reactive electron flux (i.e. SE whose energy is above the electron induced dissociation cross section threshold of 10 eV) for later-stage growth with electron beam with energy of (a) 25 keV and (b) 10 keV.

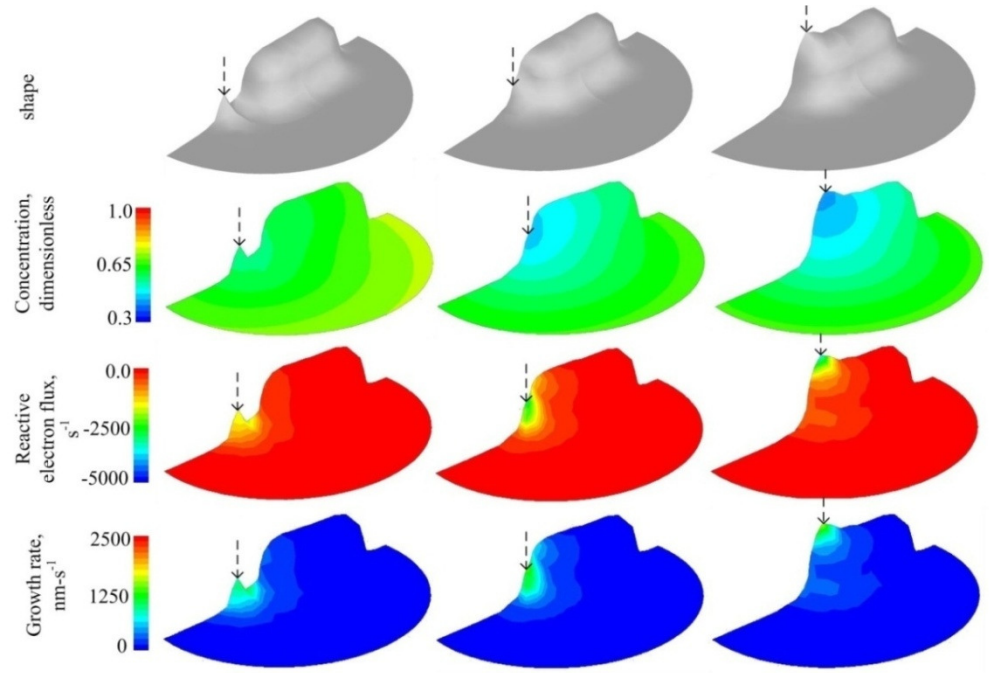

Figure 2.55. Deposit shape, precursor surface concentration, reactive electron flux, and spatial distribution of the deposit growth rate 0.2 s into the deposition process for electron beam energy of 10 keV, current of 100 pA, and beam diameter of 50 nm for three electron beam impingement locations (indicated with black arrow).

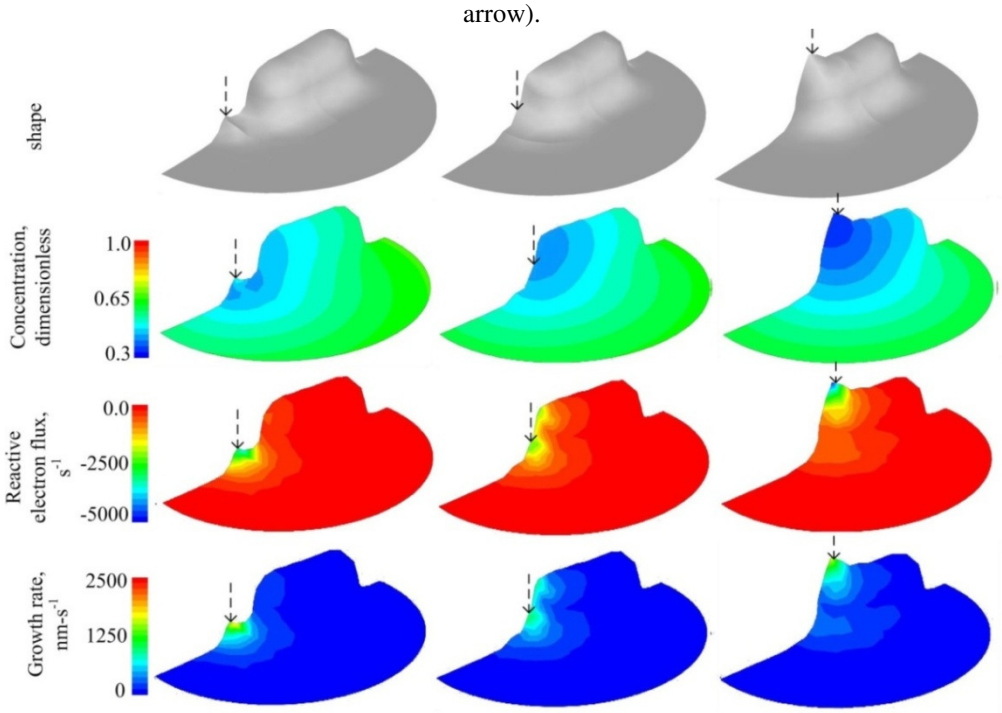

Figure 2.56. Deposit shape, precursor surface concentration, reactive electron flux, and spatial distribution of the deposit growth rate 0.2 s into the deposition process for electron beam energy of 25 keV, current of 100 pA, and beam diameter of 50 nm for three electron beam impingement locations (indicated with black arrow).

Similarly to the initial deposition, the energy of the electron beam does not significantly impact the growth of the deposit during the later-stage of the process. The yield of secondary electrons contributing to the dissociation reaction and thus the reactive electron flux increase with electron beam energy. However, the increase in the reactive electron flux is offset by the reduction in the magnitude of the precursor surface concentration and the resulting growth rate of the deposit is similar for the low and high electron beam energies (see Figure 2.55 and Figure 2.56). The location of the electron beam impingement strongly influences the shape of shape of the EBID carbon joint. As observed during the initial growth stages, impinging an electron beam on the MWNT at ~10 nm away from the edge results in primarily vertical deposit growth. As the process progresses, the cone-shaped deposit begins to form on top of the MWNT and the secondary electron yield increases gradually. A narrower cone forms at higher electron beam energy because of a decreased electron scattering within the cone and MWNT. Focusing the electron beam on the edge of the MWNT causes growth in direction normal to the MWNT surface. While initially most of the growth occurrs on the lower part of the edge, the deposit gradually thickens in the upper part of the edge during the later deposition stages. As a result, at the end of the simulation the deposit uniformly covers most of the MWNT's edge and the secondary electron yield no longer varies significantly. Use of lower electron beam energy results in a more uniform deposit because of higher electron scattering probability near the top of the edge. Impinging the electron beam on the substrate at ~10 nm away from the edge results in typical cone-shaped deposit just as in the case of initial deposit growth. However, as the deposition progresses, the cone widens and begins to merge with the MWNT edge. The secondary electron yield increases during cone formation, but begins to decrease during the merging of the cone and deposit at the MWNT edge. The yield continues to decrease as the cone merges into the MWNT's edge because of the decrease in the surface area of the lower part of the deposit. In summary, depending on the location of the electron beam impingement, the cone-shaped, uniform-film like, or cone-merging-into-the-edge deposits can be formed.

4.6 Concluding remarks

In this Chapter EBID of residual hydrocarbons on MWNTs is investigated. It is found that only secondary electron transport within the MWNT and its geometry can affect the deposition process. A method for measuring of secondary electron yield in free standing MWNT is developed and validated. The measured secondary electron yield is estimated to be in the ~0.05-0.1 range, corresponding to isotropic (K=1) or slightly anisotropic (K=10) secondary electron scattering within the MWNT. However, vibration of the SEM stage, electron beam drift, and deposition of contamination causes significant uncertainty in the measured stage current and makes quantitative comparison to simulation results difficult.

EBID on MWNT resting on silicon substrate is investigated in detail using experiments and simulations. No difference is found in deposit shape grown at different locations along the close and open (FIB-cut) ends of MWNT. The size and geometry of EBID pillar deposits grown on MWNT and on the amorphous carbon lines are found to be similar, indicating a minimal impact of MWNT's properties on growth dynamics of EBID carbon interfaces. The experimental results are confirmed through simulation of early growth of EBID deposits. In particular, it is demonstrated that similar deposit geometries are expected from carbon pillar deposition on structures with isotropic and highly anisotropic secondary electron scattering properties. The physical mechanism responsible for such a behavior is a rapid build-up of a thin amorphous carbon layer on the surface of a MWNT, which prevents the escape of secondary electron generated within the MWNT and therefore diminishes the impact of nanotube properties on the later stages of the EBID growth process. Lastly, the geometrical influence of the MWNT on the EBID process is explored. Both early and later stages of EBID carbon connection formation at end of MWNT with diameter of 30 nm resting on a flat carbon substrate is investigated for low (10 keV) and high (25 keV) electron beam energies as a function of the electron beam impingement positions. The electron beam impingement location was found to have much stronger impact on the deposit shape than the beam energy. The energy of the electron beam does not significantly impact the deposition process due to the interplay between the magnitudes of the reactive electron flux, the precursor surface concentration, and product of the two (the growth rate). Impinging the electron beam on the MWNT a few nanometers away from its

edge produces cone-shaped deposits and is the least useful for improvement of electrical contact properties of the interface. Focusing the beam directly on the edge of the MWNT produces uniform film-like deposit and is most applicable to establishing an efficient electrical contact with the outer shell of the MWNT. Initially, impinging the electron beam on the substrate ~10 nm away from the edge results in a cone-shaped deposit. However, as the deposition progresses, the cone widens and begins to merge with the edge of the MWNT. While establishing of contact with outer shell of the MWNT is the slowest in this case, this approach provides an opportunity for growing a deposit into the open end of the MWNT.

CHAPTER 5

CONCLUSIONS AND RECOMMENDATIONS FOR FUTURE WORK

5.1 Summary

High contact resistance of MWNT-substrate interface is one of the major obstacles impeding application of MWNT in electrical and electronic devices such as interconnects and tips for conductive force microscopy (CFM). Bachtold et al. [16] demonstrated that EBID of carbon MWNT-substrate connection significantly lowers the interface contact resistance. In this work, factors contributing to the EBID formation of the carbon connection to MWNT and their influence on the contact resistance are explored experimentally and theoretically. A dynamic growth model of EBID of carbon is developed, implemented, and validated. Physical conditions corresponding to diffusion-limited, mixed, and reaction-limited growth regimes, as well as their impact on the growth rate and shape of the EBID deposits, are quantified. Simulation results are compared to experiments and a good agreement is found in observed topology of complex ring-within-pillar deposits. Furthermore, simulations correctly capture the dependence of the ring-diameter on the energy of the electron beam, as well as the growth rates of the central pillar and the ring. The MWNT properties are found to have minimal impact on the interface growth dynamics of the EBID process, due to shielding of secondary electrons generated within the tube by the rapidly deposited amorphous carbon layer on the surface of the tube. As demonstrated through simulations, focusing of the electron beam on the substrate next to the tube's end produces a cone-like deposit, which eventually merges with the tube. In contrast focusing the electron beam directly on the tube's end produces a uniform and conformal film-like carbon coating around the outer shell of MWNT. The bulk resistance of the carbon joint is found to be a dominating factor contributing to the total resistance of the MWNT interconnect. It is also found that a significantly smaller contact area of deposited carbon is sufficient, as compared to that between the carbon and metal pad, in order to make an Ohmic interconnect junction. With sufficient dimensions of the EBID carbon joint and reduction of the resistivity of the material induced by its partial graphitization, the resistance of the MWNT interconnect can be reduced to

the range of the theoretical limit for the outer-shell MWNT electrical conduction.

5.2 Original contributions and publications

The following are original contributions of this work:

- Formulation, implementation, and validation of a comprehensive dynamic growth model of the EBID process using residual hydrocarbons as a precursor;
- Identification of physical conditions corresponding to diffusion-limited, mixed, and reaction-limited growth regimes, as well as their impact on the growth rate and shape of the EBID deposits;
- Determination of the physical mechanism behind the experimentally-observed formation and growth dynamics of complex ring-within-pillar deposits;
- Theoretical and experimental quantification of the impact of MWNT on the growth dynamics of the EBID process;
- Theoretical and experimental quantification of the role of electron beam impingement location and electron beam energy on resulting shape of MWNT-electrode EBID carbon connections;
- Determination of dominating factors contributing to the resistance of the MWNT interconnects;
- Determination of the relative importance of the mechanical contact area of the EBID-made carbon joint to MWNT and the metal electrode.

The following publications and presentations resulted from this thesis research:

Refereed Journal Publications

- Rykaczewski, K., White, W.B., and Fedorov, A., *Analysis of electron beam induced deposition (EBID) of residual hydrocarbons in electron microscopy*, Journal of Applied Physics A, 101 (5), 054307-054319 (2007).
- Fedorov, A., Rykaczewski, K., and White, W., *Transport issues in focused electron beam chemical vapor deposition*, Surface & Coatings Tech., 201(22-23):p.8808-8812, (2007).
- Rykaczewski, K., Marshall, A., White, W.B., and Fedorov, A., *Dynamic growth of carbon nanopillars and nanorings in electron beam induced dissociation of residual hydrocarbons on semiconductor substrate*, Ultramiscroscopy., 108 (9), (2008).

- Rykaczewski, K., Henry, M.R., Fedorov, A.G., *Electron Beam Induced Deposition (EBID) of residual hydrocarbons in the presence of a multiwall carbon nanotube.* Applied Physics Letters 95, 113112 (2009).
- Rykaczewski, K., Kulkarni, D., Singamaneni, S., Henry, M.R., Kim, S.K., Tsukruk, V. V., Fedorov, A.G., *Effect of Electron Beam Induced Deposited (EBID) Carbon Joint Geometry and Material Properties on Electrical Resistance of Multiwalled Carbon Nanotube (MWNT)-to-Metal Contact Interface.* Nanotechnology, submitted, October 2009.

Conference Presentations:

- Rykaczewski, K, Fedorov A.G., *Electron Beam Induced Deposition (EBID) of Carbon Interface between Carbon Nanotube Interconnect and Metal Electrode*, Symposium BB: Material Systems and Processes for Three-Dimensional Micro- and Nanoscale Fabrication and Lithography, *MRS 2009 Spring Meeting.*
- Rykaczewski, K, White W.B., Browning J., Marshall A.D., Fedorov A.G., *Dynamic model of electron beam induced deposition (EBID) of residual hydrocarbons in electron microscopy, ASME, Heat Transfer Division,* Proceedings of 2006 ASME IMECE 2006 - *Heat Transfer*, 2006, 1p

5.3 Recommendations for future work

5.3.1 Quantitative simulations of EBID of residual hydrocarbons

An opportunity for improvement in the three-dimensional EBID simulation model is in enhancing the deposit growth algorithm and the remeshing procedure of the deformed grid. As discussed in Chapter 2, with the current growth algorithm an extremely small grid size (0.05 nm) is required for achieving grid independence. As shown in Figure D.9, decreasing the grid size significantly increases the number of computational cells, the number of iterations, and the time required for simulation of electron transport. A finer mesh also requires a significant increase in the number of simulated primary electrons for accurate

capture of the reactive electron flux spatial distribution. With grid size as fine as 0.05 nm, the required number of primary electrons is significantly higher than the number of electrons impinging on the substrate within the period of time that the reactive electron flux is updated. Thus, simulating contribution of each of the primary electrons to the deposit growth may become more efficient in this case.

The growth algorithm can be improved in two ways. First, the current algorithm can be refined by using a linear interpolation of these variables between the values at cell centers in performing numerical integration instead of assuming a constant value of precursor concentration and reactive electron flux within each cell. While this approach should allow for more accurate capturing of high gradients of reactive electron flux with a larger grid size, it may be difficult to implement on an unstructured triangular grid in three dimensions. Also, this approach will not resolve the remeshing problems associated with deposit growth. Another approach can be recommended in which a contribution of each of the incident electrons to the growth is accounted for directly using the cellular automata method [38]. Example of two-dimensional cellular automata EBID growth simulation is shown in Figure 5.1, which can be readily extended to three dimensions.

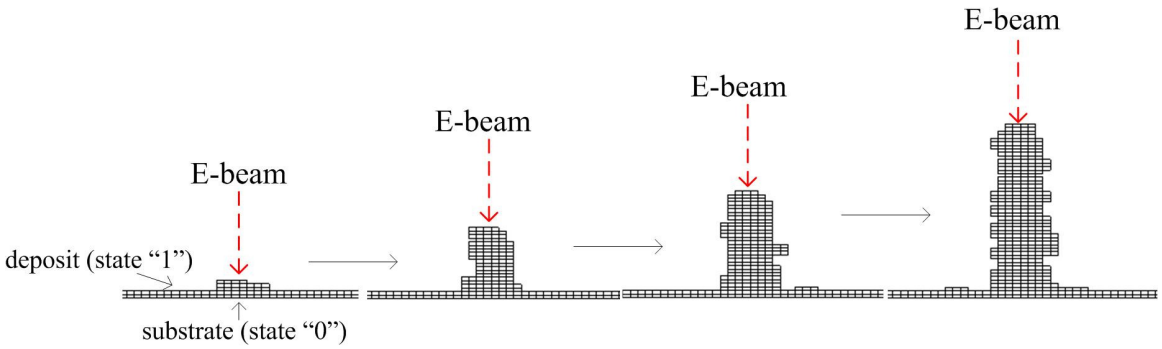

Figure 5.1. Example of cellular automata EBID deposit growth.

Specifically, as in work of Silvis-Cividijan [38] each precursor atom on the surface can be represented by an "atomic size" cube and can be dissociated (its state is changed from "adsorbed" to "deposit") based on a dissociation probability criterion, which is a function of secondary electron energy, dissociation/ionization cross section, and surface concentration of the precursor. Rather than continuously updating the concentration profile and only periodically updating the reactive electron flux, the deposition rate (and the deposit shape) can be updated continuously (with each secondary electron leaving the substrate) and the

concentration can be updated periodically based on the local time-average of the reactive electron flux and an approximate reconstruction of the deposit surface. This direct approach does not need any remeshing algorithm, and would allow for simulation of arbitrarily complex geometries, such as a full cylinder (MWNT) on top of a flat substrate.

Further simplification of the simulation can be achieved by taking into account the fact the concentration of the precursor within the relatively small reaction zone (flat substrate or nanotube end) reaches a quasi-steady state after a brief initial period of the deposition process. The time scale for reaching of the quasi-steady state concentration profile is proportional to the ratio of the characteristic length scale for the deposition process (electron beam diameter) squared and the representative adsorbed precursor surface diffusion coefficient. For simulations beyond that time the transient evolution of the surface concentration does not need to be computed and the quasi-steady state concentration distribution along the surface of the deposit can be utilized without sacrificing the accuracy of simulations. The assumption of a steady state concentration profile is easily integrated into the FLUENT and cellular automata simulations and significantly simplifies and speeds up the simulation.

5.3.2 Experimental demonstration of EBID contact with inner shells of MWNT

Establishing an electrical contact to inner shells of a MWNT should allow for lowering of the interconnects resistance to a few ohm range. Two key issues have to be resolved in order to accomplish this goal. First, a method for production of clean open-ended MWNT has to be developed. Second, the EBID-made carbon joint has to be deposited in a way such that it establishes contact with the inner shells. The findings of this thesis research suggest several potential solutions for resolving these problems:

- As it is demonstrated in this thesis the MWNT powder annealing, water assisted electron beam etching, and FIB cutting are unable to cut the MWNT ends (i.e, open up an access to all shells) without causing detrimental damage to the tube or to the electrode. However, it is observed in laboratory that the MWNT tend to break into smaller pieces while being dispersed in a solution and subjected to ultrasonication. Ultrasonicating a solution with dispersed MWNT for an extended period of time (~0.5 to 1 h or more) produces primarily

very short (~500 nm or less) tubes. Starting out with long MWNT (~10-40 μm) in DMF and sonicating the solution for a controlled period of time may potentially produce shorter MWNT with open ends due to the tube breakage. To increase a chance of having two open ends, MWNT grown with one end open can be used as a precursor material.

- As demonstrated through simulations in Chapter 4, focusing the electron beam on the substrate next to the edge of the MWNT or directly on the edge produces a deposit which establishes contact to the edge/end of the tube. It is difficult to assess whether deposition of uniform film-like deposit over the edge/end of the tube or merging of a cone-shaped deposit with the edge/end of the tube would produce a better mechanical (and with that electrical) contact to the inner shells of the MWNT. While in Chapter 3 it is demonstrated that only a small contact area to the outer shell of a MWNT is sufficient for a good electrical contact, it is difficult to quantify how small of a contact area is sufficient for good electrical contact with inner shells of the tube (direct physical contact with just the end each shell (a ring) might not be sufficient). However, the fact that the precursor atoms can efficiently diffuse within carbon the nanotubes [135] suggests a possibility of amorphous carbon deposition within the MWNT. As illustrated in Figure 5.2, focusing the electron beam on the substrate next to the MWNTs end would be highly advantageous because it would allow for diffusion adsorbed precursor into the MWNT.

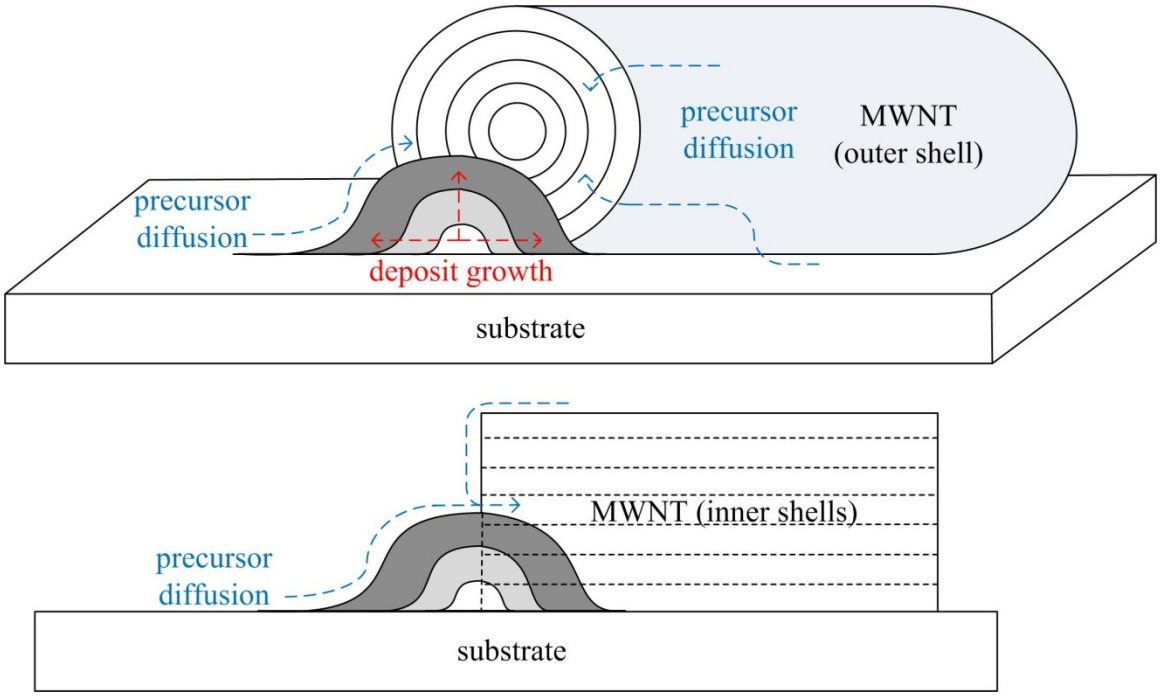

Figure 5.2. Schematic of proposed method for establishing contact with MWNT's inner shells: top is a 3-D view, a bottom is a cut along the MWNT axis.

APPENDIX A: METHOD FOR ACCOUNTING FOR VARIED SUBSTRATE PROPERTIES

Constant surface properties are assumed in the derivation of the surface transport equation, (Equation 2.4). A method outlined by Phillips and Fedorov [136] is used to modify the governing equation to account for the difference between deposit and substrate transport properties. Let us assume that concentration C_1 with surface diffusion coefficient D_1 describe the precursor state on the surface of the deposit. Likewise, surface concentration C_2 with surface diffusion coefficient D_2 describe precursor on the surface of the bare substrate. The transition between the two surfaces (deposit-to-substrate) occurs at the edge of the deposit at $s = s_{tr}$. Then, the same surface transport equation can be used to describe any changes in the precursor concentration, valid at their respective application domain (i.e., surfaces of the deposit and substrate, respectively):

$$\begin{aligned}\frac{\partial C_1}{\partial t} &= \frac{1}{r}\frac{\partial}{\partial s}\left(D_1 r \frac{\partial C_1}{\partial s}\right) - C_1\dot{Q}_1 \\ \frac{\partial C_2}{\partial t} &= \frac{1}{r}\frac{\partial}{\partial s}\left(D_2 r \frac{\partial C_2}{\partial s}\right) - C_2\dot{Q}_1\end{aligned} \qquad \text{A.1}$$

The following initial and boundary conditions apply:

$$\begin{aligned}&I.C. \quad C_1\big|_{t=0} = C_{1,0} \;\;\&\;\; C_2\big|_{t=0} = C_{2,0} \\ &B.C. \quad \left.\frac{\partial C_1}{\partial s}\right|_{s=0} = 0 \;\;\&\;\; C_2\big|_{s\to\infty} = C_{2,\infty}\end{aligned} \qquad \text{A.2}$$

and concentration and flux continuity has to be satisfied at the transition point $s = s_{tr}$, i.e.,

$$\begin{aligned}&C_1\big|_{s=s_{tr}} = KC_2\big|_{s=s_{tr}} = C'\big|_{s=s_{tr}} \\ &D_1\left.\frac{\partial C_1}{\partial s}\right|_{s=s_{tr}} = D_2\left.\frac{\partial C_2}{\partial s}\right|_{s=s_{tr}} = \frac{D_2}{K}\left.\frac{\partial C'}{\partial s}\right|_{s=s_{tr}}\end{aligned} \qquad \text{A.3}$$

where K is the partitioning coefficient. Using the modified surface concentration $C'(s,t)$ defined in Equation A.3 as new dependent variable, Equation A.1 can be combined to make the continuity conditions Equation A.3 automatically satisfied, yielding a single surface transport equation for all materials simulated:

$$\alpha\frac{\partial C'}{\partial t}=\frac{1}{r}\frac{\partial}{\partial s}\left(Dr\frac{\partial C'}{\partial s}\right)-\beta C'\dot{Q}''_1$$

$$0<s\le s_{tr} \qquad \alpha=1,\ D=D_1,\ \beta=1 \qquad \text{A.4}$$

$$s_{tr}<s<\infty \quad \alpha=\frac{1}{K},\ D=\frac{D_2}{K},\ \beta=\frac{1}{K}$$

with the initial conditions

$$C'\big|_{t=0}=\begin{cases}C_{1,0} & 0<s\le s_{tr}\\ KC_{2,0} & s_{tr}<s<\infty\end{cases} \qquad \text{A.5}$$

and boundary conditions

$$\left.\frac{\partial C'}{\partial s}\right|_{s=0}=0 \ \ \& \ \ C'\big|_{s\to\infty}=KC_{2,\infty} \qquad \text{A.6}$$

APPENDIX B: SCALING ANALYSIS OF THE SURFACE TRANSPORT EQUATION (STE)

Different growth regimes can be deduced from the surface transport equation (STE) by applying scaling analysis. Depending on the relative magnitudes of the three time scales associated with the equation, three possibilities are:

1. $t_{\text{diff}} \gg t_{\text{sink}}$
2. $t_{\text{diff}} \ll t_{\text{sink}}$
3. $t_{\text{diff}} \sim t_{\text{sink}}$

Depending on the observation time scale t_{obs} of interest various physical scenarios can be observed as discussed below.

1. $\boldsymbol{t}_{\text{diff}} \gg \boldsymbol{t}_{\text{sink}}$

Different possibilities for the observation time in this case are schematically shown in Figure B.1.

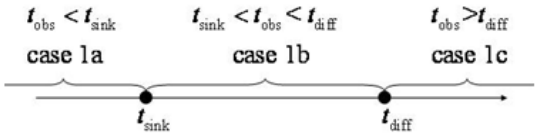

Figure B.1. Regime map for case 1: $\boldsymbol{t}_{\text{diff}} \gg \boldsymbol{t}_{\text{sink}}$

In case 1a, $\frac{\boldsymbol{t}_{\text{obs}}}{\boldsymbol{t}_{\text{diff}}} \ll \frac{\boldsymbol{t}_{\text{obs}}}{\boldsymbol{t}_{\text{sink}}} \leq 1$ which implies that diffusion is in a "frozen" quasi-steady state and the storage term on the left hand side (LHS) is balanced by the sink (reaction) term on the right hand side (RHS) of Equation 2.8 leading to the analytical solution for the precursor concentration in the form of $\boldsymbol{C}^* = \boldsymbol{C}_0 * \exp\left(-\frac{\boldsymbol{t}_{obs}}{\boldsymbol{t}_{\text{sink}}} \dot{\boldsymbol{Q}}_S * \boldsymbol{t}^*\right)$. In case 1b, the observation time scale has a magnitude between the mass sink (reaction) time scale and the diffusion time scale. If $\boldsymbol{t}_{\text{obs}}$ is of the same order of magnitude as $\boldsymbol{t}_{\text{sink}}$ than same solution as in case 1a applies. In case $\frac{\boldsymbol{t}_{\text{obs}}}{\boldsymbol{t}_{\text{diff}}} \ll 1 \ll \frac{\boldsymbol{t}_{\text{obs}}}{\boldsymbol{t}_{\text{sink}}}$ all terms in the Equation 2.8 are unbalanced. The mass sink (reaction) is much faster than diffusion and reaches equilibrium. Thus, complete

consumption of the precursor occurs leading to a trivial solution of vanished surface concentration everywhere where the mass sink is non-zero ($s<s_c$). Outside of this complete-consumption domain ($s<s_c$), the concentration field is quasi-steady ("frozen") and described by the solution of the following problem:

$$\frac{\boldsymbol{t}_{obs}}{\boldsymbol{t}_{diff}}\frac{\partial}{\partial \boldsymbol{s}^*}\left(\boldsymbol{r}^*\frac{\partial \boldsymbol{C}^*}{\partial \boldsymbol{s}^*}\right)=0 \quad \text{where } \boldsymbol{s} > \boldsymbol{s}_c$$
$$\boldsymbol{C}^*\big|_{s=s_c} = 0 \;\&\; \boldsymbol{C}^*\big|_{s\to\infty} = \boldsymbol{C}^*_{\infty} \qquad \text{B.1}$$

If $\boldsymbol{t}_{\text{obs}}$ is of the same order of magnitude as $\boldsymbol{t}_{\text{diff}}$ the reaction reaches equilibrium immediately (on the observation time scale) and consumes all reagent wherever the mass sink in non-zero. Outside of this region the surface concentration will evolve in a transient fashion described mathematically by:

$$\boldsymbol{C}^* = 0 \;\text{ where }\; \boldsymbol{s} \le \boldsymbol{s}_c$$
$$\frac{\partial \boldsymbol{C}^*}{\partial \boldsymbol{t}^*} = \frac{\boldsymbol{t}_{obs}}{\boldsymbol{t}_{diff}}\frac{\partial}{\partial \boldsymbol{s}^*}\left(\boldsymbol{r}^*\frac{\partial \boldsymbol{C}^*}{\partial \boldsymbol{s}^*}\right) \quad \text{where } \boldsymbol{s} > \boldsymbol{s}_c$$
$$\boldsymbol{B.C.}\;\; \boldsymbol{C}^*\big|_{s=s_c} = 0 \;\&\; \boldsymbol{C}^*\big|_{s\to\infty} = \boldsymbol{C}^*_{\infty} \qquad \text{B.2}$$
$$\boldsymbol{I.C.}\;\; \boldsymbol{C}^*(\boldsymbol{t}=0,\boldsymbol{s}) = \boldsymbol{C}^*_0$$

The case 1c, $1 \le \frac{\boldsymbol{t}_{\text{obs}}}{\boldsymbol{t}_{\text{diff}}} \ll \frac{\boldsymbol{t}_{\text{obs}}}{\boldsymbol{t}_{\text{sink}}}$, is identical to the case described by Equation B2.

2. $\boldsymbol{t}_{\text{diff}} \ll \boldsymbol{t}_{\text{sink}}$

Different possibilities for the observation time in this case are schematically represented in Figure B.2.

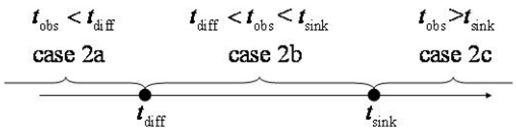

Figure B.2. Regime map for case 2: $\boldsymbol{t}_{\text{diff}} \ll \boldsymbol{t}_{\text{sink}}$

In case 2a, $\frac{\boldsymbol{t}_{\text{obs}}}{\boldsymbol{t}_{\text{sink}}} \ll \frac{\boldsymbol{t}_{\text{obs}}}{\boldsymbol{t}_{\text{diff}}} \le 1$ implies that the reaction can be treated as being in "frozen" quasi-steady state.

The diffusion term balances the storage term resulting in:

$$\frac{\partial C^*}{\partial t^*} = \frac{t_{obs}}{t_{diff}} \frac{1}{r^*} \frac{\partial}{\partial s^*} \left(r^* \frac{\partial C^*}{\partial s^*} \right)$$
$$\left. \frac{\partial C^*}{\partial s^*} \right|_{s=0} = 0 \;\&\; C^*|_{s \to \infty} = C^*_{\infty} \;\&\; C^*|_{t=0} = C^*_0 \qquad \text{B.3}$$

In case 2b, the t_{obs} is shorter than t_{sink} and longer than t_{diff}. If t_{obs} and t_{diff} are of the same order of magnitude the situation is the same as in case 2a. If $\frac{t_{obs}}{t_{sink}} \ll 1 \ll \frac{t_{obs}}{t_{diff}}$ all terms in Equation 2.8 are unbalanced which implies that the reaction is in a "frozen" quasi steady state and the diffusion is instantaneously fast reaching true steady-state described using the steady-state mass conservation:

$$\frac{1}{r^*} \frac{\partial}{\partial s^*} \left(r^* \frac{\partial C^*}{\partial s^*} \right) = 0$$
$$\left. \frac{\partial C^*}{\partial s^*} \right|_{s=0} = 0 \;\&\; C^*|_{s \to \infty} = C^*_{\infty} \qquad \text{B.4}$$

Solving Equation B.4 results in a uniform concentration distribution $C^*(r^*) = C^*_{\infty}$ implying equilibrium. In the case when t_{obs} and t_{sink} are of the same order of magnitude diffusion is instantaneously fast and leads to equilibrium with a uniform surface concentration $C^*(r^*) = C^*_{\infty}$ while the storage of the surface-adsorbed precursor is balanced by the reaction:

$$\frac{\partial C^*}{\partial t^*} = -\frac{t_{obs}}{t_{sink}} C^* \dot{Q}_S^* \qquad \text{B.5}$$

Equation B.5 is a subject to initial condition of a total amount of the reacting species deposited on the substrate being fixed. Since $C^* = C^*(t^*) \neq f(s^*)$, we can integrate Equation B.5 over the substrate/deposit surface area and also in time, yielding:

$$C^*(t^*) = C_0^* \exp\left(-\frac{t_{obs}}{t_{sink}} \frac{\int_0^{t^*} \int_{A_{sub}} \dot{Q}_s(s,t) dA dt'}{A_{sub}} \right) \qquad \text{B.6}$$

Special case of infinite supply of the deposited species corresponds to infinite area of the substrate, which reduces Equation B.6 to an uniform and constant in time concentration $C^*(t^*) = C_0^*$.

In case 2c, if the t_{obs} and t_{sink} are of the same order of magnitude the situation can be also described using

Equation B.6.

3. $\tau_{diff} \sim \tau_{sink}$

In this case both the diffusion and mass sink (reaction) time scales are of the same order of magnitude and both need to be considered. If the observation time scale is much shorter than τ_{diff} and τ_{sink} the problem becomes trivial—on this time scale nothing happens, as neither diffusion nor reaction has a chance to perturb the initial concentration. In case the observation time is much longer than τ_{diff} and τ_{sink} diffusion will balance the reaction, and the steady-state will result:

$$\frac{\tau_{sink}}{\tau_{diff}} \frac{1}{\rho^*} \frac{\partial}{\partial \sigma^*} \left(\rho^* \frac{\partial C^*}{\partial \sigma^*} \right) - C^* \dot{Q}_S^* = 0$$
$$\left. \frac{\partial C^*}{\partial \sigma^*} \right|_{\sigma=0} = 0 \quad \& \quad C^*|_{\sigma \to \infty} = C^*_{\infty} \qquad \text{B.7}$$

APPENDIX C: MC ELECTRON TRANSPORT AND GENERATION SIMULATION

C.1. Monte Carlo Modeling

In MC simulations of electron transport, it is assumed that an electron is a point particle undergoing elastic and inelastic collisions with a linear trajectory in between. An elastic collision can occur due to electronic repulsion in electron-free electron collision or due to large mass difference in an electron-nucleus collision. On the other hand, an inelastic collision can occur during electron interaction with inner shell electrons (ionization--production of x-ray or Auger electron), with valence electrons (production of secondary electrons), and with crystal lattice (production of phonons). For an individual collision the type of interaction an electron has is random. With ~10^9 electrons impinging on a substrate per second in a SEM with electron beam current of ~100 pA, a realistic approximation of the electron transport can be achieved by sampling the type of individual events from a uniform random number distribution (R). For example, if the probability of an inelastic collision occurring is P_1, setting a criterion of $P_1 > R$ for occurrence of an inelastic collision and repeating such test many times should approximate the right number of inelastic events occurring. As shown in Equation C.1, this approach can be generalized to sample any type of variable y with a probability function $p(y)$:

$$R = \frac{\int_0^x p(y)dy}{\int_0^{x_{MAX}} p(y)dy} \quad \rightarrow \quad \text{x=Fnx(R)} \qquad \text{C.1}$$

Where x is any number between 0 and x_{MAX}. As shown, Equation C.1 can be rearranged so that x is a function of the random number R.

Once the type of collision that the electron will undergo is determined, the mean free path (MFP), angle of deflection α, and energy lost (ΔE) have to be determined. In addition, during an inelastic collision possibility of generating a secondary electron has to be taken into consideration. The following sections will describe the models used to obtain these key variables.

C.2. Primary Electron Scattering and Secondary Electron Generation Models

The Primary Electron beam impinging on the substrate is described by its location on the surface,

energy, and beam current. Energy and current of the beam are assumed to be constant and set to parameters similar to experimental values. Primary beam defocusing due to precursor gas molecules is neglected and the surface distribution of the incident beam is assumed to be Gaussian. A Gaussian random number with a standard deviation (σ) of 1 is generated by converting a uniform random number using the polar form of the Box-Muller transformation [137]. The standard definition of an electron beam diameter (d) is the full width half maximum (FWHM), which corresponds to ~2.35σ of a Gaussian beam distribution.

For scattering within a single material, the total mean free path, λ_T, of the electron is determined by the elastic, λ_{el}, and the inelastic, λ_{in}, mean free paths. The distance (step) between two collisions is sampled using a random number *R* following the Poisson distribution [76].

$$\text{step} = -\lambda_T \ln R = -\left(\frac{1}{\lambda_{el}} + \frac{1}{\lambda_{in}}\right)^{-1} \ln R \qquad \text{C.2}$$

For simulation of a multipart target with characteristics dimensions comparable to the mean free path of the electron approach taken by Li et al. [77] and Yue et al. [78] has been adopted. Specifically, the step length is equal to the sum of lengths of individual zones, r_i, along the path of the electron and partial length of the last zone, T_m (see Figure C.1). The partial length of the last zone is determined as follows [138]:

$$\sum_{i=1}^{m-1} \frac{r_i}{\lambda_i} + \frac{T_m}{\lambda_m} = -\ln R \qquad \text{C.3}$$

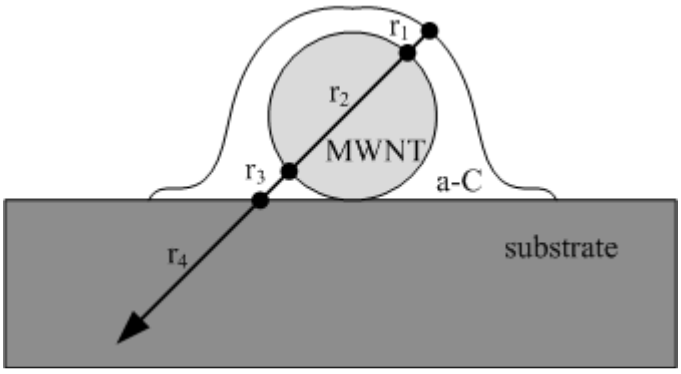

Figure C.1. Illustration of the electron step length in a multipart sample.

Since primary electrons of interest have energies higher than 10 keV in the multipart zone of the

simulation, the small energy change associated with passing boundary between two materials with different Fermi energies and work functions [78] was neglected.

In general, a mean free path can be calculated from the scattering cross section , σ, in the following manner [76]:

$$\lambda = \frac{A}{N_A Z \rho \sigma} \qquad \text{C.4}$$

Dependent on the energy of the primary electron, the elastic mean free path and scattering angles are calculated using either the Rutherford or the Mott cross-sections [76]. The Rutherford cross section (Equation C.5) is utilized for electrons with energies higher than 5keV while the Browning [139, 140] approximation to the Mott cross section (Equation C.7) is utilized for electron below this threshold.

The Rutherford total cross section corrected for relativistic effects and screening of the nucleus by inner shell electrons for an electron of energy E scattered for a scattering angle θ is calculated using the following equations. The derivation of the formula can be found in M. Dapor's book [141].

$$\sigma_{el} = 5.21e-21\frac{Z^2}{(0.001E)^2}\left(\frac{0.001E+mc^2}{0.001E+2mc^2}\right)\frac{4\pi}{\alpha(1+\alpha)}[cm^2]$$
$$\alpha = \frac{(3.4e-3)Z^{2/3}}{0.001E} \qquad \cos\theta = 1 - \frac{2\alpha \mathrm{R}}{1+\alpha-\mathrm{R}} \qquad \text{C.5}$$

Where mc^2 is the rest energy of an electron and α is the screening parameter. The relativistic Mott differential elastic cross section per element solid angle can be expressed as:

$$\frac{d\sigma_{el}}{d\Omega} = |f(\theta)|^2 + |g(\theta)|^2 \qquad \text{C.6}$$

Where f(θ) and g(θ) are the scattering amplitudes obtained from the partial wave expansion solution of Pauli-Dirac's equation and $d\Omega$ is the element solid angle. No analytical solution to Equation C.6 exists. Tabulated data sets are available but are inconvenient for use in calculations with large number of repetitions. An empirical approximation for the Mott cross section was proposed by Browning [139, 140].

$$\sigma_{el} = \frac{(3e-18)Z^{1.7}}{E + 0.005Z^{1.7}E^{0.5} + 0.0007\frac{Z^2}{E^{0.5}}}[cm^2] \qquad \text{C.7}$$

To compute the inelastic mean free path and energy lost for the primary electrons the Fast Secondary Electron (FSE) model is used. FSE model assumes that secondary electrons are produced only by a knock-on collision with a free electron. The classical Coulomb differential cross section $\frac{d\sigma}{d\Omega}$ is employed to describe this process [76].

$$\frac{d\sigma}{d\Omega} = \frac{\pi e^4}{E^2}\left(\frac{1}{\Omega^2} + \frac{1}{(1-\Omega)^2}\right) \qquad \text{C.8}$$

Where E is the primary electron energy and Ω is the energy transfer to the secondary electron ΔE normalized by E. The deflection angle α of the primary electron of energy E (in keV) is computed as [76]:

$$\sin^2\alpha = \frac{2\Omega}{(2+(1-\Omega)\frac{E}{511})} \qquad \text{C.9}$$

The azimuth scattering angle γ of the generated secondary electron with respect to the incident electron direction is computed as [76]:

$$\sin^2\gamma = \frac{2(1-\Omega)}{(2+\Omega\frac{E}{511})} \qquad \text{C.10}$$

101 EMBED Equation.DSMT4

Generated secondary electrons with energies below 100 eV are assumed to scatter isotropically and the azimuth scattering angle γ equals:

$$\cos\gamma = 2R - 1 \qquad \text{C.11}$$

It is assumed that the polar scattering angle for the generated secondary electrons is independent of energy and equals $2\pi R$.

The normalized energy lost by the PE in collision is computed by solving the following equation [76]:

$$R = \frac{\int_{\Omega_c}^{\Omega}\left(\frac{d\sigma}{d\Omega}\right)d\Omega}{\int_{\Omega_c}^{0.5}\left(\frac{d\sigma}{d\Omega}\right)d\Omega} \rightarrow \Omega = \frac{1}{1000\text{-}998R} \qquad \text{C.12}$$

where the energy lost by the incident electron is $E\Omega$.

The inelastic mean free path, λ_{in} ,depends on material properties and on the electron energy. Only a few analytical expressions are available and the experimental data is often limited to a few keV range. Seah and Dench [142] proposed empirical formulas valid between 1-10,000eV, which is used in this work.

$$\lambda_{in} = a_0 \left(\frac{C_1}{(E - E_f)^2} + C_2 (a_0 (E - E_f))^{0.5} \right) \text{ (nm)}$$
$$a_0 = 10^9 \left(\frac{A_{mol}}{n_A \rho N_A} \right)^{1/3} \text{ (nm)} \qquad \text{C.13}$$

For calculations of λ_{in} for high energy primary electrons an expression is taken from Joy [76]:

$$\lambda_{in} = \frac{0.255 N_a E^2 A}{\rho Z} \text{ (nm)} \qquad \text{C.14}$$

Secondary electron transport is treated using the Straight Line Approximation (SLA). In this approximation, scattering of the low energy secondary electrons is neglected by assuming that the secondary electron travels in a straight line from the point of generation. The probability of a SE traveling distance z to reach the surface is:

$$p_{absorption} = e^{-z/IMFP} \qquad \text{C.15}$$

In case before it reaches the surface, a secondary electron has to pass through multiple zones, the individual zone lengths (r_i) and corresponding inelastic mean free paths (λ_i) are taken into account in calculating the absorption probability in the following way:

$$p_{absorption} = \prod_{i=1} p_i = \prod_{i=1} e^{-\frac{r_i}{\lambda_i}} = e^{-\sum_{i=1} \frac{r_i}{\lambda_i}} \qquad \text{C.16}$$

For secondary electrons, the energy changes associated with passing boundary between two materials were taken into account using the approach outlined by Yue et al. [78]. Specifically, when a secondary electron passes a boundary between materials A and B, with corresponding Fermi Energies of E_A and E_B, the difference E_A-E_B is added to the electron's energy.

Once at the surface, the generated secondary electron has to overcome the surface barrier in order to escape into vacuum. Specifically, the electron energy has to be greater than the sum of the material work

function and the Fermi energy [38]. Probability that an electron will escape surface barrier is [38]:

$$p(E) = 1 - \sqrt{\frac{E_F + \phi}{E}} \qquad \text{C.17}$$

For a typical secondary electron with energy below 50eV the average p(E) is about 0.1, implying a reflection coefficient of 0.9 at the metal-vacuum interface [143]. Thus, only a small fraction of the generated secondary electrons escapes into vacuum. It is instructive to note that the escape depth (into the material below its surface) is on the order of a few nanometers for most of the materials, while the penetration depth of PE can be on the order of several micrometers for higher energy electrons.

C.3. Geometric Relations

In order to correctly trace each electron from one collision to another its direction has to be transformed by the new polar and azimuthal scattering angles. The direction an electron moves is described by directional cosines in a fixed three-dimensional coordinate system. The geometrical representation of the system is shown in Figure C.2.

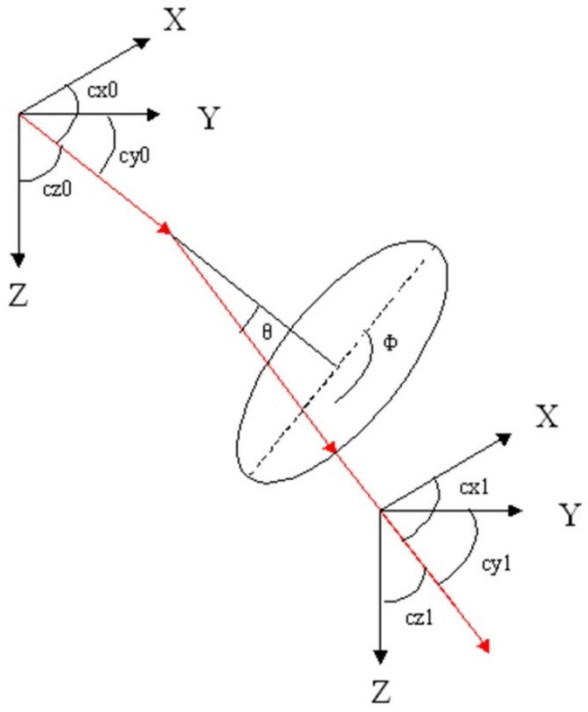

Figure C.2. Schematic of three dimensional electron tracing.

$$
\begin{aligned}
cx_1 &= cx_0\cos\theta + V_1V_2 + cy_0V_2V_4 & V_3 &= \cos\phi \\
cy_1 &= cy_0\cos\theta + V_4(cz_0V_1 - cx_0V_2) & V_4 &= \sin\phi \\
cz_1 &= cz_0\cos\theta + V_2V_3 - cy_0V_1V_4 & AN &= -\frac{cx_0}{cz_0} \\
V_1 &= AN\sin\theta & & \\
V_2 &= ANAM\sin\theta & AM &= \frac{1}{\sqrt{1+ANAM}}
\end{aligned}
\qquad \text{C.18}
$$

After each collision the new directional cosines (cx_1, cy_1, and cz_1) based on the scattering angles θ and ϕ are calculated according to Equation C.18.

C.4. Random Number Generator

Validity of a Monte Carlo simulation is based on the randomness of the pseudorandom number generator used. The Mersenne Twister (MT) pseudorandom number generator was utilized in this work. The MT is a twisted Generalized Fast Shift Register (GFSR) pseudorandom number generator. The period of MT is $2^{19937} - 1$, it has a 623 dimensional equidistribution with 32 bit accuracy, and consumes 624 words of working area. In contrast, the RAND() function in C has a period of 2^{31} and consumes 1 word of the working area. The MT has a CPU-time of 9.64 s while the MT has a CPU-time of 10.18 s for generation of 10^7 numbers. In summary, the MT algorithm takes up more memory and is slower, but produces a better quality array or random numbers than the RAND() function. Makoto Matsumoto and Takuji Nishimura C++ MT code available, at http://www.math.sci.hiroshima-u.ac.jp/~m-mat/MT/emt.html, is used in simulations.

C.4. MC Simulation program

Flow chart of MC reactive electron flux computation program for a single material target is shown in Figure C.3. Scattering within targets consisting of two or three (two top cases in the insert in Figure C.3) materials are based on the single scattering algorithm with one or two more scattering options available. The "electron scattering trees" for these algorithms are presented in Figure C.3 but the corresponding flow charts will not be presented.

At the beginning of the simulation the geometry of the deposit, defined by a set of numbered triangular

faces, is imported from a text file (see Appendix D). Since the geometry defined within FLUENT has one line of symmetry, but the MC simulation is fully three-dimensional, the mirror geometry is created. At the end of the simulation the results for the two symmetric sides are averaged. In simulations, each electron is traced individually.

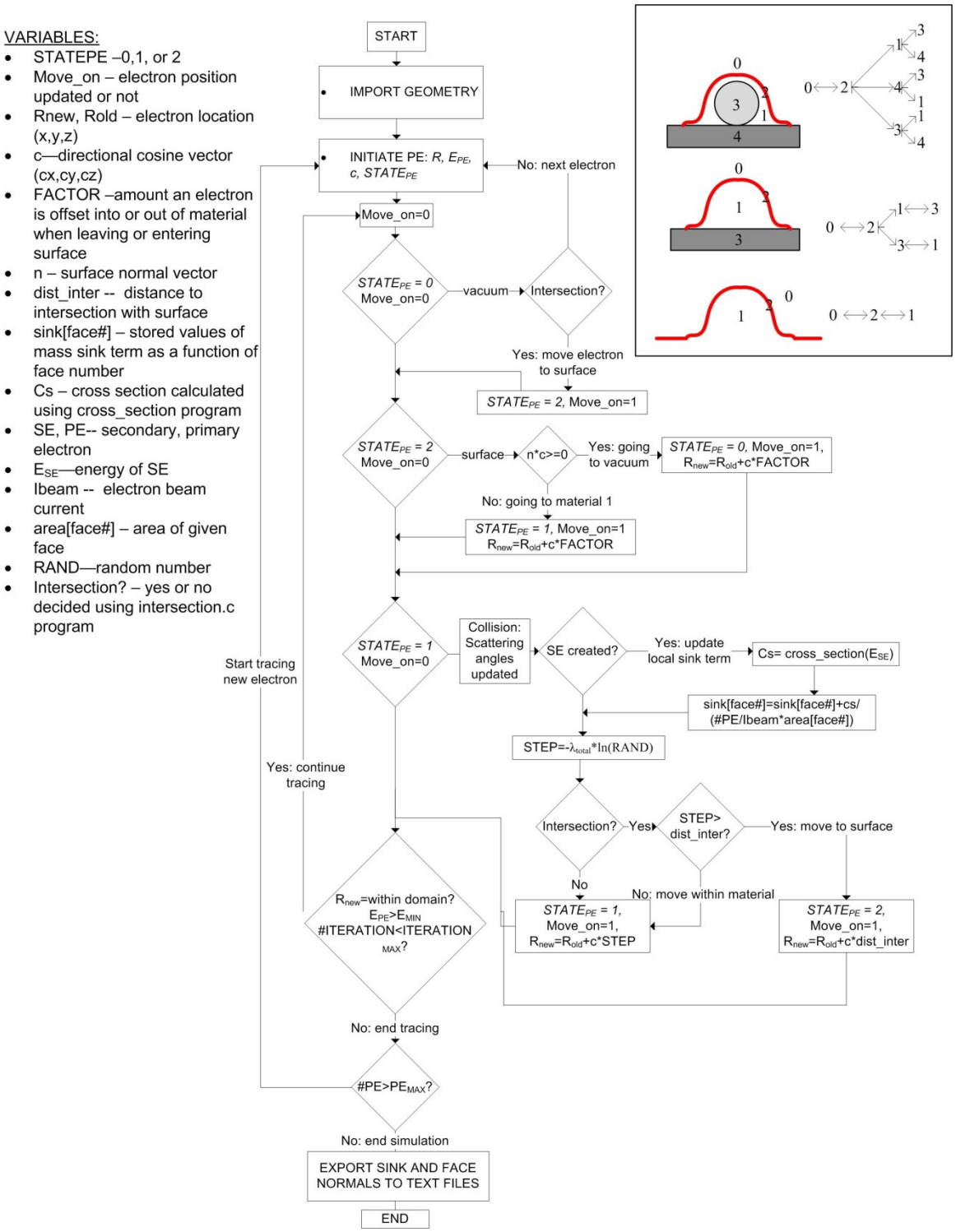

Figure C.3. Flow chart for DSMC mass sink term computation of a single material target. Inset in the top right schematically shows the possible electron scattering zones (0=vacuum, 1=amorphous carbon, 2=surface, and in more complex system 3=MWNT and 4=substrate).

Initially each electron has energy equal to that of the primary electron beam, travels in vertical direction (cz=1 in Figure C.3) and is positioned at the x-y plane with x and y position specified by a random number sampled from a gaussian distribution with standard deviation corresponding to the FWHM theoretical diameter of the electron beam. Next, the electron scattering trajectory is traced until it leaves the simulation domain, looses most of its energy or has a more than a set number of collisions. Ray tracing algorithm is used for computation of the distance to intersection of a specific face and the projected electron path. Specifically, during each step intersection of the given electron path with an infinite plane defined by each face is computed. If the intersection point lies within the region defined by the corners of the face the distance to the intersection is stored. In case of multiple intersections with the surface the shortest distance is picked. The electron travels in a straight line in vacuum until it reaches a surface or leaves the simulation domain. When within the target material (amorphous carbon for example), the electron undergoes elastic and inelastic collisions and travels with a linear trajectory in between these events. If a secondary electron generated within an inelastic collision has the right direction and sufficient energy to reach the surface and overcome the surface barrier, the cross section corresponding electron energy is added to the reactive electron flux at the specific face number. Between the scattering events within the medium and traveling in vacuum, the electron is in a "surface state". If entering (leaving) the material, the electron is moved slightly into (out) of the surface state. When tracing of all primary electrons is concluded, the computed mass sink term for each of the grid faces is exported into a text file and later utilized by FLUENT.

C.5. Number of primary electrons necessary for simulation

The number of simulated primary electrons has a strong influence on the resulting reactive electron flux distribution. As shown in Figure C.4, simulating too few primary electrons impinging vertically on a flat target produces a skewed and non-symmetric reactive electron flux spatial distribution. Naturally, a denser grid requires a higher number of simulated primary electrons to achieve "electron independent" results. As shown in Figure C.4, simulating 500,000 primary electrons is sufficient for achieving "electron independent" results for an electron beam with radius of 25 nm impinging on an uniform (not graded) grid

with ~2 nm length scale.

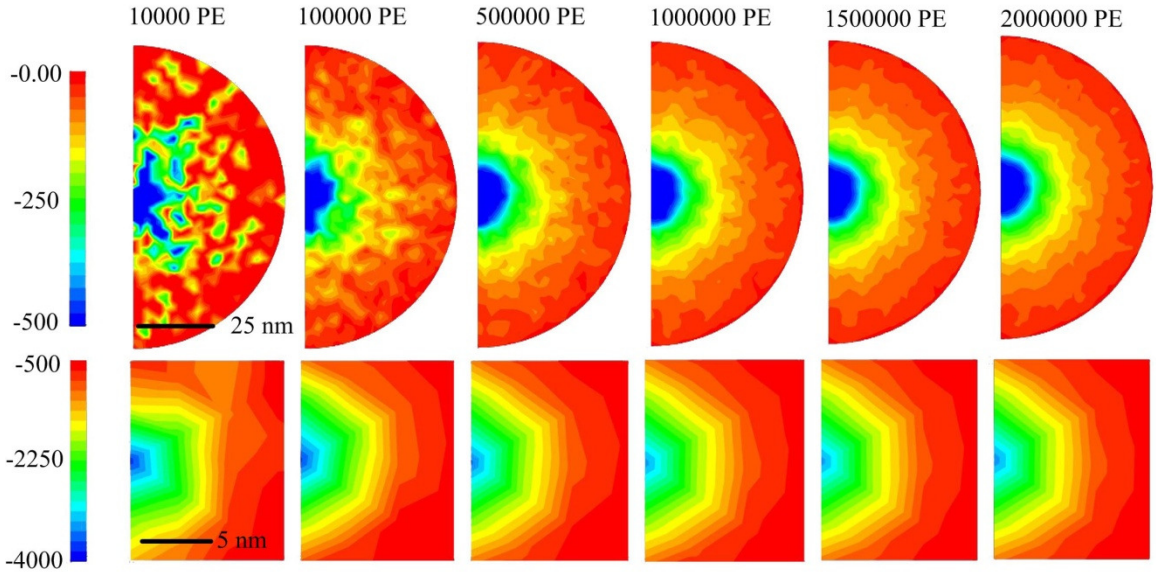

Figure C.4. Mass sink term spatial distribution resulting from simulation of different number of primary electrons of an electron beam with radius of 25 nm, energy of 25 keV, and current of 100 pA impinging on a flat carbon substrate with a model mesh scale of 2 nm.

It is important to note that utilization of a uniform mesh is preferred. Utilization of a graded mesh and not simulating a sufficient number of electrons can result in an incorrect distribution of the reactive electron flux.

C.6. Fitting parameters for Ionization and Dissocation Cross Sections

Table C.1 lists fitting parameters for electron induced dissociation cross section (Equation 2.11) and electron induced ionization cross section (Equation 2.12) for C_4H_6.

Table C.1. Constants and fitting parameters dissociation and ionization cross sections.

A_1	11326.9	E_{th}, eV	10
A_2	3014.6	E_{max}, eV	25
A_3	93.850	σ_{max},nm^2	0.087
A_4	-7121.8	λ,eV	77
A_5	-458.57		

APPENDIX D: NUMERICAL IMPLEMENTATION OF EBID OF RESIDUAL

HYDROCARBONS' MODEL

D.1. Axisymmetric Surface Transport Equation

The general flow chart of the transient simulation is shown in Figure D.1. The inputs into the program are the shape of the deposit (r and z vectors) and precursor concentration C, as well as properties of the electron beam such as current, full width at 50% of the beam, energy and time of simulation. Physical (material) properties of the substrate and deposit, size of the simulated region and surface properties such as surface diffusion coefficient are also the input parameters. At each time step, a variable size grid is generated over the given deposit curve producing discretization along the arc-length coordinate s. The r, z, s and ds/dr data for each new node are computed using linear interpolation between nodes from the grid at the previous time moment.

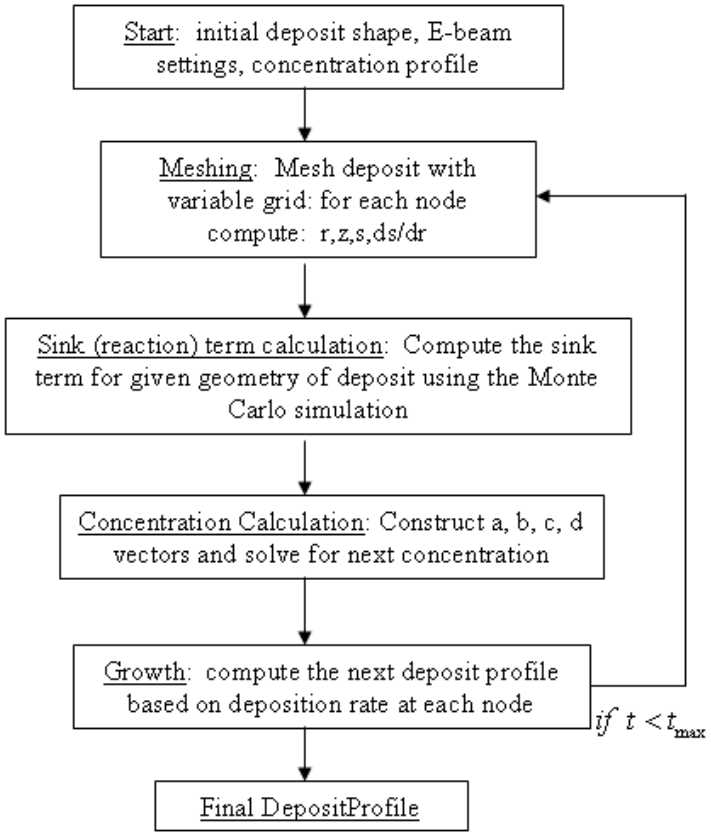

Figure D.1. Flow chart of the transient deposit growth simulation [41].

Next, the reactive electron flux term is computed by running a time-averaged Monte Carlo simulation of the primary electron scattering and secondary electron generation coupled with the dissociation cross sections for the adsorbed hydrocarbon species. The computation time and space averaged local mass sink term is a function of geometry of the substrate and of the growing deposit obtained from the previous time step. By taking this observation into account the simulation procedure was optimized by performing time-intensive Monte Carlo simulations of the reactive electron flux term not for every time step, but only when the deposit shape changes significantly. It should be noted that the reactive electron flux term needs to be updated more frequently in the case of the reaction-limited growth, and seldom in the case of the diffusion-limited process. Next the new surface concentration for the given time step is computed by numerically solving the surface transport equation. The computed mass sink term and local surface concentration are used to obtain a node specific mass deposition rate. Specific growth distance in units of *nm* at each node (normal to the surface of the deposit) is calculated according to:

$$\Delta h_{ring,i} = \frac{\Delta V_{ring,i}}{A_{ring,i}} = \frac{A_{ring,i} C_i \dot{Q}_{s_i}"\Delta t}{\rho A_{ring,i}} = \frac{C_i \dot{Q}_{s_i}"\Delta t}{\rho} \qquad \text{D.1}$$

Where $\Delta V_{ring,i}$ is the volumetric deposition rate in nm^3 at the *i*-th node, $A_{ring,i}$ is the area of the *i*-th ring in nm^2 (Figure 2.2), ρ is the molecular density of the solid deposit material in units of $molecules/nm^3$, and C_i is the surface concentration at the *i*-th node in units of $molecules/nm^2$. Taking into account the small growth during each time step the area of the deposition ring is assumed constant and taken at the previous time step. The direction of the growth at the i^{th} node is assumed to be normal to the segment connecting the adjacent nodes. If the simulation time does not reach the preset total simulation time the new (updated) *r, z, and C* values are passed back into the meshing and interpolation steps to proceed forward in time. The shapes of the deposit and concentration profiles at each time step are saved into a text file for post-processing.

D.2. Generalized STE

D.2.1. Program Overview

The generalized STE model described in Chapter 2 is implemented in FLUENT simulation environment. The Monte Carlo (MC) simulation of electron transport and generation is written as a separate C++ application and is coupled with the FLUENT mass transport and growth simulation (see Appendix C). The deposit geometry is periodically remeshed using GAMBIT program. The flow chart for the main simulation program is shown in Figure D.2.

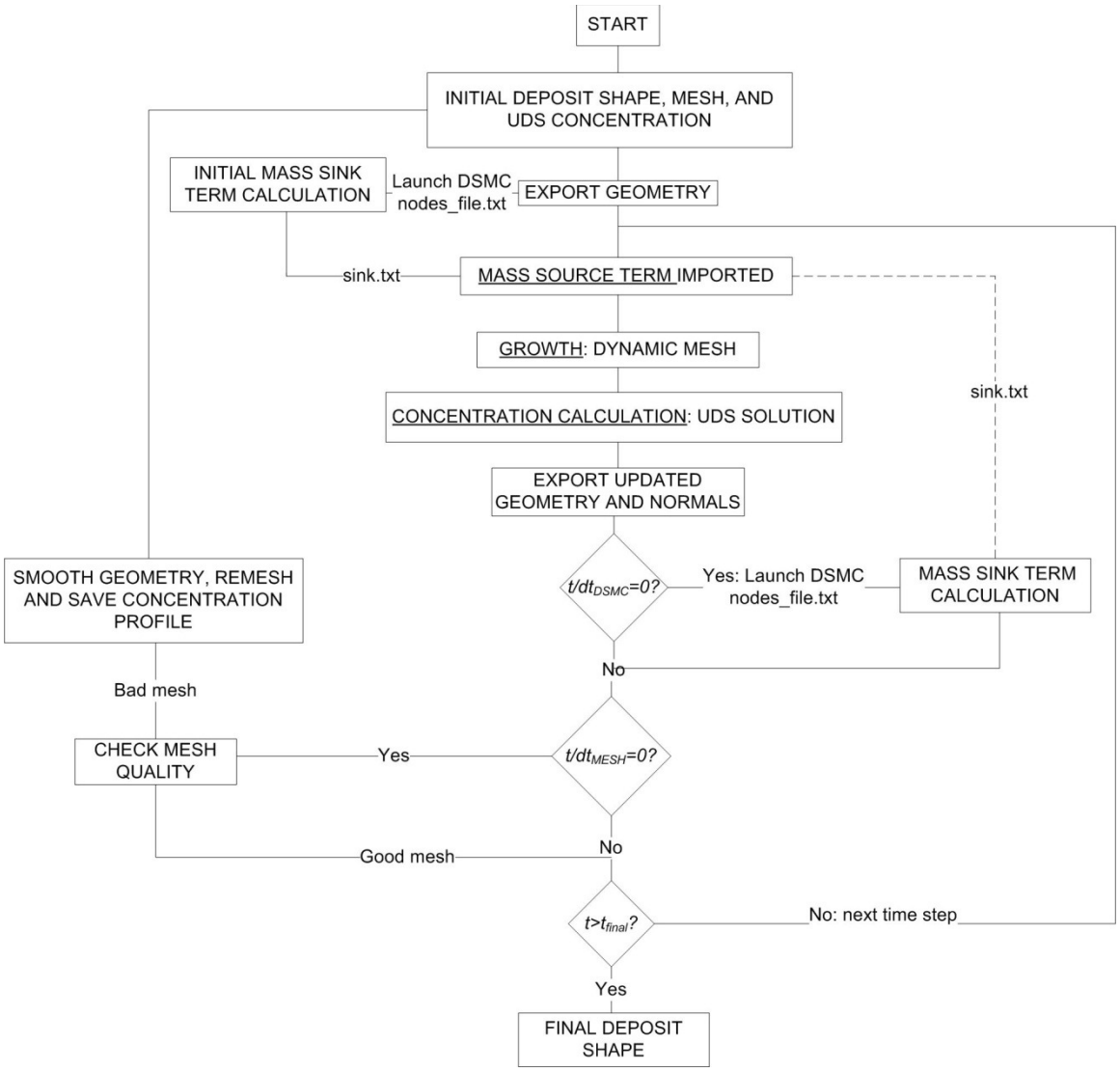

Figure D.2. The main simulation program flow chart.

The Surface Transport Equation (Equation 2.5) is numerically solved using a modified three-

dimensional general transport equation for a User Defined Scalar (UDS) confined to a thin shell volume. The inputs into the simulation are the meshed deposit geometry with specified initial and boundary conditions for the surface concentration. Next the input geometrical information is exported into a text files (number_of_faces.txt, nodes_file.txt, and normals.txt) and an external MC application is launched using the DEFINE_EXECUTE_ON_LOADING User Defined Function (UDF) macro. The MC application computes the reactive electron flux for each face/cell and saves the results into sink.txt file. FLUENT waits until the MC application operation is completed and imports the cell specific reactive electron flux using the DEFINE_SOURCE UDF macro. Cell specific mass sink/source term is computed by multiplying the reactive electron flux by the precursor concentration. The incremental growth for the current time step for each node within the mesh is computed based on area weighted average of the product of cell specific concentration and reactive electron for the neighboring cells. The growth of the mesh is controlled using the DEFINED_GRID_MOTION dynamic mesh UDF macro. Next, the UDS concentration profile is updated for the next time step. At the end of each time step iteration the updated geometrical information is exported into text files. The MC application is launched every n_{dsmc} time steps and the geometry is exported and remeshed every n_{remesh} time steps. Every remeshing operation requires a new FLUENT session. The details of each of the simulation steps and selection of related settings is described in the following sub-sections.

D.2.2. UDS simulation and model geometry

The transient three-dimensional transport equation for UDS φ is discretized using Finite Volume Method and solved within FLUENT. For each individual cell, FLUENT solves the following equation:

$$\frac{\partial \rho \phi}{\partial t} V = \sum_{f}^{N_{faces}} D_{\phi} \nabla \phi_f \cdot \vec{A}_f + S_{\phi} V \qquad \text{D.2}$$

Where $\nabla \phi_f$ is the gradient, D_{ϕ} is the diffusion coefficient, S_{ϕ} is the mass source term, and ρ is the density of the scalar quantity ϕ, V and $\vec{A}_f$ are the volume and face area vector of each cell, respectively. When the solution is confined to a constant height thin shell with zero flux boundary conditions on top and

bottom face and ρ is unity, Equation D.2 reduces to the height independent Equation D.3:

$$\frac{\partial \phi}{\partial t} A = \sum_{f}^{N_{edges}} D_{\phi} \nabla \phi \cdot \vec{L}_f + S_{\phi} A \qquad \text{D.3}$$

Where $\vec{L}_f$ is the length of each edge and A is the area of the given face. Figure D.3 shows the top view (x-y) view of the simulation domain and a schematic representing an individual thin shell wedge cell with appropriate boundary conditions of the dimensionless concentration C^* (UDS scalar ϕ) .

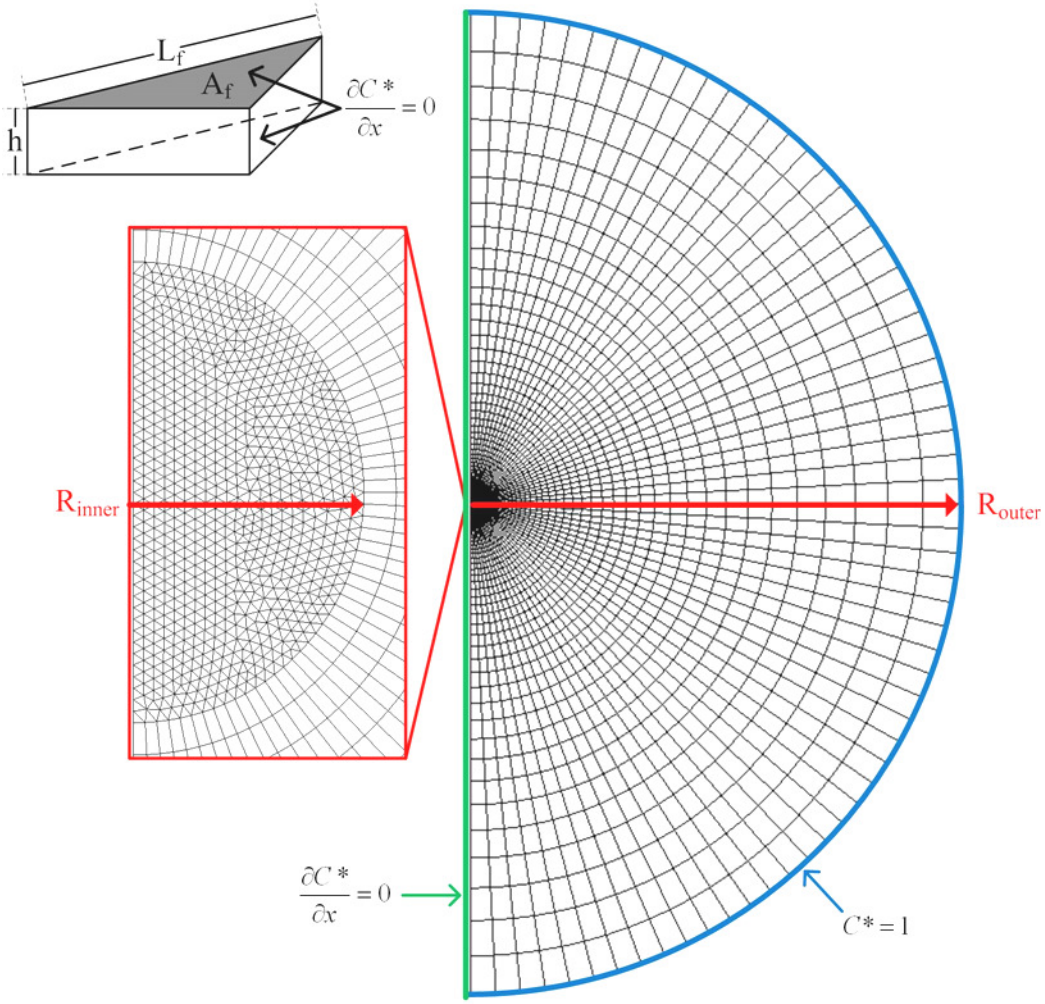

Figure D.3. Top view of the meshed simulation domain and three-dimensional view of an individual thin shell wedge cell with appropriate boundary conditions for the dimensionless concentration C*.

To confirm the height (h in Figure D.3) independence of the solution, results for three different shell thicknesses were compared. Figure D.3 shows the dimensionless concentration C^* in the center of the

deposition zone as a function of time for *h* equal to 1 nm, 0.1 nm and 0.01 nm. As expected, the solution does not depend on the thickness of the shell.

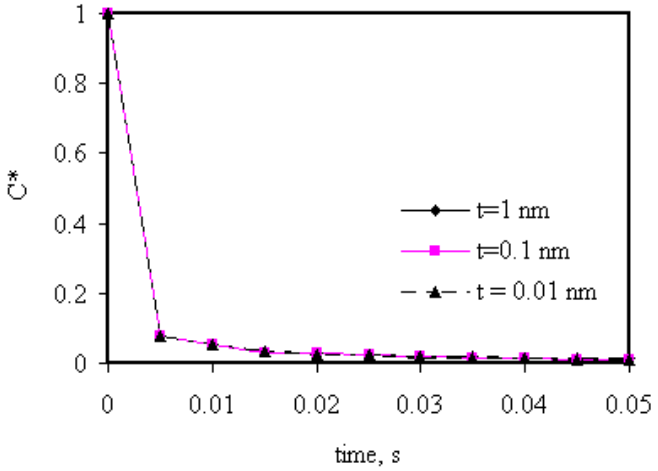

Figure D.4. Dimensionless surface concentration, C*, versus time for three different shell thicknesses.

As shown in Figure D.2, the simulated domain is divided into two zones with radiuses of R_{inner} and R_{outer}. The inner zone is densely meshed with fine wedge cells, while the outer zone was meshed with a coarse hexahedron mesh. The electron transport and generation simulation, source term computation, and growth of the deposit are confined to the inner region. The influence of the value of R_{inner} on the electron transport and generation and *C** simulation results is investigated. Results for electron beam with radius of 25 nm, accelerating voltage of 25 kV, and current of 100 pA, impinging in the center of the inner region at a surface with initially *C**=1 are shown in Figures D.5 and D.6.

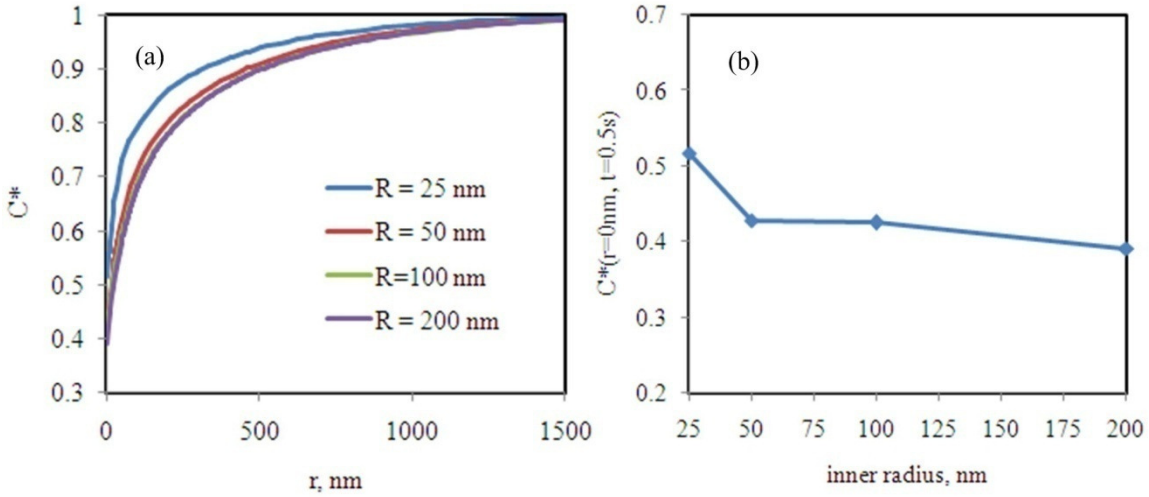

Figure D.5. Influence of the inner radius (R) on the precursor concentration C* simulation results.

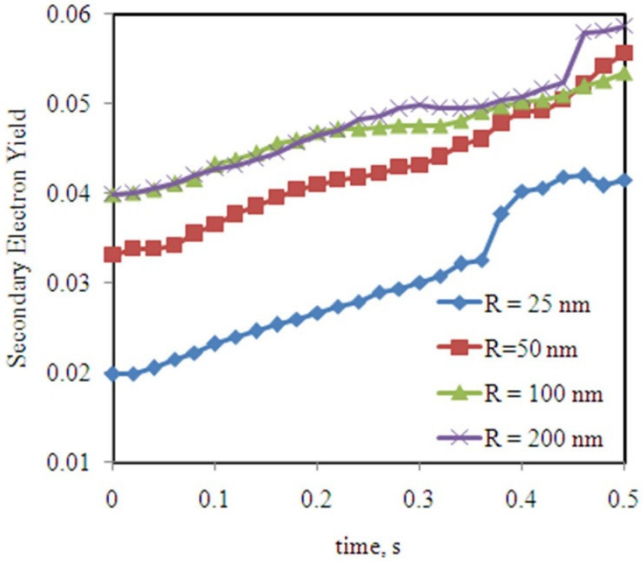

Figure D.6. Influence of the inner radius (R) on secondary electron yield time evolution.

The results are not impacted if the value of R_{inner} equal to and beyond 50 nm. As a general rule, the value of R_{inner} must be set to 2-3 times that of the electron beam. The mesh information is exported at beginning of each FLUENT session and after each time step using either the DEFINE_ON_LOADING or DEFINE_EXECUTE_AT_END UDF macro.

D.2.3. Growth and dynamic mesh simulation

The computed reactive electron flux and local surface concentration are used to obtain a node specific growth rate. For each node, the specific growth in units of nm is computed using the area-weighted average of the product of the cell residual hydrocarbon concentration, mass sink term, and density of the deposited material:

$$\Delta h_k = \sum_{i=1}^{N_{neighbors}} \frac{A_i}{\sum_{i=1}^{N_{neighbors}} A_i} \frac{\Delta V_i}{A_i} = \sum_{i=1}^{N_{neighbors}} \frac{A_i}{\sum_{i=1}^{N_{neighbors}} A_i} \frac{A_i C_i \dot{Q}_{s_i} \Delta t}{\rho A_i} = \sum_{i=1}^{N_{neighbors}} \frac{A_i}{\sum_{i=1}^{N_{neighbors}} A_i} \frac{C_i \dot{Q}_{s_i} \Delta t}{\rho} \qquad \text{D.4}$$

Where ΔV_i is the volumetric deposition rate in nm^3 at the i-th face, A_i is the area of the i-th face in nm^2, ρ is the molecular density of the solid deposit material in units of $molecules/nm^3$, and C_i is the surface concentration at the i-th face in units of molecules/nm^3. Figure D.7 shows a schematic representation of the neighboring face contribution towards the growth of node k.

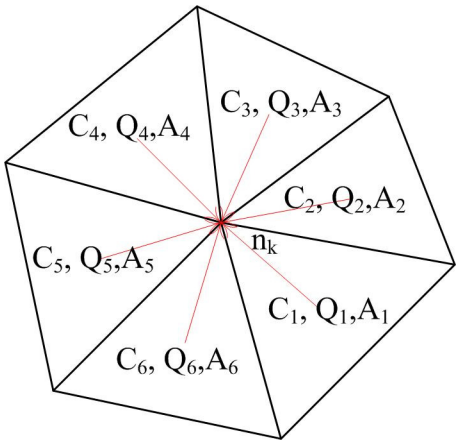

Figure D.7. Schematical representation of contribution of neighboring faces to growth of node k.

As shown in Equation D.7, the growth of node k directly depends on the reactive electron flux computed for the neighboring faces. The reactive electron flux is computed according to Equation 2.13 and is proportional to the flux of electrons passing through the given face. The flux of the electrons emerging from the substrate increases sharply near the center of the beam. While the mass transport simulation is not significantly impacted by the grid size (because the source term is multiplied by the area of the face), the growth of each node depends on the proper capturing of the flux distribution. As shown in Figure D.8, a

coarse mesh leads to a decreased growth rate in the center of the deposit. A very fine (Figure D.8b) mesh scale is required in order to capture the growth dynamics correctly. However, as shown in Figure D.9, the CPU time required per FLUENT iteration and simulation of 1000 electrons increases drastically with decreasing mesh scale. Without parallel computation the required CPU times for grid-independent solution are difficult to achieve. For computational efficiency a mesh scale of 2 nm and 5 nm is used in simulation in this thesis. This implies that the resulting growth rate is not quantitatively accurate and the resulting time evolution of the geometry is only qualitatively predictive.

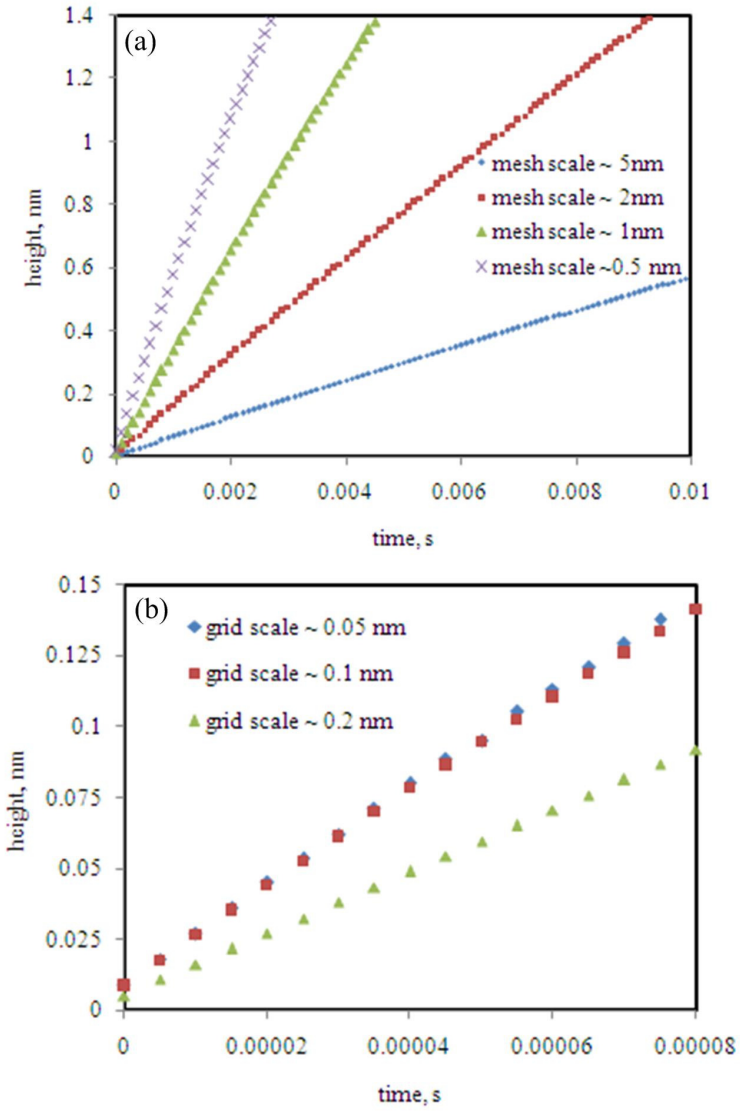

Figure D.8. Impact of mesh scale on the height of the center of the deposit.

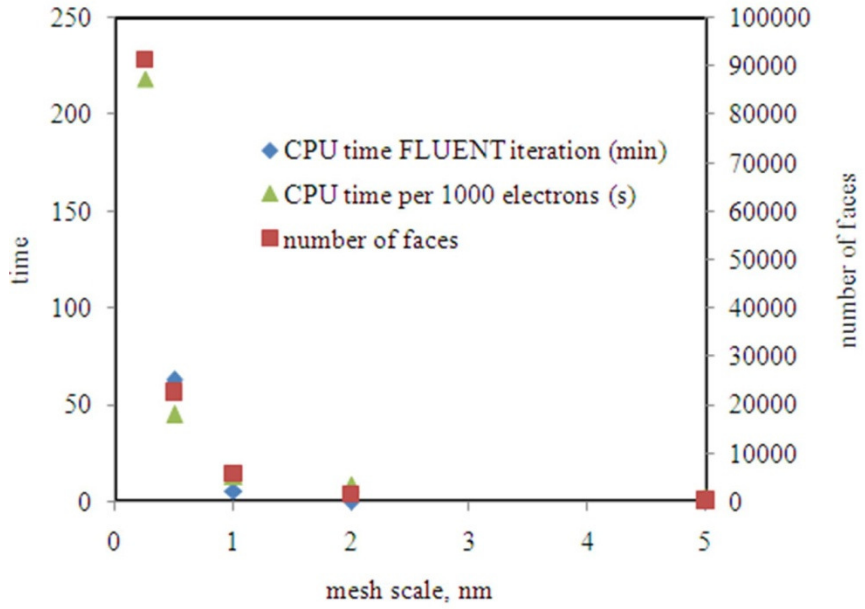

Figure D.9. Number of faces for an uniform triangular grid with different uniform mesh scales within a half circle of radius 50 nm, and CPU time required for one FLUENT iteration and simulation of 1000 electrons for the given mesh scales.

D.2.4. Remeshing of the model

Large deformations of the geometry require a periodical update of the model mesh. Several different methods for remeshing and smoothing of the geometry are tested. First FLUENTs Laplacian smoothing of the dynamic mesh is tested. Each node position is computed as follows:

$$\overline{\vec{x}_i^{\,m}} = \frac{\sum_j^{n_i} \vec{x}_j^{\,m}}{n_i} \qquad \text{D.5}$$

Where $\overline{\vec{x}_i^{\,m}}$ is the averaged node position of node i at iteration m, $\vec{x}_j^{\,m}$ is the node position of neighbor node of $\vec{x}_i^{\,m}$ at iteration m, and n_i is the number nodes neighboring node i. The new node position $\vec{x}_i^{\,m+1}$ is then computed as follows:

$$\vec{x}_i^{\,m+1} = \vec{x}_i^{\,m}(1-\beta) + \overline{\vec{x}_i^{\,m}}\beta \qquad \text{D.6}$$

Where β is the boundary node relaxation factor. Figure D.10 shows the impact of Laplacian smoothing with β= 0.7 with each iteration on the center height of the deposit. Only the time step and thus the number

of times the Laplacian smoothing is performed is varied. Due to the significant impact of the smoothing on the resulting geometry this method is not appropriate.

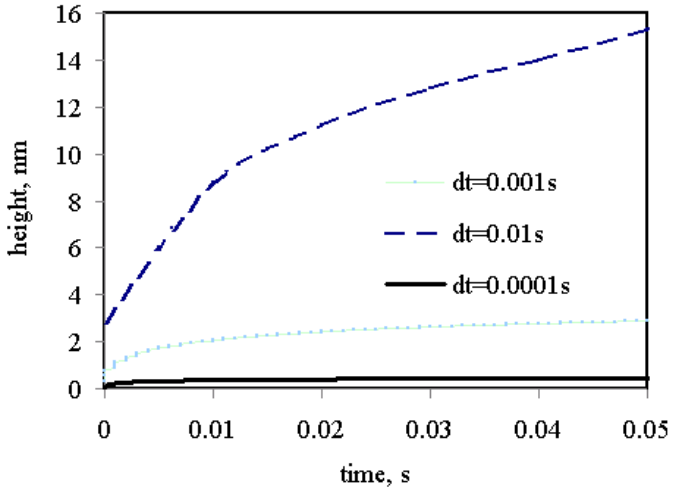

Figure D.10. Center height of the deposit versus time for different time steps with application of Laplacian smoothing with β=0.7.

Volumetric and face remeshing options within FLUENT are also tested. Unfortunately, both of the methods are not robust in three-dimensions and therefore are not applied either.

Manual remeshing of the geometry produces the best results. The mesh is periodically exported out of FLUENT into GAMBIT and remeshed (see Figure D.11). The corresponding surface concentration distribution is exported out of FLUENT and used as an initial condition for the next FLUENT simulation with the remeshed model. Concentration values for the new mesh are calculated by interpolating between the old mesh values and are implemented as an initial condition using the DEFINE_INIT UDF macro.

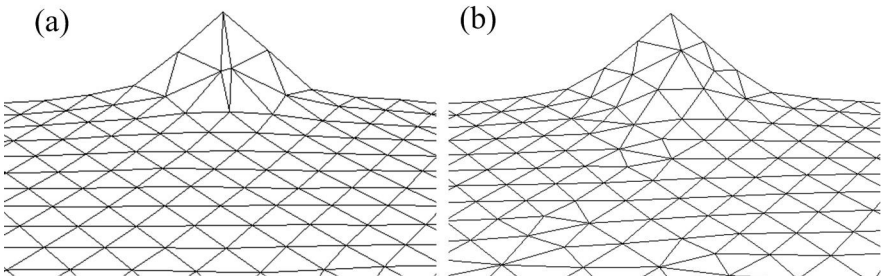

Figure D.11. Example of a mesh (a) before and (b) after remeshing in GAMBIT.

D.2.5. Iteration, reactive electron flux updating, and remeshing time steps

Time steps for iteration, source term updating, and remeshing are investigated. Figure D.12 shows the height of the deposit and dimensionless concentration at the center of the deposition zone for two different time steps. A time step of 0.001s was found to be sufficient for correctly capturing of the concentration and height time evolution with a mesh scale of 2 nm.

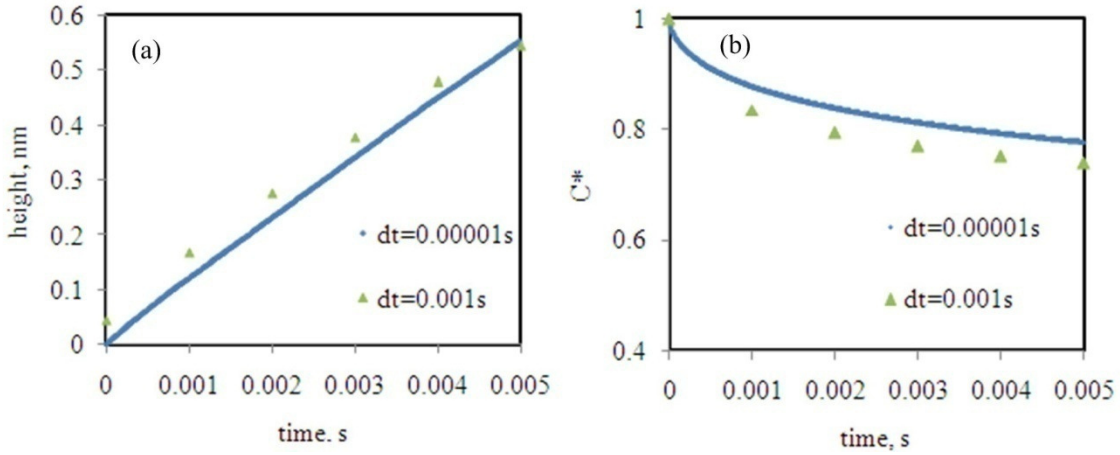

Figure D.12. (a) Height versus time and (b) Dimensionless Concentration, C*, versus time at the center of the deposition zone for two different time steps for geometry with a mesh scale of 2 nm.

Next, the frequency of updating the reactive electron flux is investigated. Figure D.13 shows height of the deposit and dimensionless concentration at the center of the deposition zone and secondary electron yield as a function of time for different reactive electron flux update frequency. Updating the reactive electron flux every 0.0125 s produces similar results as updating the mass sink term every 0.00625 seconds, and is utilized in all simulations.

The frequency of remeshing the model depends on the extent of the deformation of the mesh, which varies during the simulation. Selecting a fixed time step for updating the mesh is difficult and the mesh is updated at different time steps during different stages of deposit growth. As a simple rule of thumb remeshing is performed when the local deformed mesh scale is double of that of the initial mesh scale.

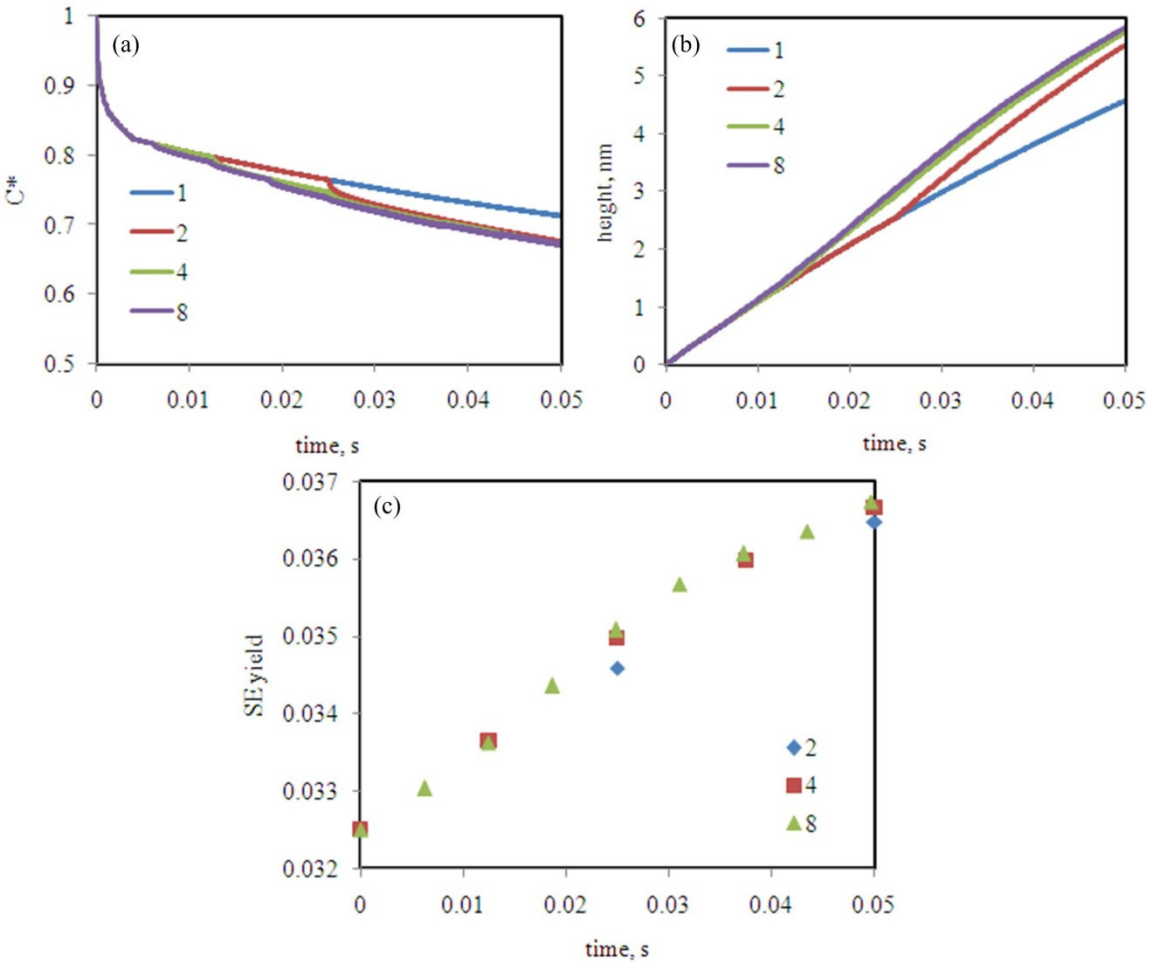

Figure D.13. (a) Height versus time, (b) Dimensionless Concentration, C*, versus time at the center of the deposition zone, and (c) Secondary electron yield versus time for different mass sink term update frequency.

APPENDIX E: ELECTRO-THERMAL SIMULATION

The temperature rise due to Joule heating of the interconnect is simulated using Finite Element Method and solved using ANSYS. A half sphere connected to a cylinder is used to represent a simplified geometry of the EBID carbon contact-MWNT assembly (Figure E.1).

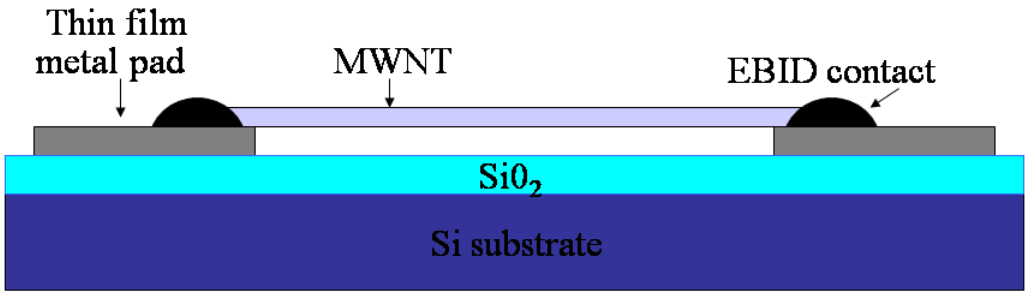

Figure E.1. Schematic of the simplified MWNT interconnect geometry.

The solution is assumed to be symmetric about the center and axis of the MWNT. Thus only a quarter of the whole geometry is modeled. The MWNT is modeled as a solid cylinder with diameter of 30 nm and length of 10 μm while the deposit is modeled as a hemisphere with diameter of 100 nm. The metal electrode and $Si0_2$ layer are simulated as square pads with, 6000x100nm and 25000x1000nm dimensions, respectively. The volumes are meshed with element sizes based on five different line sizes, 5, 20, 100, 500, and 1000. The meshed geometry is shown in Figure E.2.

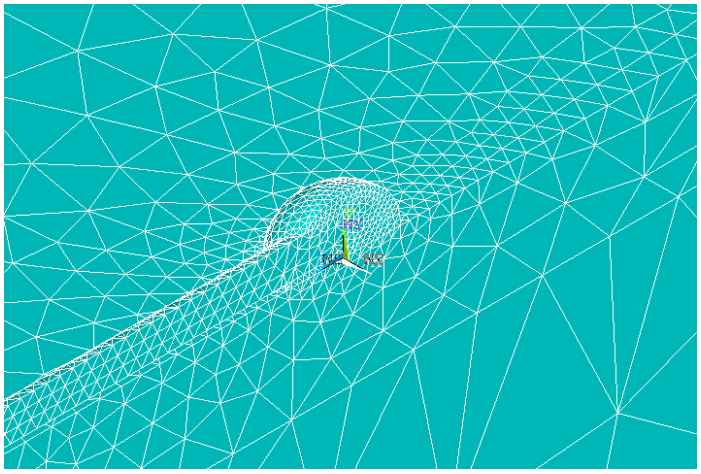

Figure E.2: Close up of the MWNT and carbon joint ANSYS mesh.

Two sets of EBID carbon joint material properties corresponding to unannealed amorphous carbon and to partially graphitized carbon are simulated. Table E.1 summarizes all material properties applied in the

simulation. Equivalent resistivity of the MWNT is calculated based on conduction through the outer shell of the tube only.

Table E. 1: Physical properties of the materials used in electro-thermal simulation.

Material	**Electrical Resistivity, Ω·nm**	**Thermal Conductivity, W/(nm·K)**	**Density,kg/nm^3**
MWNT	925	30e-7	2.2e-24
$Si0_2$	10e21	0.014e-7	2.2e-24
Amorphous Carbon (aC)	200	1e-9	2e-24
Partially Graphitized aC	5	4.7e-8	2.25e-24
Electrode (Copper)	16.7	1.434e-9	8.9e-24

A convective boundary is set to surfaces of the MWNT, carbon joint, and thin metal plate (ambient temperature of 300K and heat transfer coefficient of 5 W/mK). A constant temperature boundary condition of 300K is set on the bottom of the $Si0_2$ layer. The load conditions consist of an applied DC voltage across the interconnect. Loading of 0.1, 1, and 5 V was simulated. An example of the temperature distribution and resulting temperature rise within the carbon joints are shown in Figure E.3. As shown in Figure E.3, significant temperature rise (more than 100ºC) occurs with a loading higher than 1 V for both the amorphous carbon and partially graphitized joint cases. This result confirms that the decreases in interconnect resistivity is due to significant Joule heating induced partial graphitization of the MWNT-electrode carbon joint.

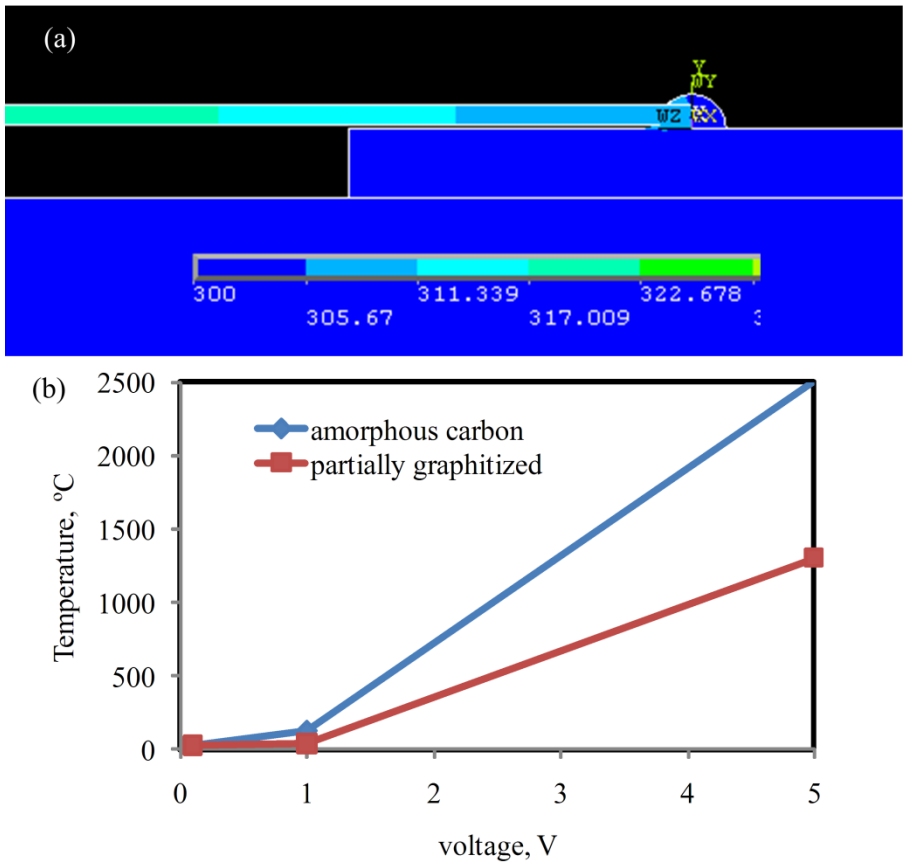

Figure E.3. (a) Example of temperature distribution within MWNT and carbon joint, and (b) Maximal temperature within the carbon joint for different applied voltages for amorphous carbon and partially graphitized deposits.

REFERENCES

1. Naeemi, A., R. Sarvari, and J.D. Meindl, *Performance comparison between carbon nanotube and copper interconnects for gigascale integration (GSI).* Ieee Electron Device Letters, 2005. **26**(2): p. 84-86.
2. Dong, L.F., et al., *Effects of local Joule heating on the reduction of contact resistance between carbon nanotubes and metal electrodes.* Journal of Applied Physics, 2007. **101**(2).
3. Anantram, M.P. and F. Leonard, *Physics of carbon nanotube electronic devices.* Reports on Progress in Physics, 2006. **69**(3): p. 507-561.
4. Graham, A.P., et al., *How do carbon nanotubes fit into the semiconductor roadmap?* Applied Physics a-Materials Science & Processing, 2005. **80**(6): p. 1141-1151.
5. Collins, P.G., et al., *Current saturation and electrical breakdown in multiwalled carbon nanotubes.* Physical Review Letters, 2001. **86**(14): p. 3128-3131.
6. Li, H., et al., *Circuit modeling and performance analysis of multi-walled carbon nanotube interconnects.* Ieee Transactions on Electron Devices, 2008. **55**(6): p. 1328-1337.
7. Close, G.F., et al., *A 1GHz Integrated Circuit with Carbon Nanotube Interconnects and Silicon Transistors.* Nano Letters, 2008. **8**(2): p. 706-709.
8. Kahng, Y.H., et al., *The role of an amorphous carbon layer on a multi-wall carbon nanotube attached atomic force microscope tip in making good electrical contact to a gold electrode.* Nanotechnology, 2008. **19**(19): p. 7.
9. Tersoff, J., *Contact resistance of carbon nanotubes.* Applied Physics Letters, 1999. **74**(15): p. 2122-2124.
10. Frank, S., et al., *Carbon nanotube quantum resistors.* Science, 1998. **280**(5370): p. 1744-1746.
11. Nihei, M., et al. *Low-resistance multi-walled carbon nanotube vias with parallel channel conduction of inner shells*. 2005. Burlingame, CA, United States: Institute of Electrical and Electronics Engineers Computer Society, Piscataway, NJ 08855-1331, United States.
12. Sato, S., et al. *Novel approach to fabricating carbon nanotube via interconnects using size-controlled catalyst nanoparticles*. 2006. Burlingame, CA, USA: IEEE.
13. Li, H.J., et al., *Multichannel ballistic transport in multiwall carbon nanotubes.* Physical Review Letters, 2005. **95**(8).
14. Langford, R.M., et al., *Comparison of different methods to contact to nanowires.* Journal of Vacuum Science & Technology B, 2006. **24**(5): p. 2306-2311.
15. Dockendorf, C.P.R., et al., *Individual carbon nanotube soldering with gold nanoink deposition.* Applied Physics Letters, 2007. **90**(19).
16. Bachtold, A., et al., *Contacting carbon nanotubes selectively with low-ohmic contacts for four-probe electric measurements.* Applied Physics Letters, 1998. **73**(2): p. 274-276.
17. Rice, P., et al., *Broadband electrical characterization of multiwalled carbon nanotubes and contacts.* Nano Letters, 2007. **7**(4): p. 1086-1090.
18. Bussolotti, F., et al., *In situ manipulation and electrical characterization of multiwalled carbon nanotubes by using nanomanipulators under scanning electron microscopy.* Physical Review B, 2007. **76**(12).
19. Molhave, K., et al., *Solid gold nanostructures fabricated by electron beam deposition.* Nano Letters, 2003. **3**(11): p. 1499-503.
20. Fedorov, A.G., K. Rykaczewski, and W.B. White, *Transport issues in focused electron beam chemical vapor deposition.* Surface & Coatings Technology, 2007. **201**(22-23): p. 8808-8812.
21. Ding, W., et al., *Mechanics of hydrogenated amorphous carbon deposits from electron-beam-induced deposition of a paraffin precursor.* Journal of Applied Physics, 2005. **98**(1).
22. Utke, I., P. Hoffmann, and J. Melngailis, *Gas-assisted focused electron beam and ion beam processing and fabrication.* Journal of Vacuum Science & Technology B, 2008. **26**(4): p. 1197-1276.
23. Ando, A., et al., *Improvement of electrical contact at carbon nanotube/Pt by selective electron irradiation.* Physica E-Low-Dimensional Systems & Nanostructures, 2004. **24**(1-2): p. 6-9.
24. Kiang, C.H., *Electron irradiation induced dimensional change in bismuth filled carbon nanotubes.* Carbon, 2000. **38**(11-12): p. 1699-1701.

25. Yu, M.F., et al., *Tensile loading of ropes of single wall carbon nanotubes and their mechanical properties.* Physical Review Letters, 2000. **84**(24): p. 5552-5555.
26. Yu, M.F., et al., *Three-dimensional manipulation of carbon nanotubes under a scanning electron microscope.* Nanotechnology, 1999. **10**(3): p. 244-252.
27. Dong, L.X., F. Arai, and T. Fukuda, *Electron-beam-induced deposition with carbon nanotube emitters.* Applied Physics Letters, 2002. **81**(10): p. 1919-1921.
28. Fukuda, T., F. Arai, and L.X. Dong, *Fabrication and property analysis of MWNT junctions through nanorobotic manipulations.* International Journal of Nonlinear Sciences and Numerical Simulation, 2002. **3**(3-4): p. 753-758.
29. Fukuda, T., F. Arai, and L.X. Dong, *Assembly of nanodevices with carbon nanotubes through nanorobotic manipulations.* Proceedings of the Ieee, 2003. **91**(11): p. 1803-1818.
30. Nakayama, Y., *Scanning probe microscopy installed with nanotube probes and nanotube tweezers.* Ultramicroscopy, 2002. **91**(1-4): p. 49-56.
31. Abe, H., et al., *Electric transport and mechanical strength measurements of carbon nanotubes in scanning electron microscope.* Physica E-Low-Dimensional Systems & Nanostructures, 2004. **24**(1-2): p. 42-45.
32. Wang, M.S., et al., *Fabrication and electrical and mechanical properties of carbon nanotube interconnections.* Advanced Functional Materials, 2005. **15**(11): p. 1825-1831.
33. Chen, Q., S. Wang, and L.M. Peng, *Establishing Ohmic contacts for in situ current-voltage characteristic measurements on a carbon nanotube inside the scanning electron microscope.* Nanotechnology, 2006. **17**(4): p. 1087-1098.
34. Yang, Q.H., et al., *Local reconstruction and controllable nanospot welding of multiwalled carbon nanotubes under mild electron beam irradiation.* Materials Letters, 2006. **60**(20): p. 2433-2437.
35. Dong, L.X., A. Subramanian, and B.J. Nelson, *Carbon nanotubes for nanorobotics.* Nano Today, 2007. **2**(6): p. 12-21.
36. Kaplan-Ashiri, I., et al., *Microscopic investigation of shear in multiwalled nanotube deformation.* Journal of Physical Chemistry C, 2007. **111**(24): p. 8432-8436.
37. Wei, D.C., et al., *Real time and in situ control of the gap size of nanoelectrodes for molecular devices.* Nano Letters, 2008. **8**(6): p. 1625-1630.
38. Silvis-Cividjian, N., *Electron Beam Induced Nanometer Scale Deposition*. 2002, University of Delft: Netherlands.
39. Rykaczewski, K., et al., *Dynamic growth of carbon nanopillars and microrings in electron beam induced dissociation of residual hydrocarbons.* Ultramicroscopy, 2008. **108**(9): p. 989-92.
40. Ueda, K. and M. Yoshimura, *Fabrication of nanofigures by focused electron beam-induced deposition.* Thin Solid Films, 2004(464-465): p. 331-334.
41. Rykaczewski, K., W.B. White, and A.G. Fedorov, *Analysis of Electron Beam Induced Deposition (EBID) of residual hydrocarbons in electron microscopy.* Journal of Applied Physics, 2007. **101**(5): p. 054307.
42. Madsen, D.N., et al., *Soldering of nanotubes onto microelectrodes.* Nano Letters, 2003. **3**(1): p. 47-49.
43. Gopal, V., et al., *Rapid prototyping of site-specific nanocontacts by electron and ion beam assisted direct-write nanolithography.* Nano Letters, 2004. **4**(11): p. 2059-2063.
44. Banhart, F., *The formation of a connection between carbon nanotubes in an electron beam.* Nano Letters, 2001. **1**(6): p. 329-332.
45. Mateiu, R., et al., *An approach to a multi-walled carbon nanotube based mass sensor.* Microelectronic Engineering, 2004. **73-74**: p. 670-674.
46. Molhave, K., et al., *Towards pick-and-place assembly of nanostructures.* Journal of Nanoscience and Nanotechnology, 2004. **4**(3): p. 279-282.
47. Molhave, K., et al., *Constructing, connecting and soldering nanostructures by environmental electron beam deposition.* Nanotechnology, 2004. **15**(8): p. 1047-1053.
48. Brintlinger, T., et al., *Electrodes for carbon nanotube devices by focused electron beam induced deposition of gold.* Journal of Vacuum Science & Technology B, 2005. **23**(6): p. 3174-3177.
49. Bauerdick, S., et al., *Direct wiring of carbon nanotubes for integration in nanoelectromechanical systems.* Journal of Vacuum Science & Technology B, 2006. **24**(6): p. 3144-3147.

50. Krasheninnikov, A.V. and F. Banhart, *Engineering of nanostructured carbon materials with electron or ion beams.* Nature Materials, 2007. **6**(10): p. 723-733.
51. Song, J.W., et al., *Characterization and air pressure sensing of doubly clamped multi-walled carbon nanotubes.* Nanotechnology, 2008. **19**(1): p. 4.
52. Subramanian, A., et al. *Micro and Nanorobotic Assembly Using Dielectrophoresis*. in *Robotics: Science and Systems I*. 2005. Massachusetts Institute of Technology, Cambridge, Massachusetts.
53. Cosslett, V.E., *Particle Growth in the Electron Microscope.* Journal of Applied Physics, 1947. **18**(9): p. 844-845.
54. Watson, J.H.L., *An Effect of Electron Bombardment Upon Carbon Black.* Journal of Applied Physics, 1947. **18**(2): p. 153-161.
55. Ellis, S.G., Paper read to Am. Electron Microscopy Soc. Washington, DC, November, 1951.
56. Ennos, A.E., *The Origin of Specimen Contamination in the Electron Microscope.* British Journal of Applied Physics, 1953. **4**(APR): p. 101-106.
57. Hart, R.K., T.F. Kassner, and J.K. Maurin, Philosophical Magazine 1969. **21**(170): p. 453-67.
58. Fourie, J.T., *Controlling Parameter in Contamination of Specimens in Electron-Microscopes.* Optik, 1975. **44**(1): p. 111-114.
59. Muller, K., *Elektronen mikroschreiber mit geschwindigkeitsgesteuerter strahlfurung. II.* Optik, 1971. **33**: p. 296.
60. Reimer, L. and M. Wachter, *Contribution to the contamination problem in Transmission Electron Microscopy.* Ultramicroscopy, 1978. **3**: p. 169-174.
61. Fourie, J.T., *High Contamination Rates from Strongly Adsorbed Hydrocarbon Molecules and a Suggested Solution.* Optik, 1978. **52**(1): p. 91-95.
62. Fourie, J.T., *Elimination of Surface-Originating Contamination in Electron-Microscopes.* Optik, 1979. **52**(5): p. 421-426.
63. Hren, J.J., *Specimen Contamination in Analytical Electron-Microscopy - Sources and Solutions.* Ultramicroscopy, 1978. **3**(4): p. 375-380.
64. Hirsch, P., et al., *Contamination in a Scanning Electron-Microscope and the Influence of Specimen Cooling*. Scanning, 1994. **16**(2): p. 101-110.
65. Amman, M., et al., *Atomic force microscopy study of electron beam written contamination structures.* Journal of Vacuum Science & Technology B (Microelectronics and Nanometer Structures), 1995. **14**(1): p. 54-62.
66. Kanaya, K., et al., *A Cone Formation Theory of Contamination in High-Resolution Transmission Electron-Microscopy.* Micron and Microscopica Acta, 1990. **21**(1-2): p. 13-28.
67. Toth, M., et al., *Electron flux controlled switching between electron beam induced etching and deposition.* Journal of Applied Physics, 2007. **101**(5).
68. Kislov, N.A. and Khodos, II, *Direct Electron-Beam-Induced Formation of Nanometer-Scale Carbon Structures in Stem .2. the Growth of Rods Outside the Substrate.* Microscopy Microanalysis Microstructures, 1992. **3**(4): p. 323-331.
69. Kislov, N.A., *Direct Stem Fabrication and Characterization of Self-Supporting Carbon Structures for Nanoelectronics.* Scanning, 1993. **15**(4): p. 212-218.
70. Mitsuishi, K., et al., *Dynamic profile calculation of deposition resolution by high-energy electrons in electron-beam-induced deposition.* Ultramicroscopy, 2005. **103**(1): p. 17-22.
71. Randolph, S.J., J.D. Fowlkes, and P.D. Rack, *Focused, nanoscale electron-bearn-induced deposition and etching.* Critical Reviews in Solid State and Materials Sciences, 2006. **31**(3): p. 55-89.
72. Fowlkes, J.D., S.J. Randolph, and P.D. Rack, *Growth and simulation of high-aspect ratio nanopillars by primary and secondary electron-induced deposition.* Journal of Vacuum Science & Technology B (Microelectronics and Nanometer Structures), 2005. **23**(6): p. 2825-2832.
73. Alman, D.A., D.N. Ruzic, and J.N. Brooks, *A hydrocarbon reaction model for low temperature hydrogen plasmas and an application to the Joint European Torus.* Physics of Plasmas, 2000. **7**(5): p. 1421-32.
74. Kwitnewski, S., E. Ptasinska-Denga, and C. Szmytkowski, *Relationship between electron-scattering grand total and ionization total cross sections.* Radiation Physics and Chemistry, 2003. **68**(1-2): p. 169-174.

75. Bethe, H., *The theory of the passage of rapid neutron radiation through matter.* Annalen Der Physik, 1930. **5**(3): p. 325-400.
76. Joy, D.C., *Monte Carlo Modeling for Electron Microscopy and Microanalysis*. 1995, New York, London: Oxford University Press.
77. Li, H.M. and Z.J. Ding, *Monte Carlo simulation of secondary electron and backscattered electron images in scanning electron microscopy for specimen with complex geometric structure.* Scanning, 2005. **27**(5): p. 254-267.
78. Yue, Y.T., H.M. Li, and Z.J. Ding, *Monte Carlo simulation of secondary electron and backscattered electron images for a nanoparticle-matrix system.* Journal of Physics D-Applied Physics, 2005. **38**(12): p. 1966-1977.
79. Press, H.W., et al., *Numerical Recipies in C*. 1992, New York: Cambridge University Press.
80. Joy, D.C., *A database for electron-solid interactions.* Scanning, 1995. **17**: p. 270.
81. Lin, Y. and D.C. Joy, *A new examination of secondary electron yield data.* Surface and Interface Analysis, 2005. **37**(11): p. 895-900.
82. Myers, G.E., *Analytical Methods in Conduction Heat Transfer*. 1987, Madison: Genium Publishing.
83. Taylor, P.A., et al., *Adsorption and Decomposition of Acetylene of Si(100)-(2x1).* Journal of American Chemical Society, 1992. **114**: p. 6754-6760.
84. Yoshikawa, Y., S. Akita, and Y. Nakayama, *Barrier modification at contacts between carbon nanotube and Pt electrode using well-controlled Joule heating*. Japanese Journal of Applied Physics Part 2-Letters & Express Letters, 2007. **46**(12-16): p. L359-L361.
85. Slade, P.G., *Electrical contacts : principles and applications*. Electrical engineering and electronics ;, ed. P.G. Slade. 1999, New York :: Marcel Dekker.
86. . The devices were fabricated by Jaime Zahorian from Electrical Engineering department at the Georgia Tech.
87. Dong, L.F., et al., *Floating-potential dielectrophoresis-controlled fabrication of single-carbon-nanotube transistors and their electrical properties.* Journal of Physical Chemistry B, 2005. **109**(27): p. 13148-13153.
88. www.cheaptubesinc.com.
89. www.catalyticmaterials.com.
90. www.nanoamor.com.
91. www.sesres.com.
92. www.nano-lab.com.
93. www.helixmaterial.com.
94. Qian, W.Z., et al., *Quantitative Raman characterization of the mixed samples of the single and multi-wall carbon nanotubes.* Carbon, 2003. **41**(9): p. 1851-1854.
95. Costa, S., et al., *Characterization of carbon nanotubes by Raman spectroscopy.* Materials Science-Poland, 2008. **26**(2): p. 433-441.
96. Ko, H.H., et al., *High-resolution Raman microscopy of curled carbon nanotubes.* Applied Physics Letters, 2004. **85**(13): p. 2598-2600.
97. Richard, C., et al., *Supramolecular self-assembly of lipid derivatives on carbon nanotubes.* Science, 2003. **300**(5620): p. 775-778.
98. Subramanian, A., et al., *Local control of electric current driven shell etching of multiwalled carbon nanotubes.* Applied Physics a-Materials Science & Processing, 2007. **89**(1): p. 133-139.
99. Ajayan, P.M., et al., *Opening Carbon Nanotubes with Oxygen and Implications for Filling.* Nature, 1993. **362**(6420): p. 522-525.
100. Ajayan, P.M. and S. Iijima, *Capillarity-Induced Filling of Carbon Nanotubes.* Nature, 1993. **361**(6410): p. 333-334.
101. Tsang, S.C., et al., *A Simple Chemical Method of Opening and Filling Carbon Nanotubes.* Nature, 1994. **372**(6502): p. 159-162.
102. Ito, T., L. Sun, and R.M. Crooks, *Electrochemical etching of individual multiwall carbon nanotubes.* Electrochemical and Solid State Letters, 2003. **6**(1): p. C4-C7.
103. Banhart, F., *Irradiation effects in carbon nanostructures.* Reports on Progress in Physics, 1999. **62**(8): p. 1181-1221.

104. Yuzvinsky, T.D., et al., *Precision cutting of nanotubes with a low-energy electron beam.* Applied Physics Letters, 2005. **86**(5): p. 3.
105. Lan, C., D.N. Zakharov, and R.G. Reifenberger, *Determining the optimal contact length for a metal/multiwalled carbon nanotube interconnect.* Applied Physics Letters, 2008. **92**(21): p. 3.
106. Choi, Y.R., et al., *Effect of electron beam-induced deposition and etching under bias.* Scanning, 2007. **29**(4): p. 171-176.
107. Wei, X.L., et al., *Controlling electron-beam-induced carbon deposition on carbon nanotubes by Joule heating.* Nanotechnology, 2008. **19**(35): p. 5.
108. Bret, T., et al., *In situ control of the focused-electron-beam-induced deposition process.* Applied Physics Letters, 2003. **83**(19): p. 4005-4007.
109. Taylor, D.M., *ELECTRON-BEAM-INDUCED CONDUCTIVITY AND RELATED PROCESSES IN INSULATING FILMS.* Iee Proceedings-a-Science Measurement and Technology, 1981. **128**(3): p. 174-182.
110. Porrati, F., R. Sachser, and M. Huth, *The transient electrical conductivity of W-based electron-beam-induced deposits during growth, irradiation and exposure to air.* Nanotechnology, 2009. **20**(19): p. 10.
111. Kennedy, D.P., *SPREADING RESISTANCE IN CYLINDRICAL SEMICONDUCTOR DEVICES.* Journal of Applied Physics, 1960. **31**(8): p. 1490-1497.
112. Braunovic, M., *Electrical contacts fundamentals, applications and technology*. Electrical and computer engineering, ed. N.K. Myshkin and V.V. Konchitï¸ sï¸¡. 2006, Boca Raton :: CRC Press.
113. Jiang, J., et al., *Universal expression for localization length in metallic carbon nanotubes.* Physical Review B, 2001. **6404**(4): p. 4.
114. Reznik, A., V. Richter, and R. Kalish, *Kinetics of the conversion of broken diamond (sp(3)) bonds to graphitic (sp(2)) bonds.* Physical Review B, 1997. **56**(13): p. 7930-7934.
115. Miura, N., et al., *Electron-beam-induced deposition of carbonaceous microstructures using scanning electron microscopy.* Applied Surface Science, 1997. **114**: p. 269-273.
116. Rao, A.M., et al., *Diameter-selective Raman scattering from vibrational modes in carbon nanotubes.* Science, 1997. **275**(5297): p. 187-191.
117. Yang, L. and J. Han, *Electronic structure of deformed carbon nanotubes.* Physical Review Letters, 2000. **85**(1): p. 154-157.
118. Ajayan, P.M., et al., *Single-walled carbon nanotube-polymer composites: Strength and weakness.* Advanced Materials, 2000. **12**(10): p. 750-+.
119. Jiang, C.Y., H.Y. Ko, and V.V. Tsukruk, *Strain-sensitive Raman modes of carbon nanotubes in deflecting freely suspended nanomembranes.* Advanced Materials, 2005. **17**(17): p. 2127-+.
120. Tuinstra, F. and J.L. Koenig, *Raman Spectrum of Graphite.* Journal of Chemical Physics, 1970. **53**(3): p. 1126-&.
121. Ferrari, A.C. and J. Robertson, *Interpretation of Raman spectra of disordered and amorphous carbon.* Physical Review B, 2000. **61**(20): p. 14095-14107.
122. Tamor, M.A. and W.C. Vassell, *RAMAN FINGERPRINTING OF AMORPHOUS-CARBON FILMS.* Journal of Applied Physics, 1994. **76**(6): p. 3823-3830.
123. Chu, P.K. and L.H. Li, *Characterization of amorphous and nanocrystalline carbon films.* Materials Chemistry and Physics, 2006. **96**(2-3): p. 253-277.
124. *http://www.cheaptubesinc.com/.*
125. Srivastava, N. and K. Banerjee, *Interconnect challenges for nanoscale electronic circuits.* Jom, 2004. **56**(10): p. 30-31.
126. Nojeh, A., et al., *Ab initio modeling of the interaction of electron beams and single-walled carbon nanotubes.* Physical Review Letters, 2006. **96**(5): p. 4.
127. Wong, W.K., A. Nojeh, and R.F.W. Pease, *Parameters and mechanisms governing image contrast in scanning electron microscopy of single-walled carbon nanotubes.* Scanning, 2006. **28**(4): p. 219-227.
128. Suzuki, M., T. Yamada, and C.Y. Yang, *Monte Carlo simulation of scanning electron microscopy bright contrast images of suspended carbon nanofibers.* Applied Physics Letters, 2007. **90**(8): p. 3.

129. Suzuki, M., et al., *Bright contrast imaging of carbon nanofiber-substrate interface.* Journal of Applied Physics, 2006. **100**(10): p. 5.
130. Suzuki, M., et al., *Secondary electron emission from freely supported nanowires.* Journal of Applied Physics, 2008. **104**(11): p. 6.
131. Seah, M.P. and W.A. Dench, *QUANTITATIVE ELECTRON SPECTROSCOPY OF SURFACES: A STANDARD DATA BASE FOR ELECTRON INELASTIC MEAN FREE PATHS IN SOLIDS.* Surface and Interface Analysis, 1979. **1**(1): p. 2-11.
132. Rykaczewski, K., M.R. Henry, and A.G. Fedorov, *Electron beam induced deposition of residual hydrocarbons in the presence of a multiwall carbon nanotube.* Applied Physics Letters, 2009. **95**(11): p. 113112.
133. Dietz, C.R., *Single-phase forced convection in a microchannel with carbon nanotubes for electronic cooling applications*. 2007.
134. Smith, D.A., J.D. Fowlkes, and P.D. Rack, *Simulating the effects of surface diffusion on electron beam induced deposition via a three-dimensional Monte Carlo simulation.* Nanotechnology, 2008. **19**(41): p. 11.
135. Holt, J.K., et al., *Fast mass transport through sub-2-nanometer carbon nanotubes.* Science, 2006. **312**(5776): p. 1034-1037.
136. Phillips, C., et al., *Model-based optimal design of polymer-coated chemical sensors.* Analytical Chemistry, 2003. **75**(5): p. 1106-1115.
137. Box, G.E.P. and M.E. Muller, *A note on the generation of random normal deviates.* Annals Math. Stat, 1958. **29**: p. 610-611.
138. Wan, Y.-M., et al., *Nanopillar transistors exhibiting single-electron quantum effects at room temperature.* Applied Physics Letters, 2005. **87**(12): p. 123506.
139. Browning, R., et al., *Empirical forms for the electron/atom elastic scattering cross sections from 0.1 to 30 keV.* Journal of Applied Physics, 1994. **76**(4): p. 2016-22.
140. Browning, R., et al., *Low-energy electron/atom elastic scattering cross sections from 0.1-30 keV.* Scanning: Journal of Scanning Microscopy, 1995. **17**(4): p. 250.
141. Dapor, M., *Electron-beam interactions with solids : application of the Monte Carlo method to electron scattering problems*. 2003, Berlin ; New York: Springer.
142. Seah, M.P. and W.A. Dench, *QUANTITATIVE ELECTRON SPECTROSCOPY OF SURFACES: A STANDARD DATA BASE FOR ELECTRON INELASTIC MEAN FREE PATHS IN SOLIDS.* 1979. **1**(1): p. 2-11.
143. Suichu, L., Z. Yongsheng, and W. Ziqin, *A Monte Carlo calculation of secondary electron emitted from Au, Ag, and Cu.* Jounral of Microscopy, 1987. **148**: p. 289-295.
144. Maniwa, Y., et al., *Multiwalled carbon nanotubes grown in hydrogen atmosphere: An x-ray diffraction study.* Physical Review B, 2001. **64**(7).
145. Silva, S.R.P., *Properties of Amorphous Carbon (EMIS Datareviews)* 2003: INSPEC.